Max-Planck-Institut
für Meteorologie

MAX-PLANCK-GESELLSCHAFT

International Max Planck Research School
on Earth System Modelling

Eastern-boundary baroclinic variability and the meridional overturning circulation at 26.5°N

María Paz Chidichimo

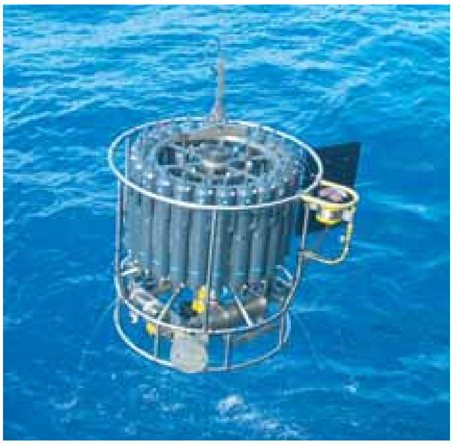

Berichte zur Erdsystemforschung 84
2010

Reports on Earth System Science

Hinweis

Die Berichte zur Erdsystemforschung werden vom Max-Planck-Institut für Meteorologie in Hamburg in unregelmäßiger Abfolge herausgegeben.

Sie enthalten wissenschaftliche und technische Beiträge, inklusive Dissertationen.

Die Beiträge geben nicht notwendigerweise die Auffassung des Instituts wieder.

Die "Berichte zur Erdsystemforschung" führen die vorherigen Reihen "Reports" und "Examensarbeiten" weiter.

Notice

The Reports on Earth System Science are published by the Max Planck Institute for Meteorology in Hamburg. They appear in irregular intervals.

They contain scientific and technical contributions, including Ph. D. theses.

The Reports do not necessarily reflect the opinion of the Institute.

The "Reports on Earth System Science" continue the former "Reports" and "Examensarbeiten" of the Max Planck Institute.

Anschrift / Address

Max-Planck-Institut für Meteorologie
Bundesstrasse 53
20146 Hamburg
Deutschland

Tel.: +49-(0)40-4 11 73-0
Fax: +49-(0)40-4 11 73-298
Web: www.mpimet.mpg.de

Layout:

Bettina Diallo, PR & Grafik

Titelfotos:
vorne:
Christian Klepp - Jochem Marotzke - Christian Klepp
hinten:
Clotilde Dubois - Christian Klepp - Katsumasa Tanaka

Berichte zur Erdsystemforschung
84
2010

Eastern-boundary baroclinic variability and the meridional overturning circulation at 26.5°N

María Paz Chidichimo

aus Buenos Aires, Argentinien

Hamburg 2010

Reports on Earth System Science
84
2010

ISSN 1614-1199

María Paz Chidichimo
Max-Planck-Institut für Meteorologie
Bundesstrasse 53
20146 Hamburg
Germany

Als Dissertation angenommen
vom Department Geowissenschaften der Universität Hamburg

auf Grund der Gutachten von
Prof. Dr. Jochem Marotzke
und
Prof. Dr. Torsten Kanzow

Hamburg, den 29. Juni 2010
Prof. Dr. Jürgen Oßenbrügge
Leiter des Departments für Geowissenschaften

ISSN 1614-1199

Eastern-boundary baroclinic variability and the meridional overturning circulation at 26.5°N

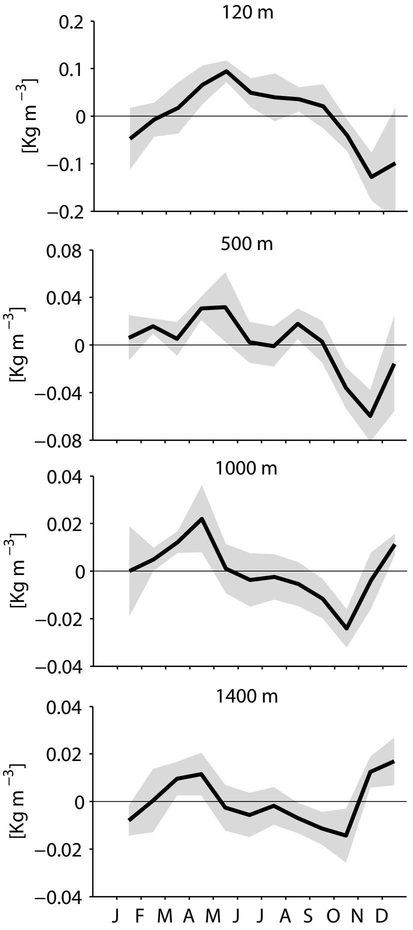

María Paz Chidichimo

Hamburg 2010

Abstract

We study the contribution of eastern-boundary density variations to sub-seasonal and seasonal anomalies of the strength and vertical structure of the Atlantic Meridional Overturning Circulation (AMOC) at 26.5° N, by means of the RAPID/MOCHA mooring array between April 2004 and April 2008. The major density anomalies are found in the upper 500 m, and they are often coherent down to 1400 m. The densities have 13-day fluctuations that are apparent down to 3500 m. The two strategies for measuring eastern-boundary density – a tall offshore mooring (EB1) and an array of moorings on the continental slope (EBH) – show little correspondence in terms of amplitude, vertical structure, and frequency distribution of the resulting basin-wide integrated transport fluctuations, implying that there are significant transport contributions between EB1 and EBH. Contrary to the original planning, measurements from EB1 cannot serve as backup or replacement for EBH: density needs to be measured directly at the continental slope to compute the full-basin density gradient. Fluctuations in density at EBH generate transport variability of 2 Sv rms in the AMOC, while the overall AMOC variability is 4.9 Sv rms. There is a pronounced deep-reaching seasonal cycle in density at the eastern boundary, which is apparent between 100 m and 1400 m, with maximum positive anomalies in spring and maximum negative anomalies in autumn. These changes drive anomalous southward upper mid-ocean flow in spring, implying maximum reduction of the AMOC, and vice-versa in autumn. The amplitude of the seasonal cycle of the AMOC arising from the eastern-boundary densities is 5.2 Sv peak-to-peak, dominating the 6.7 Sv peak-to-peak seasonal cycle of the total AMOC. Our analysis suggests that the seasonal cycle in density may be forced by the strong near-coastal seasonal cycle in wind stress curl. The transport anomalies which dominate the seasonal cycle of the basinwide upper ocean transports do not correspond to basin scale coherent flows but are concentrated at the eastern boundary between EB1 and EBH. As the deep seasonal anomalies at EBH (and the lack thereof at EB1) suggest, the seasonal flow takes place near the African coast rather than being broadly distributed over the more than 1000 km wide section between EB1 and EBH. The seasonal surface elevations inferred from altimetry can not be related to seasonal upper mid ocean transport variability at 26.5° N. The results presented here indicate that it is essential to observe the deep vertical density structure at the eastern boundary of the mid-ocean section as part of an AMOC monitoring strategy at 26.5° N.

Contents

1 Introduction **9**

1.1 Motivation . . . 9

1.2 Research questions . . . 12

1.3 Outline of the thesis . . . 12

2 Contribution of eastern-boundary density variations to the AMOC **15**

2.1 Introduction . . . 15

2.2 Data . . . 17

2.2.1 The eastern-boundary sub-array . . . 18

2.2.2 Data acquisition and processing . . . 23

2.3 Transport calculations . . . 24

2.4 Eastern-boundary hydrographic characteristics . . . 27

2.5 Transport variability . . . 35

2.6 Seasonal variability . . . 40

2.7 Discussion . . . 40

2.8 Conclusions . . . 46

3 Seasonal meridional transport fluctuations at 26.5° N **47**

3.1 Introduction . . . 47

3.2 Data and methods . . . 50

3.2.1 Data . . . 50

3.2.2 Methods . . . 51

3.3 Dynamic height from moored density measurements and SSH . . . 53

3.4 Seasonal upper ocean transports . . . 64

3.5 Discussion . . . 74

3.6 Conclusions . . . 76

4 Conclusions and outlook **79**

4.1 Conclusions . . . 79

4.2 Outlook . . . 82

4.3 Résumé . . . 82

Bibliography **85**

Acknowledgements **91**

Chapter 1

Introduction

1.1 Motivation

The Atlantic Meridional Overturning Circulation (AMOC) carries northward approximately 19 Sv (1 Sv $\equiv 10^6$ m^3 s^{-1}) of warm, saline waters above roughly 1000 m depth and the same amount of cold water southward below 1000 m depth. On its way towards high latitudes the water releases heat to the atmosphere and becomes gradually denser. In the subpolar sea it mixes with deep water during intense wintertime convection. The newly formed cold North Atlantic Deep Water is then exported southward along the east coast of the Americas in a Deep Western Boundary Current below roughly 1000 m depth (Ganachaud and Wunsch 2003). It is well-recognized that at low to mid-latitudes in the Atlantic, the meridional heat transport is largely achieved by the AMOC (rather than by the horizontal gyre circulation), reaching a maximum of 1.3 PW (25 % of the global heat flux) near 24.5° N (Hall and Bryden 1982). Thus, detecting changes in the AMOC is of high importance to detect changes in the North Atlantic's heat budget, which greatly influences the Northeast Atlantic climate (e.g., Rahmstorf 2003).

In the past, the strength and the vertical structure of the AMOC was estimated from temporally sparse hydrographic observations (e.g., Worthington 1976; Hall and Bryden 1982; Roemmich and Wunsch 1985; Bryden et al. 2005; Longworth 2007). The insufficient temporal resolution, however, would complicate the analysis of variability or the detection of trends in the AMOC.

To monitor continuously the temporal evolution of the AMOC at 26.5° N, the RAPID (Rapid Climate Change)/MOCHA (Meridional Overturning Circulation and Heat Transport Array) array become operational in 2004 (Hirschi et al. 2003; Kanzow et al. 2008a). The strength of the AMOC at 26.5° N can be divided into three components: the Gulf Stream transport across the 800 m deep straits of Florida between the Florida and the Bahamas, the zonally integrated Ekman transport, and the mid-ocean northward geostrophic transport (Cunningham et al. 2007). The latter has two components, the transport through the western boundary wedge over the Bahamas continental slope, and the transatlantic upper mid-ocean transport between the base of Bahamas continental slope at about 77° W and the African coast at about 14° W. The Gulf stream flow is measured by a submarine cable across the Florida Straits, and the wind-driven near-surface Ekman transport is derived from QuikSCAT sattelite observations. The transports of the Antilles current and deep western boundary current offshore of Abaco, Bahamas are monitored by direct velocity measurements. The heart of RAPID/MOCHA is an array of moorings to monitor the transatlantic zonally integrated geostrophic northward flow estimated from full-depth density measurements at the eastern and western boundaries of the Atlantic.

From the first year of observations, Kanzow et al. (2007) showed that the RAPID/ MOCHA array observations satisfy mass conservation for periods longer than 10 days, demonstrating the ability of the observing system to measure the strength and vertical structure of the AMOC continuously. Cunningham et al. (2007) determined the time mean of the AMOC at 26.5° N between March 2004 and March 2005 as 18.7 Sv, with a large intraseasonal variability of ±5.6 Sv rms. They found that variations of the Gulf Stream transport (of 3.3 Sv), the Ekman transport (of 4.4 Sv), and the upper mid-ocean geostrophic transport (of 3.1 Sv) contributed about equally to the AMOC temporal variability. The size of the contribution of eastern-boundary density variations to the AMOC, however, has not been studied systematically. It is normally the role of the western boundary flows that is mostly discussed in the context of the AMOC since they are assumed to be primarily responsible for AMOC variability, and thus density variability at the western boundary of the North Atlantic is expected to be larger than at the eastern boundary (Johnson and Marshall (2004); Longworth (2007)). Using historical density profiles from hydrographic cruises, Longworth (2007) found that the western-boundary contribution of the mid-ocean section to the basinwide transport fluctuations in the 0 – 800 m depth layer was twice as large as the eastern-boundary contribution (±2.8 Sv vs. ±1.5 Sv rms). However, this estimate is very uncertain since it is based on only five transatlantic CTD sections. Therefore, the primary objective of this thesis is to use the comprehensive data set now available through RAPID/MOCHA, to investigate whether eastern-boundary density variability is an important contributor to sub-seasonal and seasonal anomalies of the strength and vertical structure of the AMOC at 26.5° N.

The core of the RAPID array is an array of moored instruments deployed along 26.5° N to monitor the mid-ocean flow. From April 2004 to present, two alternative ways of sampling density profiles have been maintained continuously at the eastern boundary: a tall offshore mooring (EB1) and an array of moorings distributed on the continental slope (EBH) (more details are provided in Chapter 2). EBH array has suffered significant mooring losses, in large part due to fishing activity on the continental slope. Thus, we analyze the transport contributions from densities measured with EB1 and EBH to explore whether EB1 might serve as a backup or replacement of EBH, as was formulated in the original observing system design (Marotzke et al. 2002).

The eastern boundary current system along the Northwest African coast consists of the near-surface southward-flowing Canary Current, which carries between 1 Sv and 4 Sv (Hernández-Guerra et al. 2003, 2005), and a poleward flowing undercurrent along the African continental slope at about 950 m depth (Knoll et al. 2002). Dynamics of the eastern boundary current system include wind-driven changes in the strength of the Canary Current, Kelvin waves propagating poleward (Kawase 1987; Johnson and Marshall 2002), coastal upwelling induced by seasonal changes of the southerly trade winds (e.g., Mittelstaedt 1983), and the generation of mesoscale eddies south of the Canary Islands due to the presence of the islands in the path of the Canary Current (Hernández-Guerra et al. 1993). Here, we will investigate if we can distinguish these mechanisms in the observed eastern-boundary density variability from the moorings.

We find pronounced deep-reaching seasonal displacements of the isopycnals at the eastern boundary that appear to drive the largest part of the seasonal upper mid-ocean transports. For a better understanding of the seasonal transports, it is essential to observe whether they correspond to broad (basin scale) or localized (near ocean boundary) flows. The study of the zonal distribution of transport variability can be approximated by the computation of the temporal evolution of the flow strength between the RAPID/MOCHA full-depth dynamic height moorings distributed along 26° N, but this analysis will be limited by the zonal distance between the different moorings in the basin interior of O(1000 – 2000 km). In order to study both the zonal and meridional patterns of AMOC-related seasonal transport variability and the relation to eastern boundary densities, there is the need of putting the local information retrieved by the RAPID/MOCHA in a wider context by comparison with other data sets. The gradient in sea surface height (SSH or η) is a measure of the surface geostrophic flow, therefore altimetry might be an efficient tool to estimate the time variable strength of upper ocean transports. If good agreement between transport from mooring data and altimetry was found, altimetry could be used to study the zonal distribution of the seasonal transport at a much better zonal resolution than that provided by the moorings. Kanzow et al. (2009) found that the basinwide zonal differences in η between the eastern and the western boundary basin margins cannot be used to infer basinwide fluctuations of the meridional upper mid-ocean flow at 26.5° N at subseasonal timescales. They argue that this is due to the complexity of the vertical structure of the flow near the western boundary that does not allow a clean projection of η on a first baroclinic modal structure in contrast to the situation offshore. However, they found significant positive correlations between upper-ocean transport integrated between the eastern boundary and different sites 40 and 500 km away from the western boundary and the zonal difference in η between the corresponding section endpoints. These results are in line with those of Hirschi et al. (2009) based on numerical model simulations. In a modelling study Bingham and Hughes (2009) found that the sea surface height at the ocean margin might be a good indicator of the AMOC variability at interannual and longer timescales. Here we test whether the *seasonal* surface elevations from altimetric records can be related to *seasonal* upper mid-ocean transports at 26.5° N. If successful it would analyze the zonal structure associated with the observed, pronounced seasonal variability of the AMOC at a much higher spatial resolution than that set by the zonal separation of the RAPID/MOCHA moorings. Also, as high-quality altimetric heights are available from 1992 to present, the seasonal transport cycle transports could be computed over a long period of time.

1.2 Research questions

Based on the motivation presented above, the main research questions investigated in this study can be summarized as follows:

(1) Is the eastern-boundary density variability an important contributor to sub-seasonal and seasonal anomalies of the strength and vertical structure of the AMOC at 26.5° N?

(2) Are the density anomalies coherent at EB1 and EBH such that EB1 might serve as backup or replacement of EBH, as was formulated in the original proposal (Marotzke et al. 2002)?

(3) Which are the possible driving mechanisms of eastern-boundary density variability on seasonal timescales?

(4) Do the seasonal upper mid-ocean transport anomalies correspond to broad (basin scale) or localized (e.g. near ocean boundary) flows?

(5) Is altimetry a useful tool to infer seasonal upper mid-ocean transports at 26.5° N?

1.3 Outline of the thesis

This thesis is organized in two main chapters where our work is developed, and a final chapter with the general conclusions of this thesis and an outlook. Chapters 2 and 3 are structured with introduction, data and methods, results, discussion and conclusions. Chapter 4 presents the conclusions and an outlook.

In Chapter 2, we present the analysis of the contribution of eastern-boundary density variations to sub-seasonal and seasonal anomalies of the AMOC at 26.5° N by means of RAPID/MOCHA mooring data. For this, we estimate the transport contributions arising from eastern-boundary density variability from a tall mooring (EB1) located at the base of the eastern continental slope and an array of small moorings distributed across the continental slope up to the Moroccan shelf (EBH) to address questions (1) and (2). We further investigate the possible driving mechanisms of eastern-boundary density variability to attempt to answer question (3). In Chapter 3, we investigate the relationship between mooring-derived dynamic heights and η with a focus on seasonal variability at the eastern boundary. Next we analyze the seasonal upper mid-ocean transports in the various segments along 26.5° N defined by the mooring locations, and compare them with the corresponding zonal differences in η, addressing questions (4) and (5).

Chapter 2 has been published in *Ocean Science*[1]. Part of these results are also included in Kanzow et al. (2010), currently in review in *Journal of Climate*[2]. Similarly, Chapter 3 is intended as a paper draft and can be read on its own.

---

[1] Chidichimo, M. P., Kanzow, T., Cunningham, S. A., Johns, W. E., and Marotzke, J.: The contribution of eastern-boundary density variations to the Atlantic meridional overturning circulation at 26.5° N, Ocean Science, 6, 475-490, 2010.

[2] Kanzow, T., Cunningham, S. A., Johns, W. E., Hirschi, J. J.-M., Marotzke, J., Baringer, M. O., Meinen, C. S., Chidichimo, M. P., Atkinson, C., Beal, L. M.,Bryden, H. L., and Collins, J.: Seasonal variability of the Atlantic meridional overturning circulation at 26.5° N, Journal of Climate, in review, 2010.

Chapter 2

The contribution of eastern-boundary density variations to the Atlantic meridional circulation at 26.5° N

2.1 Introduction

The Atlantic Meridional Overturning Circulation (AMOC) moves northward approximately 19 Sv ($1\,\mathrm{Sv} \equiv 10^6\ \mathrm{m}^3\ \mathrm{s}^{-1}$) of warm, saline waters above roughly 1000 m depth and the same amount of cold water back south below 1000 m. The AMOC plays a key role in the meridional heat transport in the North Atlantic and the resulting heat release to the atmosphere on the water's way towards high latitudes. In the past, the strength of the AMOC was estimated from temporally sparse hydrographic observations (e.g., Worthington 1976; Hall and Bryden 1982; Roemmich and Wunsch 1985; Bryden et al. 2005; Longworth 2007). The insufficient temporal resolution, however, would complicate the analysis of variability or the detection of trends in the AMOC. To monitor continuously the temporal evolution of the AMOC at 26.5° N, the RAPID (Rapid Climate Change)/MOCHA (Meridional Overturning Circulation and Heat Transport Array) array become operational in 2004 (Hirschi et al. 2003; Kanzow et al. 2008a). The strength of the AMOC at 26.5° N is calculated by adding the northward transport from three contributions: the Gulf Stream transport through the Straits of Florida, measured by a submarine cable; the near surface Ekman transport, measured by satellite scatterometry; and the mid-ocean geostrophic transport across the 6000 km wide zonal section between the Bahamas and Africa, measured by the RAPID/MOCHA mooring array proper. Using the RAPID/MOCHA data, we here analyze the eastern-boundary contributions to sub-seasonal and seasonal AMOC variability.

Results from the first year of the RAPID/MOCHA array have demonstrated the ability of the observing system to measure the strength and vertical structure of the AMOC continuously (Kanzow et al. 2007). Cunningham et al. (2007) determined the time mean of the AMOC at 26.5° N between 29 March 2004 and 31 March 2005 as 18.7 Sv, with a temporal standard deviation of ±5.6 Sv. Variations of the Gulf Stream transport (of ±3.3 Sv), the Ekman transport (of ±4.4 Sv) and the upper mid-ocean geostrophic transport (of ±3.1 Sv) contributed about equally to the AMOC temporal variability. The impact of eastern-boundary density changes on the AMOC, however, has not been studied systematically. Usually, the western boundary currents are assumed to be primarily responsible for AMOC variability, and thus density variability at the western boundary of the North Atlantic is expected to be larger than at the eastern boundary (Johnson and Marshall 2004; Longworth 2007). Using historical density profiles from hydrographic cruises, Longworth (2007) investigated to what extent transport fluctuations in the $0 - 800$ m layer of the mid-ocean section at 26° N arose from western-boundary or eastern-boundary density variability. She found that the western-boundary contribution was twice as large as the eastern-boundary contribution (±2.8 Sv vs. ±1.5 Sv rms). However, this estimate is very uncertain since it is based on only five transatlantic CTD sections. On the other hand Kanzow et al. (2009) found evidence that boundary wave dynamics provide an efficient mechanism to suppress eddy and Rossby wave induced density fluctuations right at the western boundary. Using the comprehensive data set now available through RAPID/MOCHA, we investigate as our first objective whether the amplitude and frequency distribution of eastern-boundary density variability is an important contribution to sub-seasonal and seasonal anomalies of the strength and vertical structure of the AMOC at 26.5° N between April 2004 and October 2007.

The core of RAPID/MOCHA is a hydrographic mooring array along 26.5° N to monitor the mid-ocean flow. Between April 2004 and October 2007 two density monitoring systems have been maintained continuously at the eastern boundary: (i) a tall 5000-m-long offshore mooring (EB1) located at the base of the African continental slope at 23° 48.6′ N, 24° 5.7′ W, and (ii) an array of short (about 500 m long) moorings on the slope covering different vertical levels (EBH). It is desirable to measure density right at the boundary (as with EBH), in order to compute the transatlantic mid-ocean geostrophic transports; however, measurements offshore of the upwelling regime (EB1) would reduce the risk of data loss due to fishing activity (Rayner 2007). Therefore, we explore as our second objective whether indeed the density anomalies are coherent at EB1 and EBH such that EB1 might serve as a backup or replacement of EBH, as was formulated in the original observing system design (Marotzke et al. 2002).

Among the mechanisms that may change densities at the eastern boundary at 26.5° N, and thus the strength of the AMOC, are Kelvin waves propagating poleward (Kawase 1987; Johnson and Marshall 2002), or wind-driven changes in the strength of the Canary Current, or coastal upwelling created by anomalies in the local wind stress along the coasts (Köhl 2005), or the generation of cyclonic and anticylonic eddies at the flank of the Canary Islands (Hernández-Guerra et al. 1993). As our third objective in this paper, we investigate in a preliminary fashion whether our data allow us to distinguish among these mechanisms.

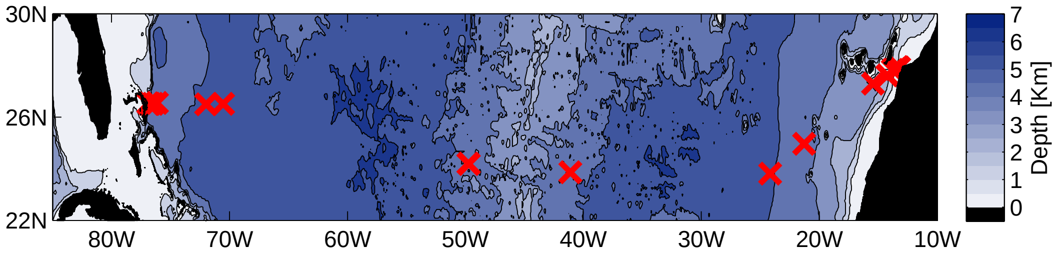

Figure 2.1: Distribution of the RAPID/MOCHA moorings across 26.5° N as deployed for year 2007.

This chapter is structured as follows. In Section 2.2 we introduce the two mooring data sets. Section 2.3 establishes the methodology to infer the eastern-boundary density contribution to AMOC variability. Section 2.4 describes the main hydrographic characteristics. Section 2.5 gives the analysis of the temporal evolution of the observed flows, their vertical structure, and a comparison of the transport contributions as obtained from EB1 and EBH. Section 2.6 details the seasonal variability of the density fluctuations at the eastern boundary of the subtropical North Atlantic off Morocco. Section 2.7 provides a discussion, and Section 2.8 presents our conclusions.

2.2 Data

The RAPID/MOCHA array was first deployed in spring 2004, and has been operating continuously since then. Kanzow et al. (2008a) gave a detailed description of the full array (see also http://www.noc.soton.ac.uk/rapidmoc). The northward flow of warm water through the 800 m deep Straits of Florida is monitored by a submerged telephone cable crossing the Straits between Florida and the Bahamas (Larsen 1992; Baringer and Larsen 2001). The Ekman transport is derived from QuikSCAT satellite scatterometry (Kanzow et al. 2007). The currents over the steep western boundary continental slope are obtained by direct velocity measurements (Johns et al. 2008). The mid-ocean flow is monitored by a hydrographic mooring array along the 26.5° N section between the Bahamas at about 77° W and the African Coast at about 15° W. The transatlantic array consists of the western-boundary (east of the Bahamas), the mid-Atlantic Ridge, and the eastern-boundary (west of Morocco) sub-arrays (Figure 2.1).

The full-depth moorings have between 11 and 24 CTD sensors at fixed depths throughout the water column. Some of the moorings of the western-boundary sub-array (WB0, WB3, WB5) (Johns et al. 2008, their Figure 1) are serviced at 18-months intervals; the remaining moorings of the full array are serviced at annual intervals (during autumn for the eastern boundary). The western-boundary and eastern-boundary moorings constitute the endpoint density profiles required to calculate the basin-wide zonally integrated geostrophic flow.

2.2.1 The eastern-boundary sub-array

The eastern-boundary sub-array as deployed for the year 2007 is shown in Figure 2.2; the nominal positions and water depths of the moorings are given in Table 2.1. The full water-column mooring EB1 is situated at the base of the continental slope, roughly 1250 km from the coast. On the first year (2004) EB1 was deployed at a nominal position of 24°31.4′ N, 23°26.9′ W. From the second year (2005) onwards, EB1 was moved to a nominal position of 23°48.6′ N, 24°5.7′ W with the purpose of locating it on a satellite track. The inshore array (EBH) consists of a series of shorter moorings distributed between the African shelf and the base of the eastern continental slope. Each of these *small* moorings covers a certain depth range such that all of them merged together account for the full boundary density profile between the surface and 5000 m. The periods of the mooring records and the nominal depths of the CTD sensors are given in Tables 2.2 and 2.3 for EB1 and EBH, respectively. Vertical sensor spacing increases with depth from roughly 100 m near the sea surface, to 200 m at the bottom of the thermocline, to 500 m in the deep ocean. During the different deployment periods the array has been subject to some minor design changes. Initially, from March 2004 to April 2005, EB1 occupied the depth range between 2500 dbar and 4850 dbar. Since April 2005 EB1 has covered the entire water column, with 24 sensors (21 sensors between November 2005 and May 2006). The re-deployment of EB1 failed in October 2006, and it was only re-deployed during a cruise in December 2006. For this reason, there is a time gap of ca. 2 months (from 8 October 2006 to 1 December 2006, Table 2.2). Each of the moorings of the EBH array has between 1 and 6 CTD sensors. In order to obtain the eastern-boundary profile for the first deployment period (March 2004 to April 2005), the measurements at EBH5, EBH4, EBH3, EBH2, EBH1 and EB1 are merged into one profile. In this way, EBH5 provides the density profile between 565 dbar and 965 dbar, EBH4 between 1060 dbar to 1460 dbar, EBH3 between 1555 dbar and 1955 dbar, EBH2 at 2060 dbar and EBH1 between 2562 dbar and 2762 dbar. Deep eastern-boundary measurements are taken from EB1 (below roughly 3000 dbar). The same merging procedure applies to the following years. From April 2005, the EBH array had consistently measurements above 500 dbar and two additional moorings (EBH0 and EBHi) were deployed across the slope to account for density measurements in the 3500–4500 dbar pressure range. During the second deployment period, all the sensors stopped recording due to battery failures, producing a gap in the data of ca. 3 months (from 2 February 2006 to 22 May 2006, Table 2.3).

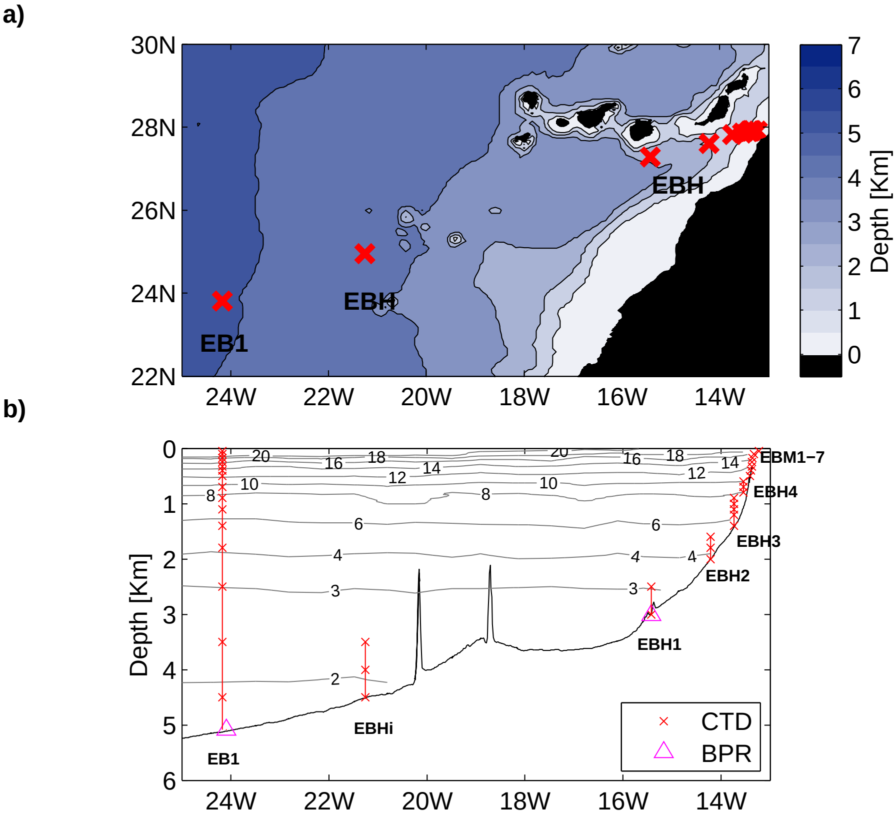
a)
30N
28N
26N
24N
22N
24W
22W
20W
18W
16W
14W
EB1
EBH
EBH
Depth [Km]
0
1
2
3
4
5
6
7
b)
Depth [Km]
0
1
2
3
4
5
6
EBM1−7
EBH4
EBH3
EBH2
EBH1
EBHi
EB1
20
16
18
14
12
10
8
6
4
3
2
CTD
BPR

Figure 2.2: (a) Location of the moorings near the eastern boundary of the 26.5° N section (red crosses), (b) distribution of CTD sensors and bottom pressure recorders (BPR) at the eastern boundary array as deployed for year 2007. The contours represent potential temperature in °C from a CTD transatlantic section at a nominal latitude of 24.5° N carried out in year 2004.

Mooring name	Latitude (North)	Longitude (West)	Water Depth [m]
EB1	23°48.6′ (24° 31.4′)	24°5.7′ (23° 26.9′)	5000
EBH1	27°16.5′	15°25.0′	3012
EBH2	27°29.2′	14°41.0′	2510
EBH3	27°37.3′	14°12.3′	2005
EBH4	27°49.9′	13°47.3′	1510
EBH5	27°51.4′	13°31.2′	1015
EBHi	24°57.3′	21°15.4′	4499
EBH0	26°59.6′	16°13.7′	3511
EBM1	27°53.6′	13°24.4′	500
EBM2	27°54.0′	13°23.4′	400
EBM3	27°54.3′	13°22.3′	325
EBM4	27°54.5′	13°21.9′	250
EBM5	27°54.6′	13°21.5′	175
EBM6	27°55.2′	13°19.9′	100
EBM7	27°54.4′	13°13.5′	50

Table 2.1: Nominal positions and water depths of eastern-boundary moorings. Note that the position of EB1 changed slightly between the first year's deployment (2004) and the subsequent deployments (2005 onwards). The position of EB1 corresponds to year 2005 deployment, while the position corresponding to the year 2004 is given in brackets.

Start Date	End Date	Nominal Instrument Pressures [dbar]	T/S Levels
4-Mar-04	7-Apr-05	2500, 3000, 3500, 4000, 4500, 4850	6
13-Apr-05	18-Nov-05	94, 144, 219, 294, 369, 444, 544, 644, 744, 844, 944, 1044, 1144, 1244, 1444, 1644, 1844, 2044, 2544, 3044, 3544, 4044, 4544, 4894	24
28-Nov-05	3-May-06	250, 325, 400, 500, 600, 700, 800, 900, 1000, 1100, 1200, 1400, 1600, 1800, 2000, 2500, 3000, 3500, 4000, 4500, 4850	21
22-May-06	8-Oct-06	110, 160, 250, 325, 400, 475, 550, 650, 750, 850, 950, 1050, 1150, 1250, 1450, 1550, 1750, 1950, 2150, 2650, 3150, 3650, 4150, 4800	24
1-Dec-06	14-Oct-07	50, 100, 175, 250, 325, 400, 500, 600, 700, 800, 900, 1000, 1100, 1200, 1400, 1600, 1800, 2000, 2500, 3000, 3500, 4000, 4500, 4850	24

Table 2.2: Periods of mooring records and nominal pressure levels of sensors of EB1 mooring.

Start Date	End Date	Nominal Instrument Pressures [dbar]	T/S Levels
4-Mar-04	1-Apr-05	565, 665, 765, 915, 965 (EBH5); 1060, 1160, 1260, 1410, 1460 (EBH4); 1555, 1655, 1755, 1905, 1955 (EBH3); 2060 (EBH2); 2562, 2762 (EBH1)	18
13-Apr-05	2-Feb-06	50, 100, 175, 250 (EBH5)**; 240, 315, 415, 515, 615, 715, 815 (EBH4)*; 911, 1011, 1111, 1211, 1411 (EBH3)**; 1600, 1800, 1990 (EBH2)**; 2510, 2990 (EBH1)**; 3490 (EBH0); 3510, 4010, 4490 (EBHi)**	24
22-May-06	4-Oct-06	50, 100, 175, 250 (EBH5); 325, 400, 500, 600, 700, 800 (EBH4); 900, 1000, 1100, 1200, 1400 (EBH3); 1600, 1800, 2000 (EBH2); 2500, 3000 (EBH1); 3500 (EBH0); 4000 (EBHi)	22
12-Oct-06	14-Oct-07	50 (EBM7)*; 100 (EBM6)*; 174 (EBM5)*; 253 (EBM4); 325 (EBM3)*; 400 (EBM2)*; 515 (EBM1); 600, 700, 800 (EBH4); 900, 1000, 1100, 1200, 1400 (EBH3); 1600, 1800, 2000 (EBH2); 2500, 3000 (EBH1); 3500 (EBH0); 3500, 4000, 4500 (EBHi)	23

* not recovered
** battery failures.

Table 2.3: Periods of mooring records and nominal pressure levels of sensors of EBH array.

The data recovery on the slope was complicated by mooring losses, most likely due to fisheries activities south of the Canary Islands. For instance, for the period from April 2005 to February 2006, one of the shallower moorings (EBH4) could not be recovered leading to a data loss at the 300–800 dbar pressure range (Rayner 2007). In an attempt to reduce the potential impact of fishing activity, in the deployment during October 2006 the shallowest mooring EBH5 was divided into a set of smaller 'mini-moorings', EBM1 to EBM7, consisting of only one CTD sensor per mooring. However, only two of the 'mini-moorings' returned data (EBM4 and EBM1, at 253 dbar and 515 dbar, respectively), two more were recovered with sensors missing (EBM5 and EBM6).

2.2.2 Data acquisition and processing

All the moored sensors discussed here are Seabird SBE37 (MicroCAT), which measure temperature, conductivity and pressure. The sensors acquire data at sampling rates between 15 and 30 min. For calibration, all moored CTD sensors are lowered on a frame together with a reference CTD package (SBE 911) before and after each deployment period. Calibration coefficients for each sensor are computed and linear trends are removed following Kanzow et al. (2006). An overall accuracy of 0.001°C, 0.002 mS/cm and 1 dbar relative to the reference CTD is achieved.

Using all the information described in Section 2.2.1, full-depth continuous profiles of temperature and salinity and thus of density (ρ) are obtained at each site as follows. Salinity is computed and temperature, salinity, and pressure are two-day low-pass filtered and interpolated on a half-daily grid. Temperature and salinity are vertically interpolated onto a regular 20-dbar pressure grid (Kanzow et al. 2007) using an interpolation technique relying on climatological temperature and salinity gradients between vertically adjacent sensor levels (Johns et al. 2005). Each MicroCAT has a pressure sensor so that when interpolating the temperature and salinity profiles between adjacent pressure levels of measurements on a regular pressure grid, the measured pressures at each time step are taken into account to avoid mooring motion effects. Finally ρ is computed. For each deployment period, upward integration of temperature and salinity is done up to the uppermost level of measurements available. The only exceptions are for year 2004 and year 2007 at EBH, when the uppermost level of measurements was 540 dbar and 240 dbar, respectively, and the data were extrapolated to 120 dbar at each time step as follows. For the year 2004 temperature and salinity are linearly extrapolated to 240 dbar by estimating the gradient from the anomalies at 840 and 540 dbars and then carrying the anomaly at 240 dbar at constant value up to 120 dbar (Kanzow et al. (2007), Supporting Online Material). For the year 2007, the data are linearly extrapolated to 120 dbar on the basis of the gradient of the anomaly between the two uppermost levels of measurements.

2.3 Transport calculations

We start by describing briefly how a time series of strength of the AMOC, $\psi_{\mathrm{MAX}}(t)$, is computed from the observational data (for more details see Kanzow et al. (2010)). Then we show how the contribution of eastern-boundary density variations to the AMOC is calculated.

At 26.5° N, $\psi_{\mathrm{MAX}}(t)$ is calculated by the sum of three meridional flow components: the northward Gulf Stream transport through the Straits of Florida (T_{GS}), the zonally integrated near-surface Ekman transport (T_{EK}), and the geostrophic mid-ocean transport between the Bahamas and the African coast (T_{MO}). From these transport contributions, a vertical profile of zonally integrated northward transport per unit depth (T_{AMOC}) is computed such that

$$T_{\mathrm{AMOC}}(z,t) = T_{\mathrm{GS}}(z,t) + T_{\mathrm{EK}}(z,t) + T_{\mathrm{MO}}(z,t), \tag{2.1}$$

where z denotes negative depth.

$\psi_{\mathrm{MAX}}(t)$ at 26.5° N is defined at each time step as the maximum northward transport in the upper ocean. The northward transport is integrated downward from the sea surface to the depth level $h_{\max}(t)$ where the maximum cumulative northward transport is reached at each time step (that is, the depth where the zero crossing between northward and southward flow occurs), according to

$$\Psi_{\mathrm{MAX}}(t) = \int\limits_{z=-h_{\max}}^{z=0} T_{\mathrm{AMOC}}(z,t)dz. \tag{2.2}$$

For the computation of $T_{\mathrm{AMOC}}(z,t)$, $T_{\mathrm{GS}}(z,t)$ and $T_{\mathrm{EK}}(z,t)$ are computed directly from the cable and wind observations, respectively. The cable measurements give an estimate of the vertically integrated transport $T_{\mathrm{GS}}(t)$. The modal vertical structure of the flow through the Straits of Florida is estimated from historical Pegasus measurements across the straits. Subsequently, the vertical structure $T_{\mathrm{GS}}(z,t)$ is obtained by projecting T_{GS} onto the leading vertical mode of the meridional transport per unit depth, which accounts for 87% of the variance (Baringer et al. 2008). $T_{\mathrm{EK}}(t)$ is computed by zonally integrating the Ekman transport between the shelf of Abaco (Bahamas) (X_{A}) and the African coast (X_{E}) following

$$T_{\mathrm{EK}}(t) = -\int\limits_{X_{\mathrm{A}}}^{X_{\mathrm{E}}} \frac{\tau_X(x,t)}{\rho f}dx \tag{2.3}$$

where τ_x is the zonal component of the wind stress, ρ is a reference density and f is the Coriolis parameter. In order to obtain vertical transport per unit depth profiles

$T_{\mathrm{EK}}(z,t)$ that are consistent with previous studies, the transports in T_{EK} are equally distributed in the upper 100 m (Kanzow et al. 2007; Cunningham et al. 2007).

$T_{\mathrm{MO}}(z,t)$ has two components: the transport $T_{\mathrm{WBW}}(z,t)$ through the western boundary wedge over the Bahamas continental slope – calculated from direct current meter measurements (Johns et al. 2008) – and the geostrophic transport between the Bahamas and the African coast. The latter is computed from the internal transport, T_{INT}, calculated from the east to west density gradient and a reference transport T_{C}. T_{INT} is computed by means of the vertical density profiles at the western boundary and the eastern boundary (ρ_{W} and ρ_{E}), relative to a reference level (h_{ref}), according to

$$T_{\mathrm{INT}}(z,t) = -(g/\rho f) \int\limits_{z'=-h_{\mathrm{ref}}}^{z} [\rho_E(z',t) - \rho_{\mathrm{W}}(z',t)]dz', \text{ for } z > -h_{\mathrm{ref}}, \tag{2.4}$$

where g is the Earth's gravitational acceleration, ρ is a reference density, and f is the Coriolis parameter. To compute absolute values of $T_{\mathrm{MO}}(z,t)$, a reference transport for $T_{\mathrm{INT}}(z,t)$ needs to be computed at each time step. This is calculated by the imposition of no net mass transport across the longitude-depth section at 26.5° N, which is justified for timescales longer than 10 days (Kanzow et al. 2007). This constraint is equivalent to a perfect compensation among the different flow components, according to

$$\int\limits_{z=-h_{\mathrm{bot}}}^{z=0} [T_{\mathrm{GS}}(z,t) + T_{\mathrm{EK}}(z,t) + T_{\mathrm{MO}}(z,t)]dz = 0, \tag{2.5}$$

where h_{bot} represents the depth of the sea floor.

The reference transport of $T_{\mathrm{INT}}(z,t)$, namely $T_{\mathrm{C}}(t)$, is computed at each time step according to

$$T_{\mathrm{C}}(t) = -\int\limits_{z=-h_{\mathrm{bot}}}^{z=0} [T_{\mathrm{GS}}(z,t) + T_{\mathrm{EK}}(z,t) + T_{\mathrm{WBW}}(z,t) + T_{\mathrm{INT}}(z,t)]dz. \tag{2.6}$$

The computation of T_{C} is performed assuming that the compensating meridional velocity field $V_{\mathrm{C}}(x,z)$ is spatially uniform (Hirschi et al. 2003) such that

$$T_{\mathrm{C}} = V_{\mathrm{C}} \int\limits_{z=-h_{\mathrm{bot}}}^{z=0} \int\limits_{X_{\mathrm{E}}}^{X_{\mathrm{W}}} dxdz = V_{\mathrm{C}} \int\limits_{z=-h_{\mathrm{bot}}}^{z=0} L(z)dz, \tag{2.7}$$

where X_{W} and X_{E} denote the position of the western and eastern boundary endpoints, and L is the effective width of the transatlantic section, which reduces with depth (Kanzow et al. 2010).

The absolute mid-ocean transport is then given by

$$T_{\mathrm{MO}}(z,t) = T_{\mathrm{WBW}}(z,t) + T_{\mathrm{INT}}(z,t) + T_{\mathrm{C}}(z,t), \tag{2.8}$$

with $T_{\mathrm{C}}(z,t)$=$V_{\mathrm{C}}L(z)$.

How then is the transport contribution of eastern-boundary densities to $\psi_{\mathrm{MAX}}(t)$ isolated? The basic concept is to perform the transport calculations such that the only time-variable contribution comes from eastern-boundary densities. As there is no significant correlation between density fluctuations at the western boundary (off the Bahamas) and the eastern boundary for annual and higher frequencies (Kanzow et al. 2010), we can isolate the eastern-boundary contribution to $T_{\mathrm{MO}}(z,t)$ by prescribing a time-invariant density profile at the western boundary at each time step in Eq. (2.4). We use

$$T^{\mathrm{EB}}_{\mathrm{INT}}(z,t) = -(g/\rho f) \int\limits_{z'=-h_{\mathrm{ref}}}^{z} [\rho_E(z',t) - \overline{\rho}_{\mathrm{W}}(z')]dz', \text{ for } -h_{\mathrm{ref}} < z < -h_{\mathrm{up}}, \tag{2.9}$$

where the overbar denotes the time-average. The reference depth, h_{ref}, is taken as the greatest common depth of the moorings in the east (4900 m), and h_{up} represents the uppermost measurement level at the eastern boundary; h_{up} differs between the different mooring deployment periods (Tables 2.2 and 2.3). To obtain estimates for the entire water column, the profiles of transport per unit depth resulting from Eq. (2.9) are linearly extrapolated from the uppermost measurement level to the surface for each time step, on the basis of the gradient of the transport anomaly between the two uppermost levels of measurements. When required, the profiles are linearly interpolated in time to fill the time gaps of 1–2 weeks between mooring recovery and redeployment.

We then add at each time step the resulting transport per unit depth anomaly profiles arising from Eq. (2.9) to the time-mean contribution of all the other components according to

$$T^{\mathrm{EB}}_{\mathrm{AMOC}}(z,t) = \bar{T}_{\mathrm{GS}}(z) + \bar{T}_{\mathrm{EK}}(z) + \bar{T}_{\mathrm{WBW}}(z) + T^{\mathrm{EB}}_{\mathrm{INT}}(z,t) + T^{\mathrm{EB}}_{\mathrm{C}}, \tag{2.10}$$

such that the compensating transport at each time step $T^{\mathrm{EB}}_{\mathrm{C}}(t)$ is given by

$$T^{\mathrm{EB}}_{\mathrm{C}}(t) = -\int\limits_{z=-h_{\mathrm{bot}}}^{z=0} [\bar{T}_{\mathrm{GS}}(z) + \bar{T}_{\mathrm{EK}}(z) + \bar{T}_{\mathrm{WBW}}(z) + T^{\mathrm{EB}}_{\mathrm{INT}}(z,t)]dz. \tag{2.11}$$

Consistent with Eq. (2.2), the eastern-boundary density contribution to the strength of the AMOC is computed from

$$\Psi^{\mathrm{EB}}_{\mathrm{MAX}}(t) = \int\limits_{z=-h_{\mathrm{max\_eb}}}^{z=0} T^{\mathrm{EB}}_{\mathrm{AMOC}}(z,t)dz, \tag{2.12}$$

where $h_{\text{max\_eb}}(t)$ is the depth where the zero crossing between northward and southward flow occurs at each time step for $T^{\text{EB}}_{\text{AMOC}}(z,t)$.

As motivated in Section 2.1, $\Psi^{\text{EB}}_{\text{MAX}}(t)$ is computed using the densities observed at either EB1 or EBH. The profiles of transport per unit depth computed according to Eq. (2.10) using EB1 and EBH will be referred to as $T^{\text{EB1}}_{\text{AMOC}}$ and $T^{\text{EBH}}_{\text{AMOC}}$, respectively. The eastern-boundary density contributions to the AMOC computed from Eq. (2.12) will be referred to as $\Psi^{\text{EB1}}_{\text{MAX}}$ and $\Psi^{\text{EBH}}_{\text{MAX}}$, respectively.

2.4 Eastern-boundary hydrographic characteristics

Next we examine the hydrographic properties of the water masses observed at EB1 and EBH to explore whether the temporal fluctuations of the properties between the two sites are coherent. For this, we examine temporal anomalies. Both data sets cover the period from 4 March 2004 to 14 October 2007 (ca. 3.5 years of data). Notice that for clearer visualization, we plot and discuss temporal anomalies relative to the time mean of each separate deployment period (Figures 2.3 – 2.6). In all calculations based on density anomalies, however, we compute temporal anomalies relative to the time mean of the entire 3.5 years unless explicitly noted. Throughout this study fluctuations are reported in ± one standard deviation.

The density at EB1 shows the strongest anomalies near the surface (Figure 2.3a); these near-surface anomalies are mainly associated with temperature fluctuations (Figure 2.4a). This is most evident during the period from April 2005 to November 2005, when measurements are available as shallow as 120 m below the surface. Away from the surface, the major density and temperature anomalies are of uniform sign between the bottom and at least ca. 800 m, with the exception of the event in December 2006 (see below, Figure 2.3 and 2.4). Maximum mid-depth density anomalies are found near 1000 m over the whole period; we observe the most intense density anomalies during May 2005, August 2005, July 2006, December 2006, and February 2007. The positive density anomaly event with a maximum by the end of May 2005 at 1000 m lasts for 10 weeks, with the more intense anomalies (exceeding 0.02 kg/m^3) confined to a layer between 800 and 1500 m. This density event is associated with positive temperature and salinity anomalies of up to 0.35°C and 0.1 psu, respectively, but the latter have their maximum at ca. 800 m, while at the depth of the maximum density anomaly (ca. 1000 m) temperature and salinity anomalies of only -0.1°C and 0.03 psu are found. This implies that salinity dominates this density excursion near its maximum. There are three major events of anomalously negative density, all with similar characteristics, taking their extreme values at the end of August 2005, at the beginning of July 2006, and at mid-February 2007, respectively, and lasting for 5 – 6 weeks, 3 weeks, and 5 weeks, respectively. Negative density anomalies during the three events exceed 0.02 kg/m^3 at the depth interval between ca. 900 and 1500 m. During the August 2005

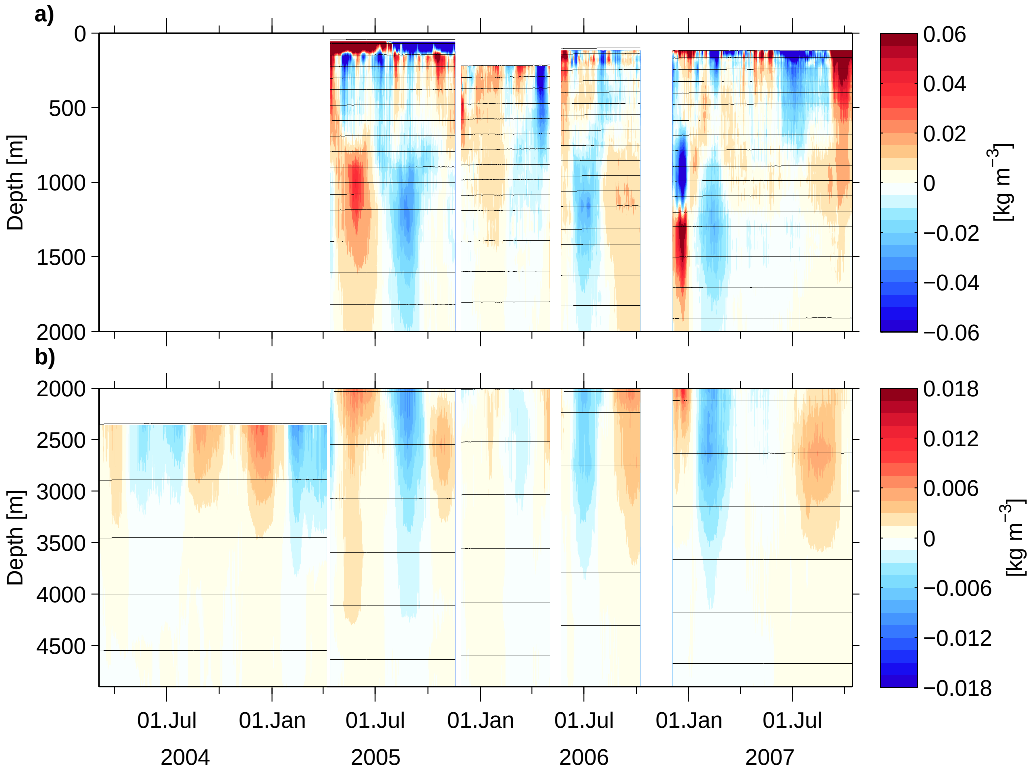

Figure 2.3: 2-day low-pass filtered in-situ density anomaly at EB1, (a) from 0 to 2000 m and (b) from 2000 m to the bottom. Dates go from 4 March 2004 to 14 October 2007. For clarity, the anomalies computed around the time mean for each deployment period are shown. Note that panels (a) and (b) have different color scales. Horizontal lines are the levels of the measurements

and July 2006 events, density minima occur at a deeper level than the corresponding salinity and temperature extrema. During December 2006, quite a different density anomaly can be identified, with two cores of opposite sign, negative in the range 600 – 1200 m and positive in the range 1200 – 2000 m. This event lasts for ca. 3 weeks, and the strongest anomalies are found at the end of December 2006, with temperature dominating the density anomaly (Figures 2.3a and 2.4a).

Some of these features seem to be water mass anomalies associated with local small-scale eddy circulations, rather than just temperature/salinity variations due to heave of density surfaces. When the cores of the temperature and salinity anomalies offset from the density anomalies, these usually occur near the zero of the density anomaly. This suggests that these are lenses (the isopycnals are expanded locally, meaning an-

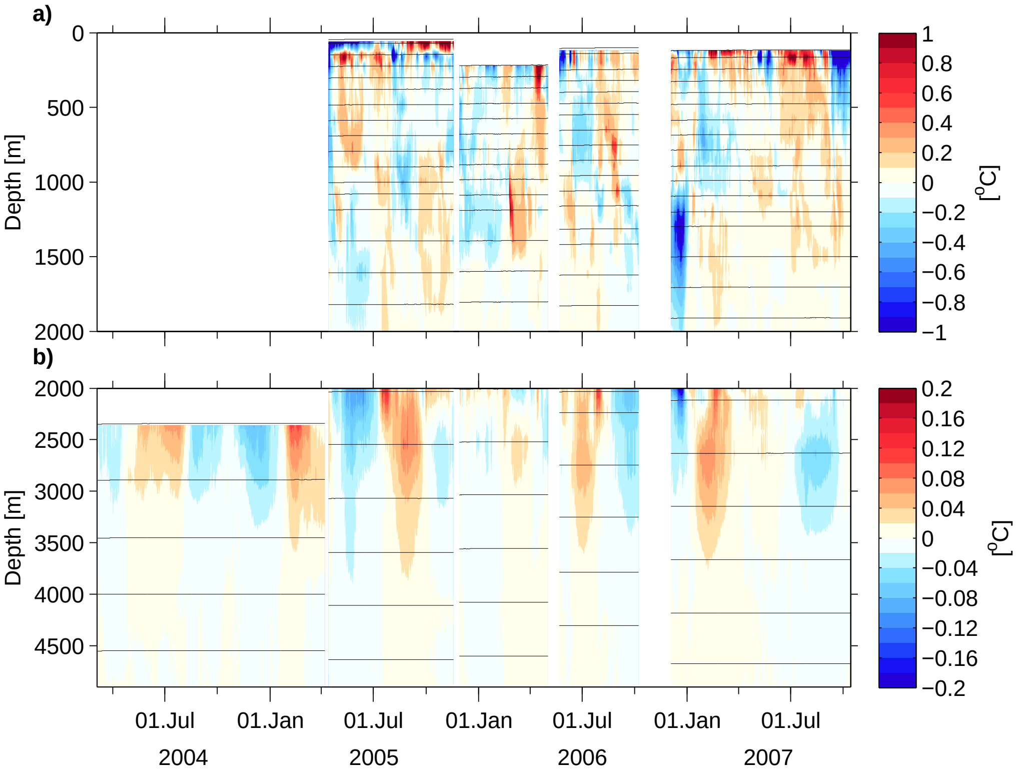

Figure 2.4: 2-day low-pass filtered temperature anomaly at EB1, (a) from 0 to 2000 m and (b) from 2000 m to the bottom. Dates go from 4 March 2004 to 14 October 2007. For clarity, the anomalies computed around the time mean for each deployment period are shown. Note that panels (a) and (b) have different color scales. Horizontal lines are the levels of the measurements.

ticyclonic circulation) or anti-lenses (the isopycnals are compressed locally, meaning cyclonic circulation) passing by the mooring. For instance, for the positive density event on May 2005 described above (Figure 2.3a), we observe that the core of the temperature (Figure 2.4a) and salinity (not shown) anomalies (ca. 800 m) offset from the core of the density anomaly (ca. 1000 m) (Figure 2.3a), suggesting that this is a salty anti-lens passing by the mooring.

Along the EBH array, the strongest density anomalies (exceeding ±0.1 kg/m^3) are found in the upper 500 m (Figure 2.5a), occasionally extending further down in the water column to up to 1400 m. Above 500 m, positive density anomalies that are persistent over longer periods (3 – 7 weeks) occur during April – May 2004, April – May 2005 and May 2007, while negative density anomalies that are persistent over longer periods

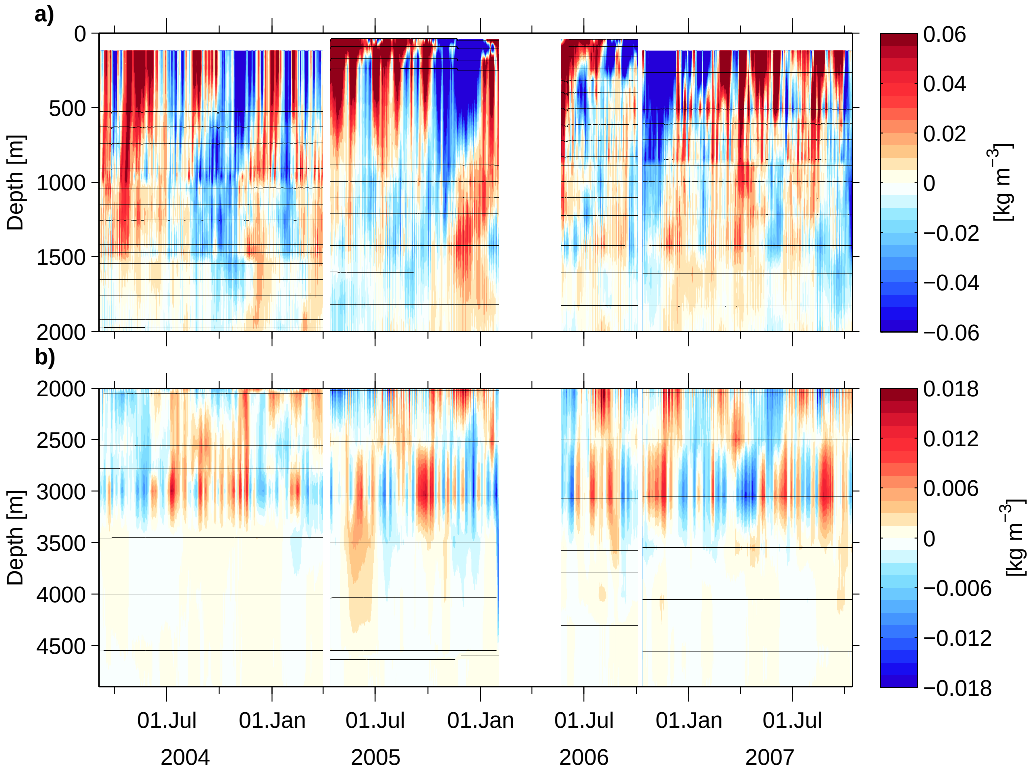

Figure 2.5: 2-day low-pass filtered in-situ density anomaly at EBH, (a) from 0 to 2000 m and (b) from 2000 m to the bottom. Dates go from 4 March 2004 to 14 October 2007. For clarity, the anomalies computed around the time mean for each deployment period are shown. Note that panels (a) and (b) have different color scales. Horizontal lines are the levels of the measurements.

(5 – 7 weeks) occur during October – November 2004, November – December 2005 and October – November 2006. The density anomalies in the upper ocean are dominated by temperature changes (Figure 2.6a). In December 2005, pronounced mid-depth maximum positive density anomalies of 0.04 kg/m^3 are found at 1300 m (Figure 2.5a); they are associated with pronounced temperature and salinity anomalies of respectively 0.7°C and 0.2 psu at the same depth level (Figure 2.6a). The anomalous warm salty water occurs at depths that are expected for mixing with Mediterranean water coming out of the Strait of Gibraltar at 36° N.

The vertical scales of the in-situ density anomalies at EB1 and EBH show pronounced differences (Figures 2.3 and 2.5). At EB1, density anomalies extend much deeper, throughout almost the entire water column, while at EBH the density anomalies are

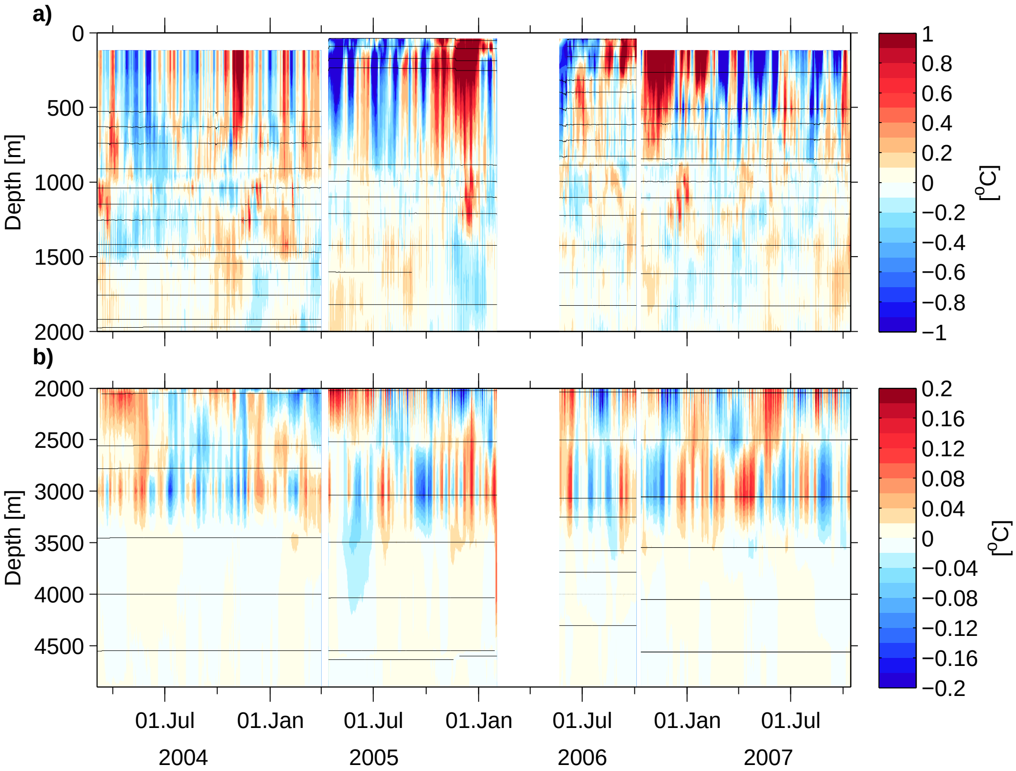

Figure 2.6: 2-day low-pass filtered temperature anomaly at EBH, (a) from 0 to 2000 m and (b) from 2000 m to the bottom. Dates go from 4 March 2004 to 14 October 2007. For clarity, the anomalies computed around the time mean for each deployment period are shown. Note that panels (a) and (b) have different color scales. Horizontal lines are the levels of the measurements.

stronger than at EB1 but they mainly occur in the upper 1400 m. The time scales of the anomalies are also different between EB1 and EBH. At EB1 the variability is dominated by long periods of a several weeks to several months, while at EBH density anomalies exhibit pronounced short-periodic variability with dominant periods around 13 days, superimposed on longer-periodic fluctuations.

A subset of the density anomalies at EBH (from November 2006 to October 2007) computed around the 3.5 year mean and band-pass filtered for the period 10 – 30 days, demonstrates that the 13-day oscillations are coherent down to 3500 m (Figure 2.7). Insufficient regularity of these features rules out fortnightly tidal forcing, and so their origin is unclear at present. This large vertical coherence gives us confidence in the sampling strategy at EBH, confirming that the variability is well captured by the *merging*

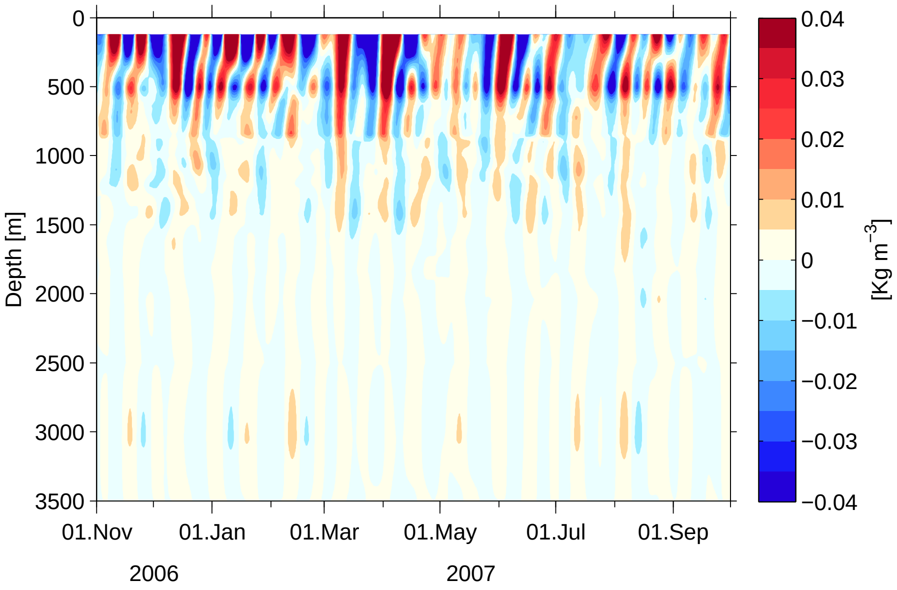

Figure 2.7: 10 – 30-day band-pass filtered in-situ density anomalies at EBH. Dates go from 1 November 2006 to 30 September 2007, because for better visualization only a subset of the 42-month long data set is displayed.

of the moorings distributed across the continental slope.

The temporal standard deviations of temperature, salinity and in-situ density at EB1 and EBH computed for the period between 13 April 2005 and 14 October 2007 (when both moorings have full-depth measurements) are shown in Figure 2.8. Both EB1 and EBH display the most pronounced differences in rms variability in temperature, salinity and density between 220 m and 800 m (Figure 2.8, Table 2.4). Amplitudes at EB1 are smaller than those at EBH above 800 m. At both sites, the largest variability is found in the uppermost level of measurements (220 m at EB1 and 120 m at EBH). At 220 m, variability in temperature, salinity, and density at EB1 is smaller than that at EBH by 0.38°C, 0.04 psu, and 0.04 kg/m^3, respectively. In particular, at 220 m rms density fluctuations are ±0.04 kg/m^3 at EB1 and ±0.08 kg/m^3 at EBH (Figure 2.8c). Temperature at EB1 exhibits maximum variability of ±0.45°C at the surface, with a local minimum of 0.15°C at ca. 900 m, and a local maximum of 0.2°C at ca. 1300 m. Temperature and salinity at EBH display maximum variability of ±0.95°C and ±0.16 psu respectively at the surface (120 m). At mid-depths, maximum variability differences between EB1 and EBH are found at ca. 1300 m, where temperature and salinity variability at EB1 exceeds that at EBH, as a result of the deep-reaching anomalies shown in Figures 2.3 and 2.4. However, there is no difference in density variability between EB1 and EBH at this depth level, indicating that even though temperature and salinity vary more at EB1, their variations are density-compensated such that there is no stronger signal in density at EB1. At both sites, the vertical distribution of rms variability in temperature is similar to that in salinity, with both properties fluctuating in-phase (Figure 2.8a and b).

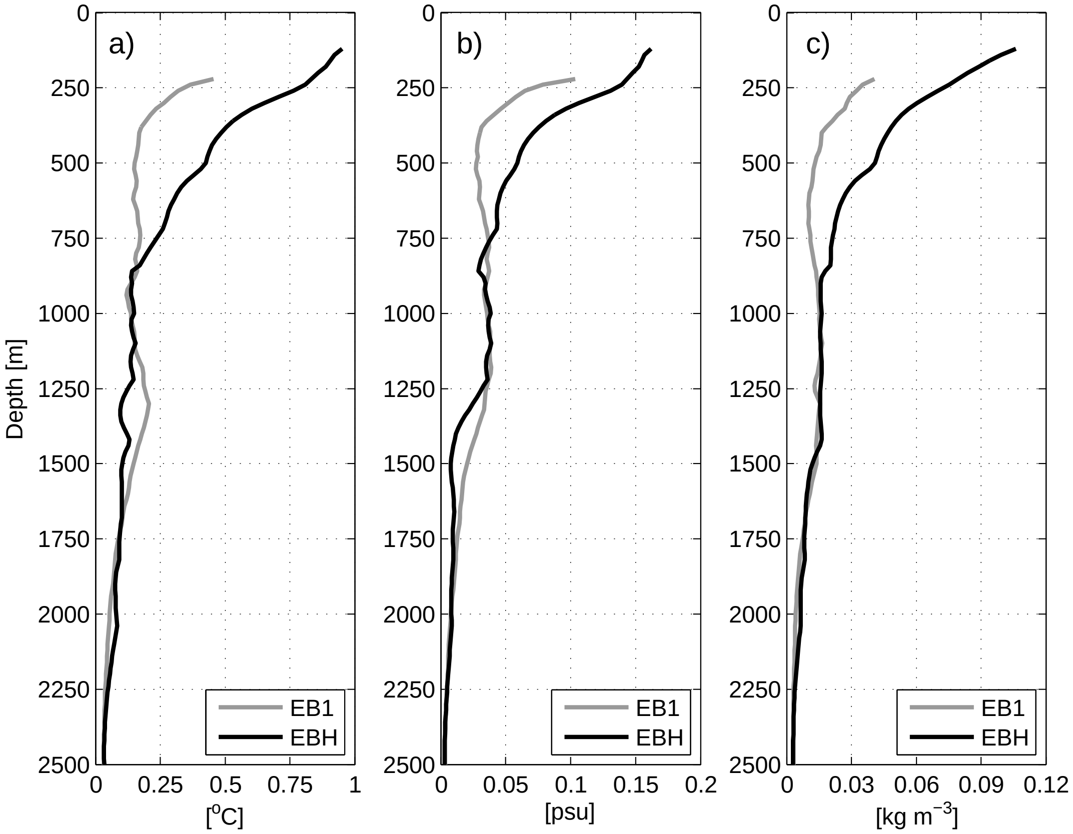

Figure 2.8: Standard deviation of (a) temperature, (b) salinity and (c) in-situ density at each depth level between the surface and 2500 m for EB1 (gray lines) and EBH (black lines). The standard deviation is computed for the period when both EB1 and EBH have full-depth measurements (13 April 2005 to 14 October 2007).

Depth		EB1			EBH	
[m]	T [°C]	S [psu]	ρ [kg/m^3]	T [°C]	S [psu]	ρ [kg/m^3]
220	17.22±0.45	36.44±0.10	1027.535±0.040	15.02±0.83	36.07±0.14	1027.761±0.079
500	12.07±0.15	35.63±0.03	1029.293±0.013	11.61±0.42	35.59±0.06	1029.354±0.041
760	8.70±0.17	35.22±0.04	1030.770±0.011	8.91±0.23	35.28±0.04	1030.780±0.021
1000	7.02±0.14	35.12±0.04	1032.051±0.015	7.52±0.15	35.22±0.04	1032.046±0.016
1260	6.22±0.19	35.18±0.03	1033.389±0.013	6.60±0.12	35.26±0.03	1033.390±0.016
1500	5.32±0.15	35.16±0.02	1034.587±0.014	5.52±0.10	35.193±0.008	1034.583±0.012
1760	4.51±0.09	35.09±0.01	1035.828±0.007	4.66±0.09	35.120±0.009	1035.824±0.008
2000	3.99±0.06	34.053±0.008	1036.944±0.004	4.04±0.08	35.061±0.008	1036.946±0.006
2500	3.25±0.03	34.986±0.003	1039.232±0.003	3.24±0.03	34.984±0.003	1039.231±0.003

Table 2.4: Time mean and standard deviation at selected depth levels between the surface and 2500 m of temperature (T), salinity (S), and in-situ density (ρ) at EB1 and EBH. The time mean and standard deviation is computed for the period when both EB1 and EBH have full-depth measurements (13 April 2005 to 14 October 2007).

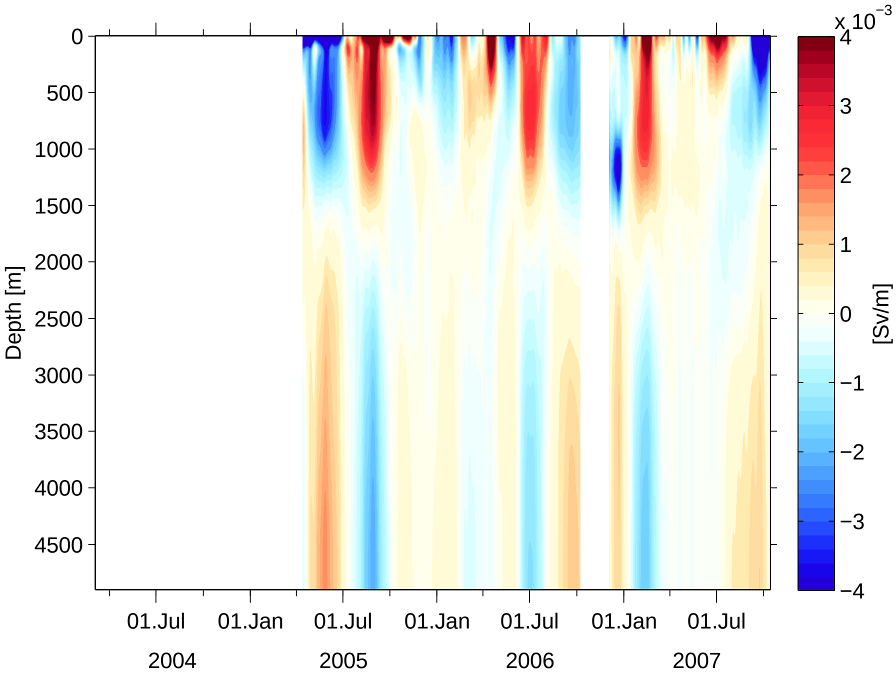

Figure 2.9: Anomalies (time mean subtracted) of the transport per unit depth as a function of time and depth, derived from EB1 ($T^{\mathrm{EB1}}_{\mathrm{AMOC}}$) and assuming steady western-boundary conditions. The data are 10-day low-pass filtered.

2.5 Transport variability

We now investigate how the differences between the density fluctuations at EB1 and EBH impact the estimates of basin-wide integrated transports. Unless otherwise noted, all the transport time series discussed here are 10-day low-pass filtered, in order to keep valid the assumption of transport compensation required for the computation of $\psi_{\mathrm{MAX}}(t)$ (Kanzow et al. 2007). Results for EB1 are shown only after April 2005, when measurements at EB1 covered the entire water column. A major difference between EB1 and EBH is that $T^{\mathrm{EB1}}_{\mathrm{AMOC}}$ (Figure 2.9) contains less energy at daily to weekly periods than does $T^{\mathrm{EBH}}_{\mathrm{AMOC}}$ (Figure 2.10), consistent with the density observations (Figures 2.3 and 2.5). Both $T^{\mathrm{EB1}}_{\mathrm{AMOC}}$ and $T^{\mathrm{EBH}}_{\mathrm{AMOC}}$ exhibit stronger fluctuations in the upper layer (above 1400 m for $T^{\mathrm{EB1}}_{\mathrm{AMOC}}$ and above 1000 m for $T^{\mathrm{EBH}}_{\mathrm{AMOC}}$) compared to the deeper layer. Below roughly 1500 m the fluctuations of $T^{\mathrm{EB1}}_{\mathrm{AMOC}}$ tend to be stronger than those of $T^{\mathrm{EBH}}_{\mathrm{AMOC}}$.

The vertical structure of the profiles is dominated by a first mode-like structure, as there is mostly one zero crossing over the record that is at a constant depth. However,

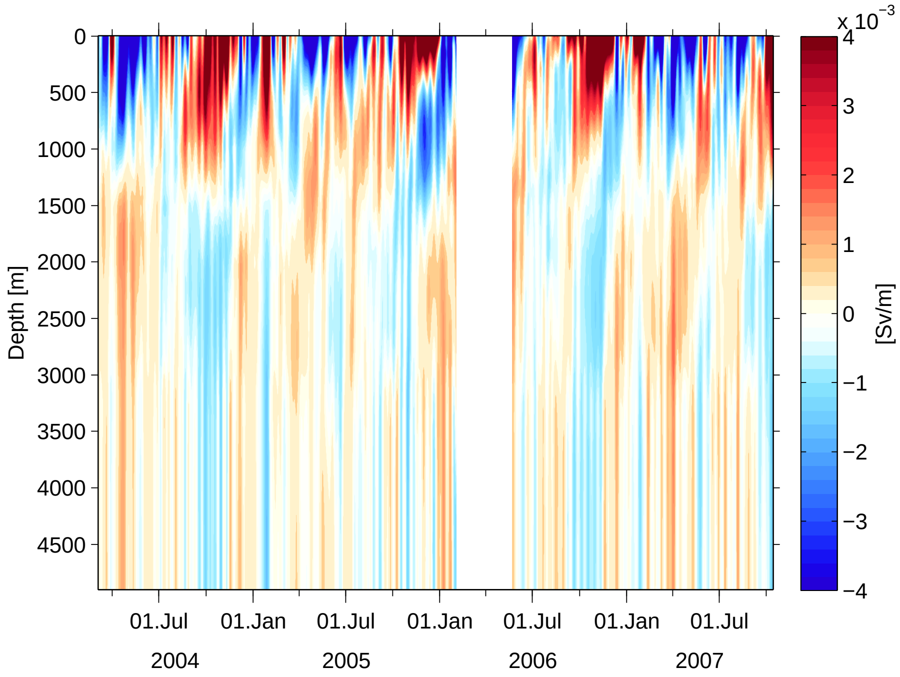

Figure 2.10: Anomalies (time mean subtracted) of the transport per unit depth as a function of time and depth, derived from EBH ($T^{\mathrm{EBH}}_{\mathrm{AMOC}}$) and assuming steady western-boundary conditions. The data are 10-day low-pass filtered.

there are exceptions to this pattern, when the vertical structure is more complex and displays two zero crossings. This occurs only during short periods, for instance from the beginning of July to the end of August 2007 for $T^{\mathrm{EB1}}_{\mathrm{AMOC}}$ (Figure 2.9), and from the beginning of August 2007 to the end of September 2007 for $T^{\mathrm{EBH}}_{\mathrm{AMOC}}$ (Figure 2.10).

The first empirical orthogonal function (EOF) modes both of the anomalies about a time-mean vertical profile of $T^{\mathrm{EB1}}_{\mathrm{AMOC}}$ and of $T^{\mathrm{EBH}}_{\mathrm{AMOC}}$ account for roughly 80% of the variance each, and both have large vertical shear in the upper ocean (Figure 2.11). A closer look reveals, however, that the first modes of $T^{\mathrm{EB1}}_{\mathrm{AMOC}}$ and $T^{\mathrm{EBH}}_{\mathrm{AMOC}}$ are very different. The zero crossing of the first EOF mode occurs 700 m deeper for $T^{\mathrm{EB1}}_{\mathrm{AMOC}}$ (1740 m) than for $T^{\mathrm{EBH}}_{\mathrm{AMOC}}$ (1076 m), in agreement with the deep-reaching density anomalies observed at EB1 (Figure 2.3). The first EOF mode of $T^{\mathrm{EB1}}_{\mathrm{AMOC}}$ shows two regions of strong shear above its zero crossing at 1740 m (above 200 m, possibly representing surface shear modes, Beckman, 1988; and between 1000 m and 1740 m). Between 200 m and 1000 m lies a region of weak shear. In contrast, the first mode of $T^{\mathrm{EBH}}_{\mathrm{AMOC}}$ has strong but monotonically decreasing shear between the surface and 1300 m, below its zero crossing at 1000 m; at 1300 m the shear drops abruptly. In the deep ocean, both $T^{\mathrm{EB1}}_{\mathrm{AMOC}}$ and

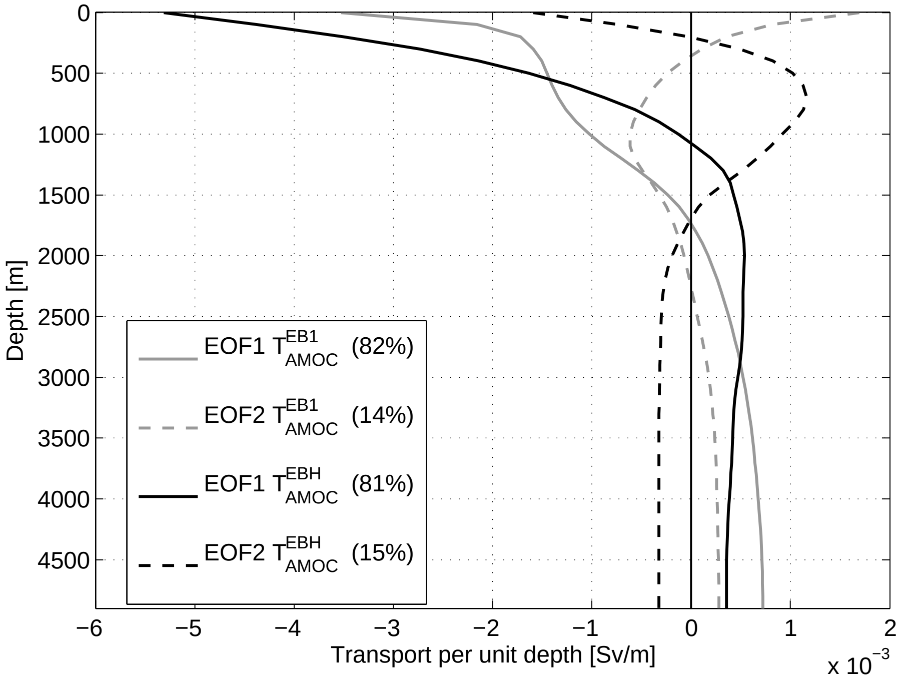

Figure 2.11: Vertical structure of the first and second vertical EOF modes of the anomalies (time mean subtracted) of the transport per unit depth profiles derived from EB1 and EBH ($T^{\mathrm{EB1}}_{\mathrm{AMOC}}$ and $T^{\mathrm{EBH}}_{\mathrm{AMOC}}$). The modes have been multiplied by the standard deviation of the corresponding principal components. The explained variance by each mode is given in brackets in the figure legend.

$T^{\mathrm{EBH}}_{\mathrm{AMOC}}$ exhibit less shear compared to the upper ocean, but $T^{\mathrm{EB1}}_{\mathrm{AMOC}}$ has more shear than $T^{\mathrm{EBH}}_{\mathrm{AMOC}}$. Below roughly 2870 m the amplitude of the first EOF mode of $T^{\mathrm{EB1}}_{\mathrm{AMOC}}$ is larger than for $T^{\mathrm{EBH}}_{\mathrm{AMOC}}$. As with the first mode, the second EOF mode of $T^{\mathrm{EB1}}_{\mathrm{AMOC}}$ (accounting for 14% of the variance) has deeper zero crossings and more shear in the deep ocean compared to the second EOF mode of $T^{\mathrm{EBH}}_{\mathrm{AMOC}}$ (accounting for 15% of the variance). These differences in vertical structure suggest that the dynamics governing the transport fluctuations are different at EB1 and EBH. Note that the vertical structures of the leading EOF modes of $T^{\mathrm{EB1}}_{\mathrm{AMOC}}$ and $T^{\mathrm{EBH}}_{\mathrm{AMOC}}$ show no obvious relationship to the vertical water mass structure. Notice also that despite the differences between the EOF modes, the depths of the zero crossings between northward and southward flow are very similar for $T^{\mathrm{EB1}}_{\mathrm{AMOC}}$ and $T^{\mathrm{EBH}}_{\mathrm{AMOC}}$, occurring on average at 1073 m (±44 m) for $T^{\mathrm{EB1}}_{\mathrm{AMOC}}$ and at 1080 m (±40 m) for $T^{\mathrm{EBH}}_{\mathrm{AMOC}}$.

We now focus on the fluctuations about the time mean of the overturning transport defined according to Eq. 2.12 using EB1 and EBH ($\Psi^{\mathrm{EB1}}_{\mathrm{MAX}}$ and $\Psi^{\mathrm{EBH}}_{\mathrm{MAX}}$, Figure 2.12).

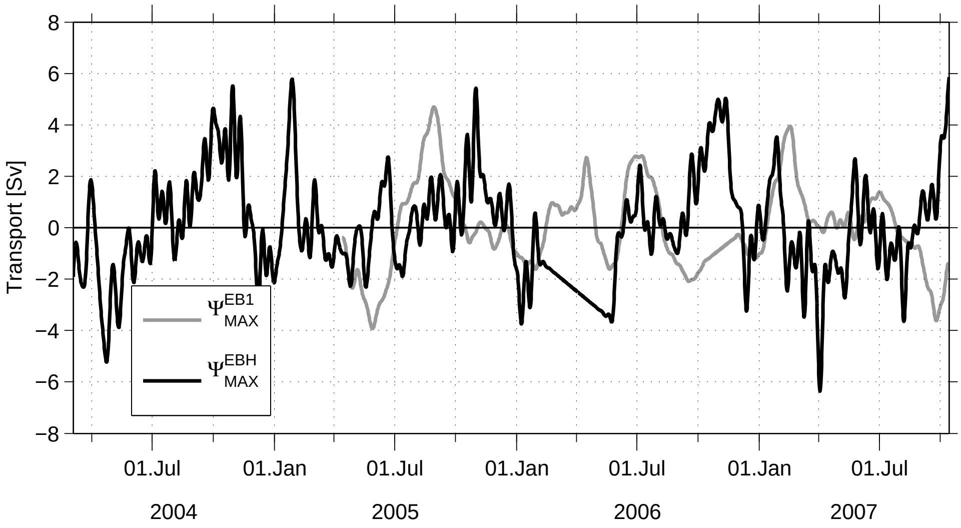

Figure 2.12: 10-day low-pass filtered anomalies of the eastern-boundary contribution to the AMOC at 26.5° N as derived form EB1 ($\Psi^{\mathrm{EB1}}_{\mathrm{MAX}}$, gray) and EBH ($\Psi^{\mathrm{EBH}}_{\mathrm{MAX}}$, black). Linear interpolation is chosen to fill the time gaps. Positive transports correspond to northward flow.

The maximum anomaly of $\Psi^{\mathrm{EB1}}_{\mathrm{MAX}}$ is 4.7 Sv on 29 August 2005, corresponding to the strongest negative density anomaly event (Figure 2.3), while the minimum anomaly is -4 Sv on 29 May 2005, corresponding to the strongest positive density anomaly event (Figure 2.3). This yields a maximum transport range of almost 9 Sv in $\Psi^{\mathrm{EB1}}_{\mathrm{MAX}}$. The maximum anomaly of $\Psi^{\mathrm{EBH}}_{\mathrm{MAX}}$ is 5.9 Sv on 14 October 2007, and the minimum anomaly is -6.3 Sv on 3 April 2007, giving a transport range of 12.2 Sv in $\Psi^{\mathrm{EBH}}_{\mathrm{MAX}}$. The 30-month record of the fluctuations of $\Psi^{\mathrm{EB1}}_{\mathrm{MAX}}$ has a standard deviation of ± 1.7 Sv, and the 42-month record of $\Psi^{\mathrm{EBH}}_{\mathrm{MAX}}$ has a standard deviation of ± 2 Sv (Figure 2.12). The integral time scale, obtained by integrating the autocorrelation function out to the first zero-crossing, is 24 days for $\Psi^{\mathrm{EB1}}_{\mathrm{MAX}}$ and 22 days for $\Psi^{\mathrm{EBH}}_{\mathrm{MAX}}$, resulting in 38 degrees of freedom (dof) in our time series of $\Psi^{\mathrm{EB1}}_{\mathrm{MAX}}$ and 62 dof in our (longer) time series of $\Psi^{\mathrm{EBH}}_{\mathrm{MAX}}$. Thus, there are 15 and 18 effectively independent measurements per year for $\Psi^{\mathrm{EB1}}_{\mathrm{MAX}}$ and $\Psi^{\mathrm{EBH}}_{\mathrm{MAX}}$, respectively. If we assume measurement errors negligible, we could resolve year-to-year changes of 0.6 Sv ($[(1.7^2/15{*}2)]^{1/2}$) for $\Psi^{\mathrm{EB1}}_{\mathrm{MAX}}$ and 0.6 Sv ($[(1.9^2/18{*}2)]^{1/2}$) for $\Psi^{\mathrm{EBH}}_{\mathrm{MAX}}$.

Although the variability of $\Psi^{\mathrm{EB1}}_{\mathrm{MAX}}$ and $\Psi^{\mathrm{EBH}}_{\mathrm{MAX}}$ differs by only 0.3 Sv in rms, their frequency distribution displays markedly different characteristics (Figure 2.13). Both $\Psi^{\mathrm{EB1}}_{\mathrm{MAX}}$ and $\Psi^{\mathrm{EBH}}_{\mathrm{MAX}}$ have dominant variance at low frequencies, and for periods longer than 50 days the spectra of the two time series are not significantly different. How-

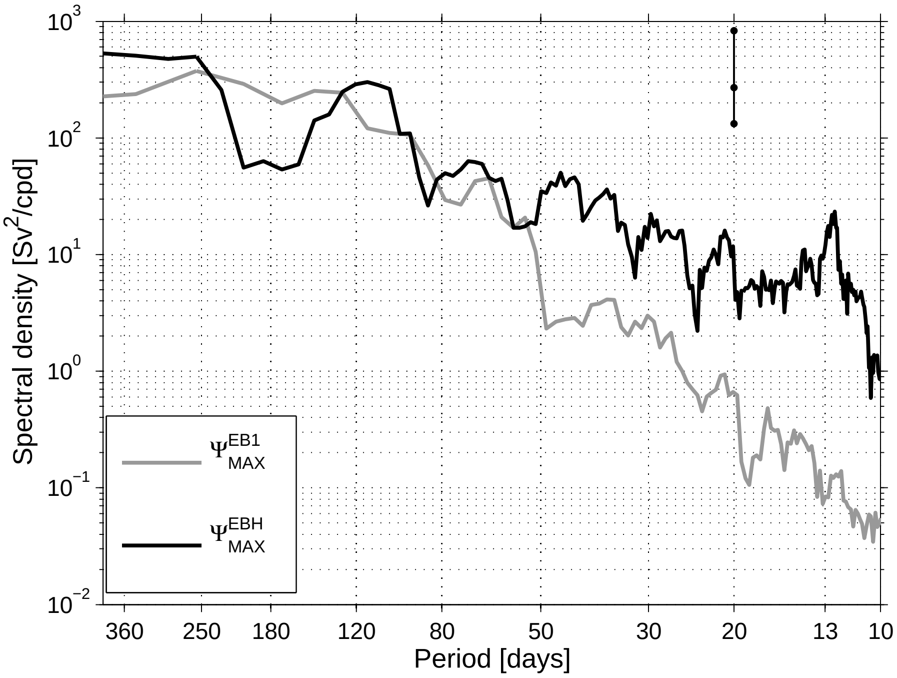

Figure 2.13: Power spectra of the 10-day low-pass filtered anomalies of the eastern-boundary contribution to the AMOC at 26.5° N as derived form EB1 ($\Psi^{\mathrm{EB1}}_{\mathrm{MAX}}$, gray) and EBH ($\Psi^{\mathrm{EBH}}_{\mathrm{MAX}}$, black). The vertical line in the upper right corner represents the 95% confidence interval. The power spectrum is computed following Percival and Walden (1993).

ever, for periods shorter than 50 days, the variance of $\Psi^{\mathrm{EB1}}_{\mathrm{MAX}}$ drops rapidly, such that for periods between 10 and 50 days the variance of $\Psi^{\mathrm{EB1}}_{\mathrm{MAX}}$ is a factor of 10 smaller than that of $\Psi^{\mathrm{EBH}}_{\mathrm{MAX}}$. Of the spectral peaks in $\Psi^{\mathrm{EBH}}_{\mathrm{MAX}}$, only the one around 13 days is clearly significant at the 95% confidence level; this peak is associated with the 13-day density variations that are coherent down to 3500 m (Section 2.4, Figure 2.7). A cross-correlogram of 50-day low-pass filtered time series of $\Psi^{\mathrm{EB1}}_{\mathrm{MAX}}$ and $\Psi^{\mathrm{EBH}}_{\mathrm{MAX}}$ fails to show significant correlation at any time lag between the two time series at the 95% confidence level (not shown), implying that we cannot identify potential westward signal propagation between the two sites through long Rossby waves.

The results presented here show that there is little agreement between the transports estimates from EB1 and EBH. There are considerable differences between EB1 and EBH in terms of amplitude, vertical structure and frequency distribution of the resulting mid-ocean geostrophic transport fluctuations. This implies that density fluctuations at the eastern boundary of the 26.5° N section need to be monitored across the continental slope. Mechanisms that are unrelated to the AMOC (such as basin-interior eddies) appear to influence strongly the density variability at EB1 on the time scales under consideration. In addition, the tall mooring EB1 is too far offshore to detect potential boundary waves and/or wind-induced processes near the coast (such as upwelling or Ekman pumping). We conclude that only the EBH data set should be used to compute the eastern-boundary density contribution to the AMOC. Analyzes in the remaining part of the paper will therefore rely entirely on EBH.

2.6 Seasonal variability

We now investigate the seasonal cycle in the density anomalies. Given that the observations span 42 months, the seasonal cycle represents the longest period that we can analyze with confidence. The monthly averages of in-situ density at selected depths levels (Figure 2.14) show that there is a pronounced seasonal variability in density right at the continental slope off northwest Africa at 26.5° N. Maximum values occur during spring (April/May) and minimum values during autumn (October/November). The seasonal cycle is coherent throughout the upper ocean and is surprisingly deep-reaching as it can be observed up to a depth of 1400 m. For all depth levels between 100 – 1400 m, the seasonal cycle is statistically significant.

As a result of the deep reaching seasonal cycle in density, there is also a pronounced seasonal cycle in the eastern-boundary contribution to the AMOC, as monthly means of the anomalies of $\Psi_{\mathrm{MAX}}^{\mathrm{EBH}}$ show (Figure 2.15). The observed seasonal density changes drive an enhanced southward upper mid-ocean flow in spring (April), resulting in a minimum in the $\Psi_{\mathrm{MAX}}^{\mathrm{EBH}}$, and vice-versa in autumn (October). The amplitude of the seasonal cycle of $\Psi_{\mathrm{MAX}}^{\mathrm{EBH}}$ is 5.2 Sv peak-to-peak, with the peak in April being statistically different from the peak in October.

2.7 Discussion

The largest density anomalies at the eastern-boundary continental slope (EBH) at 26.5° N are found in the upper 500 m of the water column, but they are often coherent down to 1400 m. The densities at EBH show 13-day fluctuations that are apparent down to 3500 m. The possible mechanism driving the 13-day density variability is not clear. Spectra of the wind field do not show any sign of dominant wind-driven forcing at this period. It can be expected that this phenomenon is associated with sea surface height anomalies; therefore a possible way to investigate the spatial scales associated with the 13-day period might be via satellite altimeter data. However, aliasing due to the insufficient temporal resolution (the Jason altimeter has a repeat cycle of 10 days) will make such an analysis problematic. The closeness of the 13-day fluctuations to the

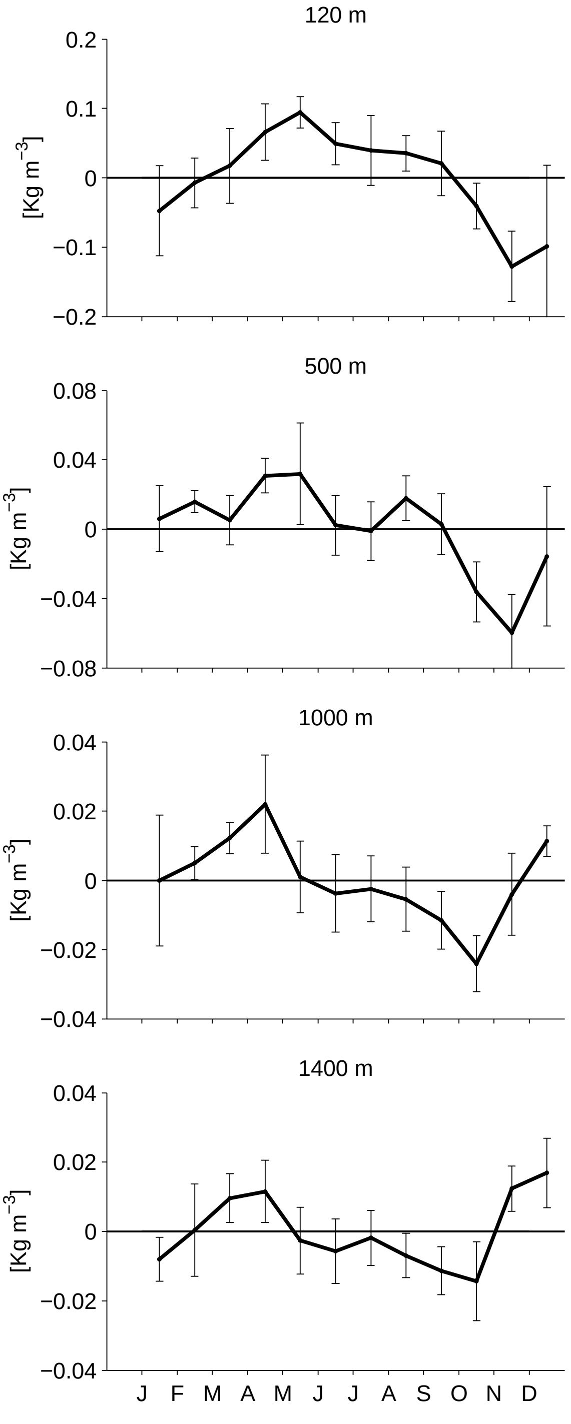

Figure 2.14: Monthly-mean in-situ density anomaly at EBH at selected depths. The bars indicate standard deviations of the monthly means. Note the change of the density scale.

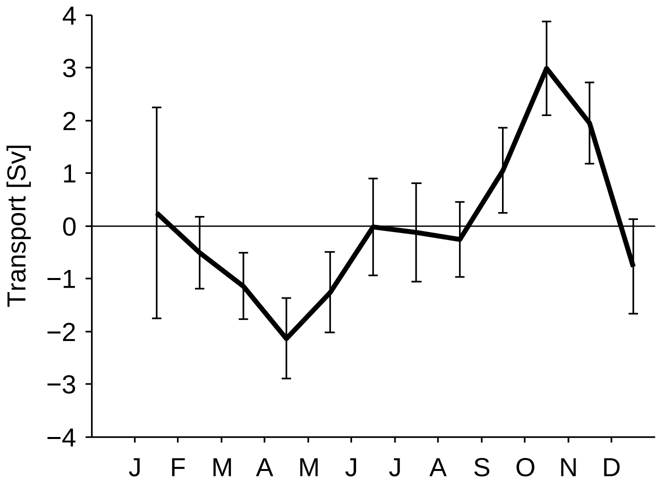

Figure 2.15: Monthly-mean anomalies of the eastern-boundary contribution to the AMOC at 26.5° N ($\Psi^{\mathrm{EBH}}_{\mathrm{MAX}}$). The bars show standard deviations of the monthly means.

fortnightly tidal periods could point to a tidal origin of this signal. However, fortnightly tidal fits applied to the EBH densities give rather different results for different depth levels (not shown), suggesting that the 13-day fluctuations are not regular enough to be tidal oscillations. It could be that the 13-day period is associated to variability induced by the eddy shedding south of the Canary Islands. However, the previously reported eddy generation sites are mostly south of Gran Canaria (distant from the shallower measurements at EBH) and subsequently the eddies tend to propagate downstream to the west (e.g., Sangrà et al. 2005, 2009). Therefore it seems unlikely that they can be responsible for the density variability observed at EBH. Furthermore, the density fluctuations we observe are coherent over a large depth range of up to 3500 m, while the maximum depth associated with anomalies of eddies shed by the Canary islands is roughly 1000 m (Piedeleu et al. 2009). Alternatively, the geometry of the semi-enclosed basin south of the Canary Island where we take our measurements might play a role in the generation of 13-day basin modes excited by stochastic wind forcing.

The temporal variability and the vertical structure of the transports derived from EB1 and EBH have different characteristics. The transports derived from EB1 show much less energy at periods shorter than 50 days, compared to the transports derived from EBH. The leading EOF transport modes show that the vertical shear of the transport arising from EB1 and EBH is especially different in the upper 1000 m. This points to different dynamics governing the density fluctuations at EB1 and EBH. Kanzow et al. (2010) show that the local wind forcing is very different, and much weaker, at

EB1 than EBH. Hence, local coastal wind forcing appears to play an important role in setting the variability at EBH. At EB1, the deep-reaching density anomalies may be linked to mesoscale eddies associated with the open ocean circulation. Contrary to the original planning (Marotzke et al. 2002), measurements at EB1 and EBH cannot serve as a backup for each other: densities need to be measured right at the continental slope to compute the eastern boundary density contribution to the AMOC.

Lee and Marotzke (1998) had proposed a decomposition of the meridional overturning circulation into three components, (i) the Ekman transport and its depth-independent compensation, (ii) the geostrophic shear associated with east to west density differences, and (iii) the contribution from barotropic velocities over sloping bathymetry (external mode). The Ekman contribution is not part of this study, and the eastern boundary contribution to the shear component is covered by the density measurements. But how about the external mode? Hirschi and Marotzke (2007) found in an eddy-permitting model of the Atlantic that the external mode mostly affected the time mean flow but not the temporal variability. They noticed that the external mode contribution to the AMOC becomes sizeable for large bottom velocities. For small bottom velocities the strength and vertical structure of the simulated AMOC (including the external mode) could be reconstructed reliably from eastern and western boundary densities as we attempted in this study. At 26.5° N (if at all) we expect the external mode to be relevant in the western boundary current system where large bottom velocities both in upper ocean (Antilles Current) and the deep western boundary current can occur (Johns et al. 2008). The direct current meter measurements across the western boundary continental slope are used to capture this contribution. At the eastern boundary, observations by Knoll et al. (2002) in the Lanzarote Passage at 29° N show that the mean bottom velocity close to 1200 m only amounts to -1.0 cm/s. In addition, at the deep part of EB1 the temperature fluctuations are of $O(10^{-2}\,^{\circ}\mathrm{C})$ (Figure 2.4, Section 2.4), therefore it can be expected that the bottom currents are small near EB1. Therefore our reconstruction of the AMOC from densities at the eastern boundary is unlikely to be affected significantly by a possible misrepresentation of the external mode.

The 10-day low-pass filtered 42-month long record of the eastern boundary contribution to the AMOC at 26.5° N, $\Psi^{\mathrm{EBH}}_{\mathrm{MAX}}$, has a temporal standard deviation of ±2 Sv. Kanzow et al. (2010) show that the overall AMOC variability is ±4.9 Sv and that the western boundary contribution of the mid-ocean section to the AMOC varies by ±2.3 Sv. The latter indicates that the western and eastern boundaries of the mid-ocean section contribute to the AMOC variability by roughly the same amount. This result contradicts earlier findings by Longworth (2007), who found from historical CTD measurements that the eastern boundary contribution was only half of that from the western boundary. However, the *total* western-boundary transport contribution to the AMOC also includes variability of the Gulf Stream and is hence significantly larger than that from the eastern boundary.

We find a pronounced deep-reaching seasonal cycle in eastern-boundary density, with maximum positive density anomalies in spring and negative ones in autumn, which are coherent between 100 m and 1400 m. These anomalies drive anomalous southward upper mid-ocean flow in spring, implying maximum reduction of the AMOC, and anomalous northward upper mid-ocean flow in autumn, implying maximum strengthening of the AMOC. The eastern boundary causes a peak-to-peak seasonal cycle of the AMOC of 5.2 Sv, clearly dominating the peak-to-peak seasonal cycle of the *total* AMOC of 6.7 Sv (Kanzow et al. 2010). This dominant influence is surprising and arises because western boundary transports do not display such a clear seasonal cycle when isolated in a similar fashion.The peak-to-peak amplitudes of the seasonal cycles of the remaining contributing components are 3.0 Sv, 2.1 Sv, and 3.9 Sv for T_{GS}, T_{EK}, and the western-boundary contribution of the mid-ocean section, respectively. Therefore, the rms of the seasonal amplitudes of all the components is 7.5 Sv, thus slightly larger than the 6.7 Sv of the total AMOC. This indicates that a small degree of compensation occurs between the components on seasonal time scales.

A detailed analysis of the mechanisms driving the seasonal density fluctuations is subject of ongoing work and is beyond the scope of this paper. We do, however, offer a preliminary analysis here. Several authors reported seasonal anomalies of the eastern boundary current system off Northwest Africa based on mooring-based measurements and hydrographic observations. A strong northward current during autumn close to the African shelf in the 1300 m deep channel between Lanzarote and Africa at 29° N was observed (Knoll et al. 2002; Hernández-Guerra et al. 2003). Knoll et al. (2002) found maximum southward flow in the upper 200 m in the middle of the channel between Lanzarote and Africa during spring. The seasonal northward transport in the Canary Current system is consistent with the anomalous northward transports (and minimum in in-situ density) we find in October (Figure 2.15). The phase of maximum southward flow during spring reported by Knoll et al. (2002) is consistent with the southward transports (and maximum in in-situ density) we find in April (Figure 2.15). This suggests a link with the variability we find in $\Psi^{\mathrm{EBH}}_{\mathrm{MAX}}$ but further analysis needs to be done on the variability of the eastern boundary current. A possible way to investigate this would be to compare the available current-meter time series at the Lanzarote passage (Hernández-Guerra et al. 2003) with our observations of $\Psi^{\mathrm{EBH}}_{\mathrm{MAX}}$. If good agreement is found, this would allow expanding the eastern-boundary AMOC time series back in time to January 1997 (when the current-meter measurements were initiated). This might be of potential importance for the re-construction of the AMOC before the start of the RAPID/MOCHA array in April 2004.

The Moroccan coastal upwelling undergoes seasonal changes induced by the coast-parallel trade winds. The band between 25° N and 43° N along the African coast exhibits strongest coastal upwelling during summer and autumn (e.g., Wooster et al. 1976; Mittelstaedt 1983). We observe maximum densities in April/May, two months earlier than the maximum upwelling occurs. Also coastal upwelling is thought to bring waters from 200 or 300 m depth to the surface. In contrast, our analysis suggests coherent seasonal density changes down to 1400 m. For these reasons coastal upwelling is unlikely to be the direct driver of the seasonal density and transport cycles. Instead, the vertical structure suggests a first baroclinic mode as a result of the displacement of the density surfaces induced by the wind stress curl. A preliminary analysis of the QuikSCAT-based SCOW (Scatterometer Climatology of Ocean Winds) seasonal wind stress curl climatology (Risien and Chelton 2008) reveals a pronounced seasonal cycle in eastern boundary wind stress curl, which leads the density anomaly by roughly 90 degrees or 3 months (Figure 2.16). The out-of-phase relationship is plausible, as uplifting of the density surfaces should prevail during the winter phases of enhanced cyclonic wind curl anomalies. Therefore maximum positive density anomalies can be expected in spring, when the transition from cyclonic to anti-cyclonic wind stress curl anomalies takes place. The summer period of anti-cyclonic wind stress curl then should lead to the observed maximum negative density anomalies in autumn as a result of the maximum depression of the density surfaces. The SCOW data set exhibits limitations in resolving the wind curl near the coast close to the mooring locations and needs to be further investigated.

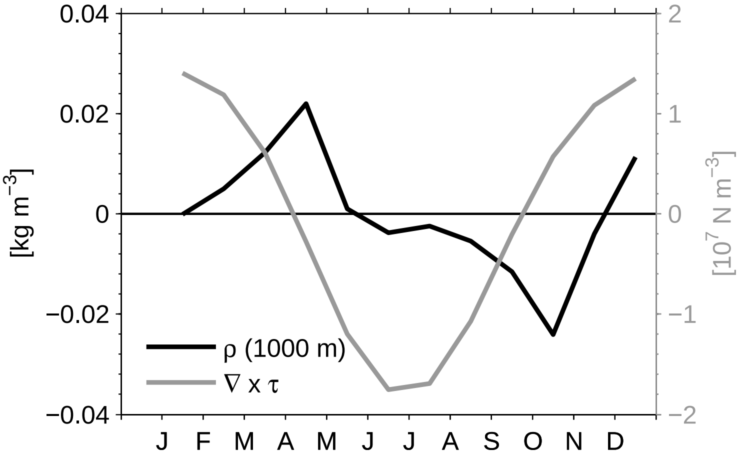

Figure 2.16: Monthly means of in-situ density anomaly at 1000 m from EBH (black), and seasonal cycle of wind stress curl ($\nabla \times \tau$) anomaly at 27° 7.5′ N, 15° 22.5′ W (about 200 km away from the position of the shallowest mooring at EBH), based on the SCOW climatology (Risien and Chelton 2008, gray).

2.8 Conclusions

Based on 3.5 years of moored temperature and salinity data at the eastern boundary of the Atlantic at 26.5° N from a tall mooring (EB1) located at the base of the continental rise (24° W) and an array of small moorings (EBH) distributed across the continental slope up to the Moroccan shelf (14° W), we find:

- Density anomalies at EBH are often coherent down to 1400 m; 13-day density fluctuations even reach down to 3500 m. This vertical coherence confirms the validity of the sampling strategy at EBH, including the merging of the profiles.

- There are significant transports between EB1 and EBH, so contrary to the original planning, measurements at EB1 cannot serve as backup for EBH. Density needs to be observed right at the continental slope as part of an AMOC monitoring strategy.

- Eastern-boundary density variations contribute ±2 Sv rms AMOC variability, similar to the contribution from the western boundary (east of the Bahamas) to the mid-ocean geostrophic component of the AMOC.

- The seasonal cycle in density at the eastern boundary is coherent between 100 m and 1400 m, with maximum positive and negative density anomalies in spring and autumn, respectively. Resulting is a minimum AMOC in spring and a maximum AMOC in autumn, with a peak-to-peak amplitude of the seasonal cycle of 5.2 Sv caused by the eastern boundary, which dominates the 6.7 Sv seasonal cycle of the total AMOC.

- At present the long-term contribution of eastern-boundary density variability to the AMOC is uncertain. The annual cycle at the eastern boundary, however, is larger than expected. This may mean that on longer time scales the contribution from eastern-boundary densities to the AMOC could be significant. Long-term sustained density measurements at EBH are necessary to quantify the role of eastern-boundary densities on AMOC changes at 26.5° N on inter-annual and longer time scales.

Chapter 3

Seasonal meridional transport fluctuations at 26.5° N

3.1 Introduction

The Atlantic Meridional Overturning Circulation (AMOC) at 26.5° N can be divided into three components: the Gulf Stream transport through the Straits of Florida, the zonally integrated Ekman transport, and the mid-ocean northward transport between the Bahamas and the African coast (Cunningham et al. 2007). The latter has two components, the transport through the western boundary wedge over the Bahamas continental slope and the geostrophic upper mid-ocean transport between the base of Bahamas continental slope and the African coast. Kanzow et al. (2010) showed that the seasonal fluctuations of the geostrophic component of the AMOC – upper mid ocean plus Gulf Stream transport (2.2 Sv and 1.7 Sv rms) – are substantially larger than the seasonal fluctuations of the Ekman transport (1.2 Sv rms). Further, they showed that the seasonal cycle in the upper mid-ocean geostrophic flow is the main driver of the seasonal cycle in the AMOC at 26.5° N. Johns et al. (2010)(manuscript in prep.) demonstrated that the upper mid-ocean geostrophic flow is responsible for the observed pronounced seasonal cycle inthe northward heat flux across 26.5° N. We have identified in Chapter 2 that the contribution of eastern-boundary density variability to the AMOC displays strong seasonal anomalies (5.2 Sv peak-to-peak). We found pronounced deep-reaching seasonal displacements of the isopycnals in the 100 – 1400 m depth range at the eastern boundary. They appear to drive the largest part of the seasonal cycle of the upper mid-ocean transport through changes in basin-wide zonally integrated baroclinic transport profile, as the isolation of the contributions from density at the western and the eastern boundary of the mid-ocean section to the upper mid ocean transport suggests.

For a better understanding of the seasonal transport anomalies it is essential to observe, whether they correspond to broad (basin scale) or localized (e.g. near ocean boundary) flows. Based on four transatlantic sections and climatologies at 24° N in the Atlantic, Baringer and Molinari (1999) found a pronounced seasonal cycle in the interior baroclinic heat flux (BHF), which presumably was caused mostly by anomalous advection of the mean temperature field (by the AMOC) rather than mean advection of anomalous temperatures. Their results showed that the annual cycle in BHF accumulated almost entirely at the western basin (their Figure 4), which would imply that the changes in the mid-ocean transport profile on seasonal timescales are dominated by flows near the western boundary. This result is inconsistent with the aforementioned pronounced seasonal density anomalies at the eastern boundary. The study of the zonal distribution of seasonal transports can be approximated by computation of the temporal evolution of the flow strength between the different dynamic height moorings along 26.5° N. However, the zonal resolution of this analysis would be limited by the zonal distance between the different moorings of O(1000 – 2000 km) in the basin interior (Figure 3.1).

In order to study both the zonal and meridional patterns of AMOC-related seasonal transport variability and the relation to eastern boundary densities, there is the need of putting the local information retrieved by RAPID/MOCHA in a wider context by comparison with other data sets. Several authors have analyzed the potential of using sea surface heights (SSH or η) as a qualitative and quantitative indicator for the temporal variability of meridional transports in the North Atlantic. This can be tested using the density moorings along 26.5° N. If good agreement between transport from mooring data and altimetry was found, altimetry could be used to study the zonal distribution of the seasonal transport cycle at a much better zonal resolution than that provided by the moorings. Kanzow et al. (2009) found that the basinwide zonal differences in η between the eastern and the western boundary basin margins cannot be used to infer basinwide fluctuations of the meridional upper mid-ocean flow at 26.5° N at subseasonal timescale. They argue that this is due to the complexity of the vertical structure of the flow near the western boundary that does not allow a clean projection of η on a first baroclinic modal structure in contrast to the situation offshore. However, they found significant positive correlations between upper-ocean transport integrated between the eastern boundary and different sites 40 and 500 km away from the western boundary and the difference in η between the corresponding section endpoints. These results are in line with those of Hirschi et al. (2009) based on numerical model simulations. In a modelling study Bingham and Hughes (2009) found that the sea surface height at the ocean margin might be a good indicator of the AMOC variability at interannual and longer timescales. Here we test whether the *seasonal* surface elevations from altimetric records can be related to *seasonal* upper mid-ocean transports at 26.5° N. If successful it would analyze the zonal structure associated with the observed, pronounced seasonal variability of the AMOC at a much higher spatial resolution than that set by the zonal separation of the RAPID/MOCHA moorings. Also, as high-quality altimetric heights are available from 1992 to present, the seasonal transport cycle could be computed over a long period of time.

However, seasonal η anomalies may not primarily be driven by geostrophic transport signals, which might compromise the interpretation of seasonal η signals in terms of circulation anomalies. Vinogradov et al. (2008) analyzed the mean seasonal cycle in sea level globally combining altimetric observations with a general circulation model over the period 1992 – 2004. They found that in the subtropical oceans a substantial part of the seasonal sea level variability (about 80%) can be attributed to changes in thermosteric height in the upper 100 m. Thus, the expected source of seasonal variability in sea surface height along 26.5° N is basin-scale coherent heating and cooling near the surface. Therefore, seasonal η anomalies are (to first order) dynamically inactive in terms of depth-integrated transport fluctuations because the zonal pressure gradients associated with this mechanism are small and are confined at the near-surface ocean. Instead, the previous findings (Chapter 2, Figure 2.14) imply that the dynamically-relevant density signal that dominates the seasonal cycle of the upper mid-ocean transports occurs close to the eastern continental margin and is coherent from the surface to 1400 m.

Using the continuous in-situ density measurements from the moorings distributed along the 26.5° N transect from the RAPID/MOCHA array, we investigate the relationship between mooring-derived dynamic heights and η, with a focus on seasonal timescales. For this, we test the degree to which seasonal anomalies of η can be linked to the vertical density structure at the mooring locations. In particular, we test whether a robust relationship can be established between η and dynamic height from in-situ density measurements at the eastern boundary. If a good agreement is found, altimetry may be an efficient tool to estimate the representativeness in time or the meridional scale of our four-year-long record of density measurements at the eastern boundary. Finally, we analyze the seasonal upper ocean zonally integrated transports across five discrete segments defined by the mooring locations from RAPID/MOCHA along 26.5° N, as well as the zonally integrated transports between the African coast and each of the moorings distributed along 26.5° N and how they add up to the whole basinwide interior upper mid-ocean transport. This is relevant for the interpretation of the pronounced seasonal variability of the AMOC and its possible driving mechanisms, as a seasonal flow pattern with large spatial scales should be associated with the large scale forcing pattern, while a boundary-confined flow might point to either localized wind forcing or boundary wave propagation.

The chapter is organized as follows. In Section 3.2 we present the underlying data and methods. Section 3.3 presents the comparison between dynamic heights from in-situ density measurements and η with a focus on seasonal variability at the eastern boundary. In Section 3.4 we analyze the upper mid-ocean transports in the various segments across 26.5° N, and compare them with the corresponding zonal differences in η. In Section 3.5 we discuss our results, and we conclude in Section 3.6.

3.2 Data and methods

3.2.1 Data

The RAPID/MOCHA array became operational since April 2004 to continuously monitor the strength and vertical structure of the AMOC (Kanzow et al. 2008b). To monitor the upper mid-ocean transport it makes use of an array of moorings measuring temperature, salinity, and pressure near the western boundary (mooring sites WB2, WBH1, WBH2, WB3, and WB5; see Johns et al. (2008) for details), on the flanks of the Mid-Atlantic-Ridge (MARW, and MAR2), and near the eastern boundary (EB1, EBHi, EBH0 – EBH5, EBM1 – EBM7). The sensors distributed at discrete depth levels acquire temperature, salinity and pressure at a sampling rate between 15 and 30 minutes. The data are 2-day low-pass filtered and subsampled on a half-daily grid (Kanzow et al. 2007) (see also www.noc.soton.ac.uk/rapidmoc). Subsequently the temperature, salinity, and pressure profiles are vertically interpolated onto a regular 20-dbar grid by applying an interpolation technique that relies on weighted sums of upward and downward integrals of climatological temperature and salinity gradients between vertically adjacent sensor levels following Johns et al. (2005). At the eastern-boundary continental slope, temperature, salinity, and pressure from all the eastern-boundary moorings have been merged into one profile covering the depth range from the sea floor up to the shallowest available level during each deployment (EBH) (Kanzow et al. (2007); see also Chapter 2, Section 2.2.2). Finally, density is computed from the temperature, salinity, and pressure profiles. The vertical density profiles at the western (WB2) and eastern boundaries (EBH) are used to estimate the basinwide zonally integrated mid-ocean transport (Cunningham et al. 2007). For this study, we focus on EBH (at the eastern continental slope) and the five full-depth density moorings (counting with 11 – 24 MicroCATs distributed over depth): WB2, WB3, and WB5, located 16, 40 and 500 km east of the Bahamas; MARW, located on the western flank of the Mid-Atlantic ridge; and EB1, located 1250 km west of the African Coast (Figure 3.1).

The satellite derived sea surface height comes from the gridded multi-satellite merged altimeter data set DT-MSLA 'Upd' (Delayed-time maps of sea level anomalies 'updated') provided by AVISO (information online at http://www.aviso.oceanobs.com). The data processing is described in Dibarboure et al. (2008). The temporal coverage span the period between October 1992 and April 2008 and has a nominal temporal resolution of 7 days. The nominal spatial resolution is of 1/3°. The underlying satellite missions include TOPEX/Poseidon, Jason-1, European Remote Sensing Satellite-2 (ERS-2), and Envisat. The satellite derived sea surface height is linearly interpolated in space from the standard grid onto the nominal mooring positions. Along EBH array, the position of EBH4 is chosen for the interpolation.

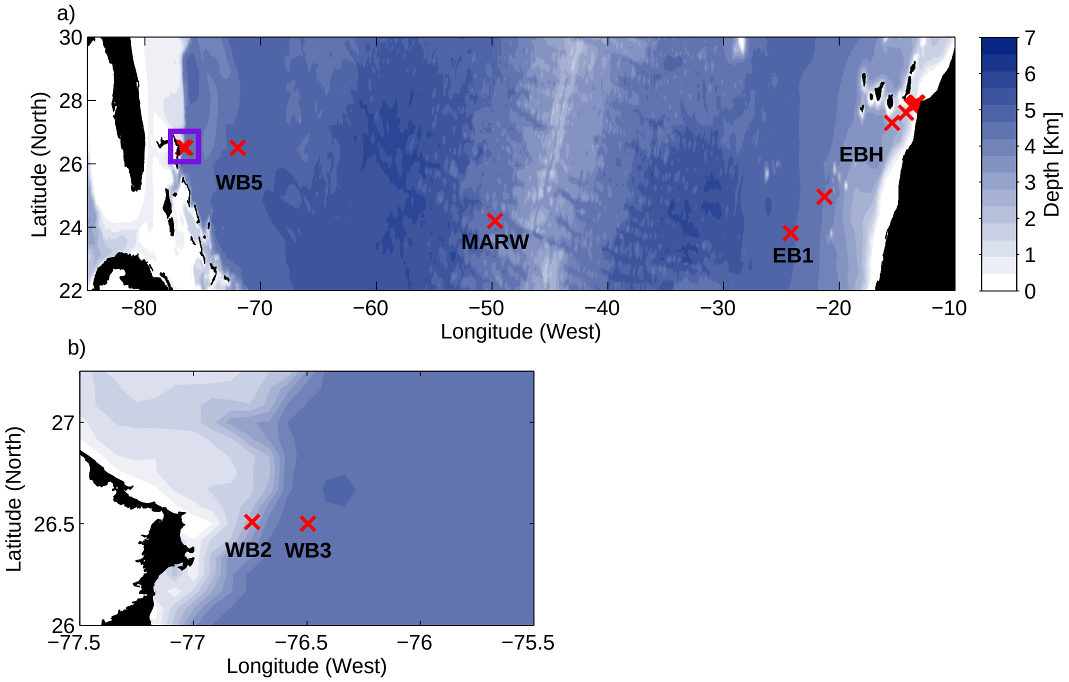
a)
30
28
26
24
22
Latitude (North)
WB5
MARW
EB1
EBH
−80
−70
−60
−50
−40
−30
−20
−10
Longitude (West)
7
6
5
4
3
2
1
0
Depth [Km]
b)
27
26.5
26
Latitude (North)
WB2
WB3
−77.5
−77
−76.5
−76
−75.5
Longitude (West)

Figure 3.1: (a) Distribution of the RAPID/MOCHA moorings across 26.5° N as deployed for year 2007 and (b) zoom of the purple square in (a) to better visualize the positions of WB2 and WB3. Only the locations of the moorings used in this chapter are shown.

3.2.2 Methods

In order to evaluate the origin of the seasonal transport signal along 26.5° N a set of estimates of upper mid-ocean meridional transports along 26.5° N are computed as follows. First, we evaluate northward geostrophic transports across five segments along the 26.5° N transect defined by the mooring locations. Between the eastern and western boundaries, there are four locations with full-depth moored density measurements, thus five zonal segments across the ocean interior are evaluated: WB2 – WB3, WB3 – WB5, WB5 – MARW, MARW – EB1, and EB1 – EBH. Then we integrate the meridional geostrophic velocity in a cumulative way between the African coast and the five mooring sites distributed along 26.5° N (i.e., east of WB2, east of WB3, east of WB5, east of MARW, and east of EB1) to analyze the extent along 26.5° N to which there is a seasonal transport signal associated with eastern boundary densities at EBH and how each of the transport contributions add up to the whole seasonal upper mid-ocean transport between WB2 and EBH. All the calculations are done for the period between April 2004 and April 2008 (except for calculations concerning EB1 when full-depth measurements are available from April 2005 onwards). The zonally integrated northward geostrophic volume transport (per unit of depth) between two mooring sites ('site W' and 'site E'), relative to a reference level z_{ref} up to the shallowest common level of measurements (h_u) from the two moorings is computed from the continuous observations of density profiles at each site according to

$$T^{\mathrm{INT}}_{\mathrm{site\ W-site\ E}}(z,t) = -(g/\rho f) \int\limits_{z'=-h_\mathrm{ref}}^{z} [\rho_{\mathrm{site\ E}}(z',t) - \rho_{\mathrm{site\ W}}(z',t)]dz' \qquad (3.1)$$

for -h_ref < z < -h_u, where ρ is a reference density and f is the Coriolis parameter. Based on our previous analysis, the depth where the zero crossing between northward and southward flow occurs for our estimations of the transport per unit depth $T^{EB}_{AMOC}(z,t)$ arising from isolating the eastern-boundary density variability contribution to the AMOC is found at a nearly constant value of 1080 m (Chidichimo et al. 2010, see also Chapter 2). Given that the distribution of the level of no motion along 26.5° N is unknown, we compute the transports relative to h_ref = 1080 m up to the common available level of measurements (h_u) from the two moorings. To get estimates of the transports per-unit-depth at the surface at each time step, we extrapolate the transport profiles obtained with Eq. (3.1) from h_u to the sea surface on the basis of the vertical gradient of the transport estimates between the two uppermost level of measurements. Finally, we integrate the resulting volume transports from the sea surface to h_{max} = 1080 m according to

$$T^{\mathrm{UO}}_{\mathrm{site\ W-site\ E}}(t) = \int\limits_{z=-h_\mathrm{max}}^{z=0} T^{\mathrm{INT}}_{\mathrm{site\ W-site\ E}}(z,t)dz. \qquad (3.2)$$

As each variable is a function of time, the mentioning of the time dependence will be omitted hereafter. The transports from Eq. (3.2) evaluated for the segments WB2 – WB3, WB3 – WB5, WB5 – MARW, MARW – EB1, and EB1 – EBH will be referred to as $T^{\mathrm{UO}}_{\mathrm{WB2-WB3}}$, $T^{\mathrm{UO}}_{\mathrm{WB3-WB5}}$, $T^{\mathrm{UO}}_{\mathrm{WB5-MARW}}$, $T^{\mathrm{UO}}_{\mathrm{MARW-EB1}}$, and $T^{\mathrm{UO}}_{\mathrm{EB1-EBH}}$, respectively. Similarly, the transports from Eq. (3.2) evaluated east of WB2, east of WB3, east of WB5, east of MARW, and east of EB1, will be referred to as $T^{\mathrm{UO}}_{\mathrm{WB2-EBH}}$, $T^{\mathrm{UO}}_{\mathrm{WB3-EBH}}$, $T^{\mathrm{UO}}_{\mathrm{WB5-EBH}}$, $T^{\mathrm{UO}}_{\mathrm{MARW-EBH}}$, $T^{\mathrm{UO}}_{\mathrm{EB1-EBH}}$, respectively. These transports will be compared to the corresponding zonal η differences between the section endpoints used for the calculations of the transports. As shown by Kanzow et al. (2007), the upper mid-ocean transport variability at periods shorter than 10 days may not be related to AMOC fluctuations. Therefore unless otherwise mentioned all the transport time series have been 10-day low-pass filtered. The anomalies (time-average subtracted) of transports and of the zonal η differences will be discussed.

3.3 Dynamic height from moored density measurements and satellite sea surface height

The purpose of this section is to analyze wether altimetric observations of η can provide useful information related to fluctuations in dynamic height computed from in-situ moored density measurements at the mooring locations along 26.5° N. In particular, we test whether the fluctuations of the altimetric observations of η at the deployment locations of the RAPID/MOCHA moorings can be linked to the changes found in the vertical density structure. Our emphasis lies on seasonal time scales.

First we examine the fluctuations about the time mean of both dynamic heights determined from in-situ density measurements (the geopotential anomaly relative to the sea floor divided by the Earth's gravitational acceleration – hereafter referred to as DH) and η for the overlapping period when there are available data from all the moorings and from altimetry (from April 2004 to April 2008, except at EB1 where full-depth density measurements are available from April 2005 onwards). The DH time series have been 10-day low-pass filtered, unless otherwise mentioned.

At all the mooring locations, the rms variability of DH at 220 m (the shallowest common depth level of measurements where there are available data for all the moorings) is smaller than the rms variability of η (Figure 3.2; Table 3.1). Thereby suggesting that a fraction of the variability of DH at all the mooring sites is contained in the upper 200 m. Along 26.5° N, the rms variability both of DH and η is largest at WB5 (Figure 3.2c) (see also Bryden et al. 2009), with the large variability most likely associated with the presence of eddies and Rossby waves in the ocean interior (Kanzow et al. 2009). Historical current meter measurements at WB5 have also revealed evidence for intense ocean-bottom-intensified (topographic) waves (see Zantopp et al. 1998). The smallest rms amplitudes of DH and η along 26.5° N are found at EB1 (Figure 3.2e), with the rms variability of η, however, being about two times larger than that in DH. The latter implies that the fraction of rms variability in DH contained in the upper 200 m is quite large at EB1. One interesting aspect is that while near the western boundary the rms variabilities of both DH and η is much larger in the ocean interior (WB3 to MARW) than at the boundary (WB2), near the eastern boundary we find the opposite situation since the rms variability offshore (EB1) is smaller than at the African coast (EBH). The latter suggests that offshore the eastern boundary near EB1 the eddy variability is very small.

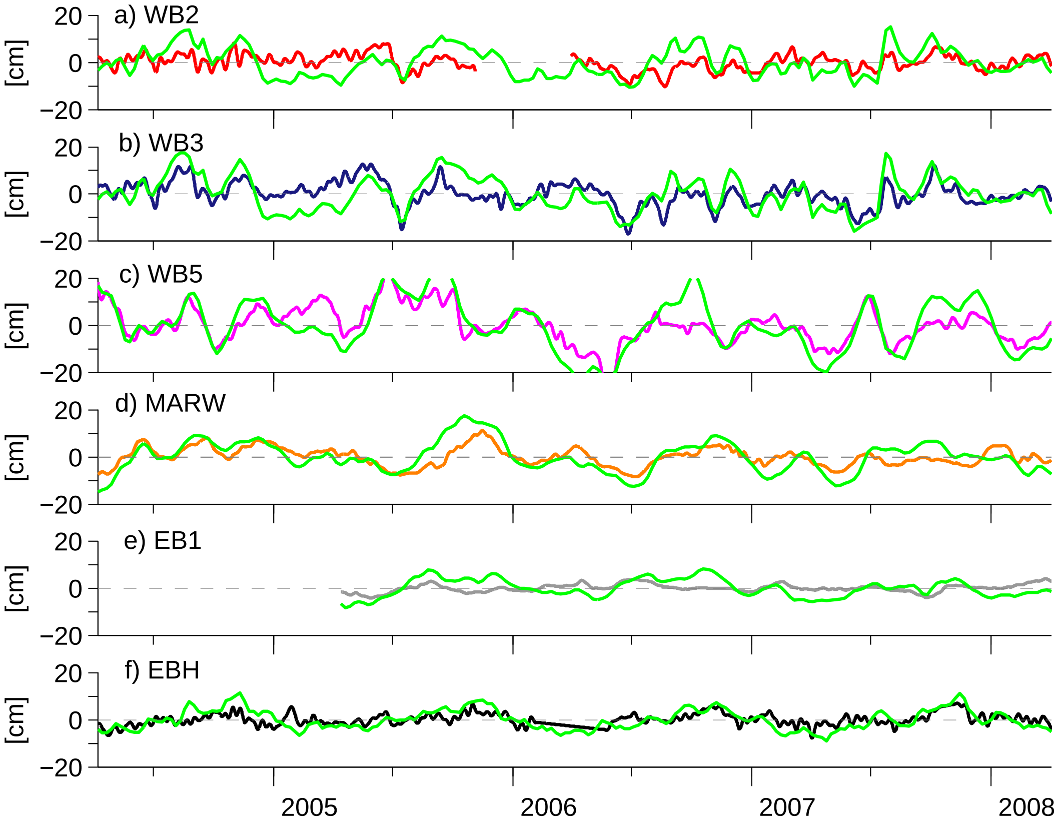

Figure 3.2: Dynamic height anomalies at 220 m (dynamic cm; geopotential anomaly relative to the sea floor divided by the Earth's gravitational acceleration) derived from in-situ density at (a) WB2, (b) WB3, (c) WB5 ,(d) MARW, (e) EB1, and (f) EBH. The green lines represent fluctuations of η [cm] interpolated onto the mooring positions.

Site	DH std dev [dyn. cm]	η std dev [cm]	correlation (DH and η)
WB2	3.3 (–)	6.1	0.27 (–)
WB3	5.0 (6.3)	7.3	0.59 (0.64)
WB5	7.7 (10.9)	10.9	0.80 (0.90)
MARW	3.9 (5.4)	6.5	0.72 (0.71)
EB1	1.6 (–)	3.7	0.31 (–)
EBH	2.5 (3.0)	4.2	0.62 (0.64)

Table 3.1: Columns 2-3 show standard deviation (std dev) of 10-day low-pass filtered mooring derived dynamic height (DH; geopotential anomaly divided by the earth's gravitational acceleration) at 220 m (shallowest common measurement level for all the moorings) and η interpolated at the mooring locations. Column 4 indicates the correlation of the DH with η at the mooring locations. The values in parentheses correspond to standard deviations and correlations computed considering DHs at the shallowest level of measurements for the full density record at each individual site (220 m for WB2, 60 m for WB5, 120 m for MARW, 220 m for EB1, and 120 m for EBH). All the time series span the period April 2004 to April 2008 except for calculations concerning EB1 (April 2005 to April 2008).

The DH fluctuations at WB3, WB5, MARW, and EBH display significant correlations (at the 95% confidence level) with η at the same locations of 0.59, 0.80, 0.72, and 0.62, respectively (Figure 3.2; Table 3.1). Right at the western boundary, the DH fluctuations at WB2 are not significantly correlated at a 95% confidence level with η. At EB1, there is very little correspondence between DH and η, and they exhibit a low (0.31) but barely significant correlation (at 95% confidence) (Table 3.1). The correlations between DH at the shallowest level of available measurements at WB3 (120 m), WB5 (60 m), MARW (120 m), and EBH (120 m) and η at the same locations, however, is only slightly larger (or very similar) (values in parentheses, Table 3.1) than the one arising from considering DH at 220 m. Note that the shallowest level of available measurements at WB2 and EB1 is 200 m and 220 m, respectively, thus it is not possible to make the same comparison. Based on Vinogradov et al. (2008) findings, however, if the largest portion of the seasonal cycle of DHs is mostly contained in roughly the upper 100 m, it would be expected a larger agreement between the DHs at a level shallower than 220 m and η at the same locations. Vinogradov et al. (2008) and Ivchenko et al. (2008) found that on seasonal timescales fluctuations of η in the subtropical oceans are mainly associated with near-surface basin-scale seasonal thermosteric changes. Thus, the seasonal anomalies in η should evolve in phase and with similar amplitudes across the basin. Next we investigate whether there is a well-defined seasonal cycle in η at the positions of the moorings by computing the average seasonal cycle for the same period of the mooring records (from April 2004 to April 2008). To establish the representativeness of the 4-year-interval the long-term average seasonal cycle will also be computed from the altimetric observations since 1992 (start of TOPEX/POSEIDON).

The average seasonal cycles of anomalies of η at the mooring positions (Figure 3.3) exhibit a similar phase with maxima in autumn and minima in the first half of the year, and zero crossings during summer and winter. The seasonal cycles of η at WB2, WB3, and WB5 (Figure 3.3a-c) exhibit quite similar characteristics. At the three sites the seasonal anomalies of η are in phase with each other with maxima in autumn and (not so well defined) minima in spring. The mean monthly standard error decreases as the western boundary is approached, being larger at WB5 (±4.4 cm) than at WB3 (±2.7 cm) and WB2 (±1.7 cm). This indicates that the eddy signal, which might cause aliasing originating from averaging the random eddy field, is largest in the ocean interior (WB5) and then it decreases towards the boundary (WB2). The average seasonal cycles of the short record of η at MARW (Figure 3.3d) show a minima in April and a maxima in November. The average standard error is of ±2.0 cm, suggesting that the record also might contain aliasing due to eddy variability. The best-defined seasonal cycles of η (with less month-to-month variability) along 26.5° N can be observed near the eastern boundary at EB1 and EBH (Figure 3.3e-f) with well-defined maxima in autumn and minima in spring, and clearly significant above the mean standard errors of ±1.1 cm and ±0.4 cm, respectively. One striking feature is the pronounced peak in autumn of η at EBH (in November) that is different at the other sites (in September or October).

Next we explore if the average seasonal cycle of η between April 2004 and April 2008 is representative of much longer periods. At all the mooring sites both amplitude and phase of the seasonal cycles of η computed from the 4-year-long record are consistent with the ones computed from the 15-year-long record starting in 1992. The monthly anomalies of η at MARW during March and November, however, seem to be biased high in the short record by roughly 2.5 cm. The high value in November is associated to the strong η fluctuations during November 2005 (Figure 3.2d). Thus, the long-term seasonal cycle of η at MARW is in better agreement with the seasonal cycles of η at EB1 and EBH, than the the seasonal cycle from the short record of η at MARW. At EB1 the monthly value in September appears to biased slightly low with respect to the long record due to intraseasonal anomalies in the short record, but this is just barely significant. It can be seen that the seasonal cycles computed from the long record of η at EB1 and EBH are very similar both in amplitude and phase.

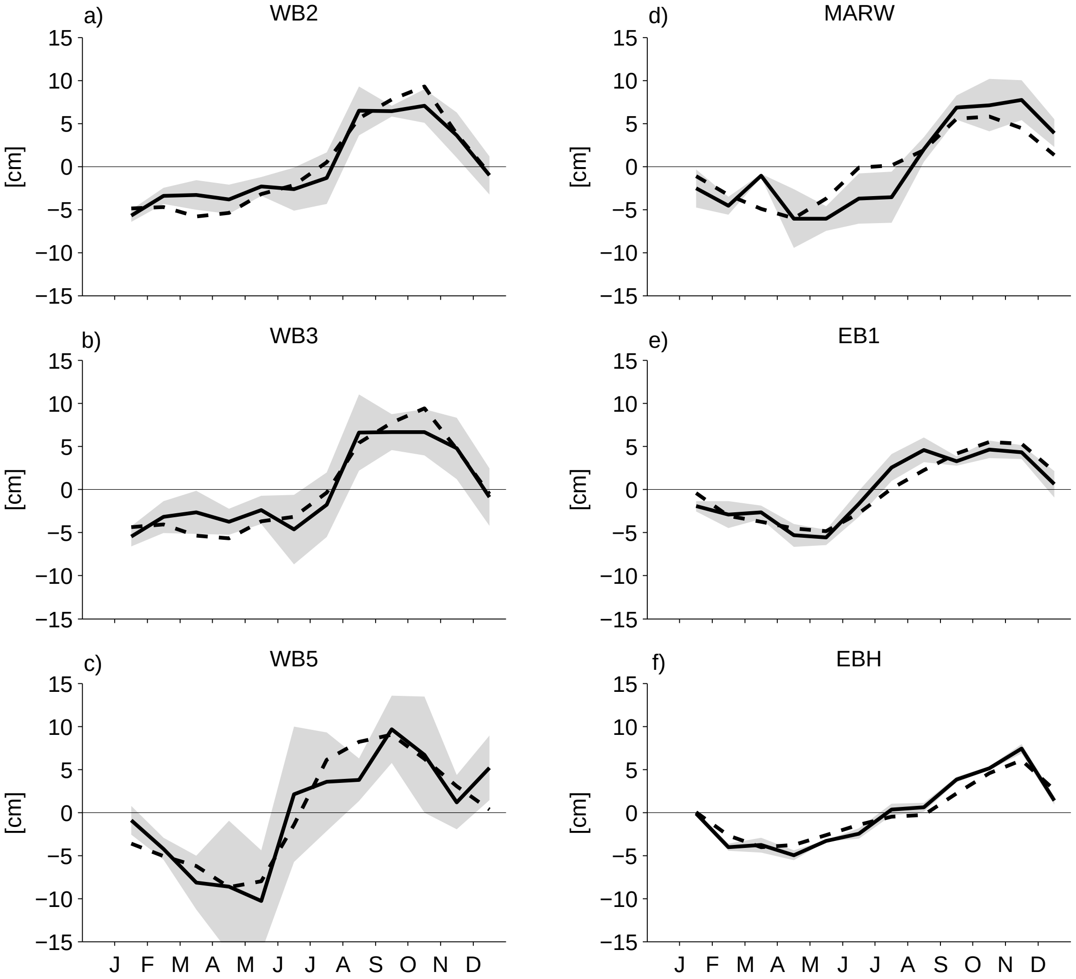

Figure 3.3: Monthly-mean anomalies of η computed for the period between April 2004 and April 2008 (solid black lines) at the positions of (a) WB2, (b) WB3, (c) WB5, (d) MARW, (e) EB1, and (f) EBH. The grey envelopes represent the standard error of each month (obtained from the 3 – 4 realizations of monthly averages available for each month). The dashed lines are the monthly-mean anomalies based on the 15-year long record of η starting in October 1992.

The results show that there is a basin-scale coherent seasonal variability in η across 26.5° N which has less month-to-month variability at the eastern boundary compared to the rest of the basin. This conclusion is valid both for the period 2004 to 2008 and the period 1992 to 2008.

If heating and cooling only affect a thin layer in the upper ocean, seasonal anomalies of η will mostly constitute a dynamically inactive component and thus might not be representative of seasonal AMOC-related transports. Next, we explore if the average seasonal cycles of DH from the moorings distributed along 26.5° N show average seasonal cycles that are similar to those of η in terms of phase and amplitude, as this could be relevant for the interpretation of the seasonal changes in the AMOC (see section 3.1).

The computed seasonal cycles of DHs at 220 m reveal that the only site along 26.5° N where there is a clear agreement in phase and amplitude between the seasonal cycles in DH and η is at EBH (Figure 3.4f). In contrast, the seasonal cycles of DHs at 220 m at WB2, WB3, WB5, MARW and EB1 do not bring out a clear seasonality (Figure 3.4a-e). This suggests that the seasonal heating and cooling at depth shallower than 220 m dominate η at these sites. At WB2 and WB3, the lack of agreement between the seasonal cycles of DH and η points to the complexity of the dynamics near the western boundary. A closer look reveals that at WB5 and MARW the average monthly means of DH and η show some degree of correspondence between peaks. However, this partial agreement arises due to aliasing in the monthly averages of DHs and η originating from long-periodic eddy variability at these sites (Figure 3.4c-d) since no significant seasonal density anomalies are found below 220 m at WB5 and MARW (not shown). At EB1, there is very little correspondence between the seasonal cycles of DH and η (Figure 3.4f).

As the main interest lies in the eastern boundary region, we now concentrate on comparing in more detail the seasonal cycles of DH and η at EB1 and EBH (Figure 3.5). At EB1 there is very little correspondence between the seasonal anomalies of DH at 220 m and η at the same location. In contrast, the seasonal anomalies of DH at 220 m at EBH (significant above the mean standard error of ± 0.5 cm) and η at the same location have the same phase (April minimum and November maximum) (Figure 3.5). This suggests that the deep vertical density structure is different at both sites. The average seasonal cycles of η at EB1 and at EBH are in reasonable agreement. At EB1 the average seasonal cycle computed between April 2005 and April 2008 has a peak-to-peak amplitude of 8.8 cm (10.2 cm between April 2004 and April 2008; see Figure 3.6) with a maximum in October and a minimum in May, while at EBH the peak-to-peak amplitude is 12.3 cm peak-to-peak, thus slightly larger than at EB1, with a maximum in November and a minimum in April. The long-term seasonal cycles of η at EB1 and at EBH, however, exhibit a peak-to-peak amplitude of 10.3 cm and 10.1 cm, respectively, indicating that the slightly larger amplitude of the seasonal cycle of η at EBH than at EB1 between April 2004 and April 2008 is not representative of long periods.

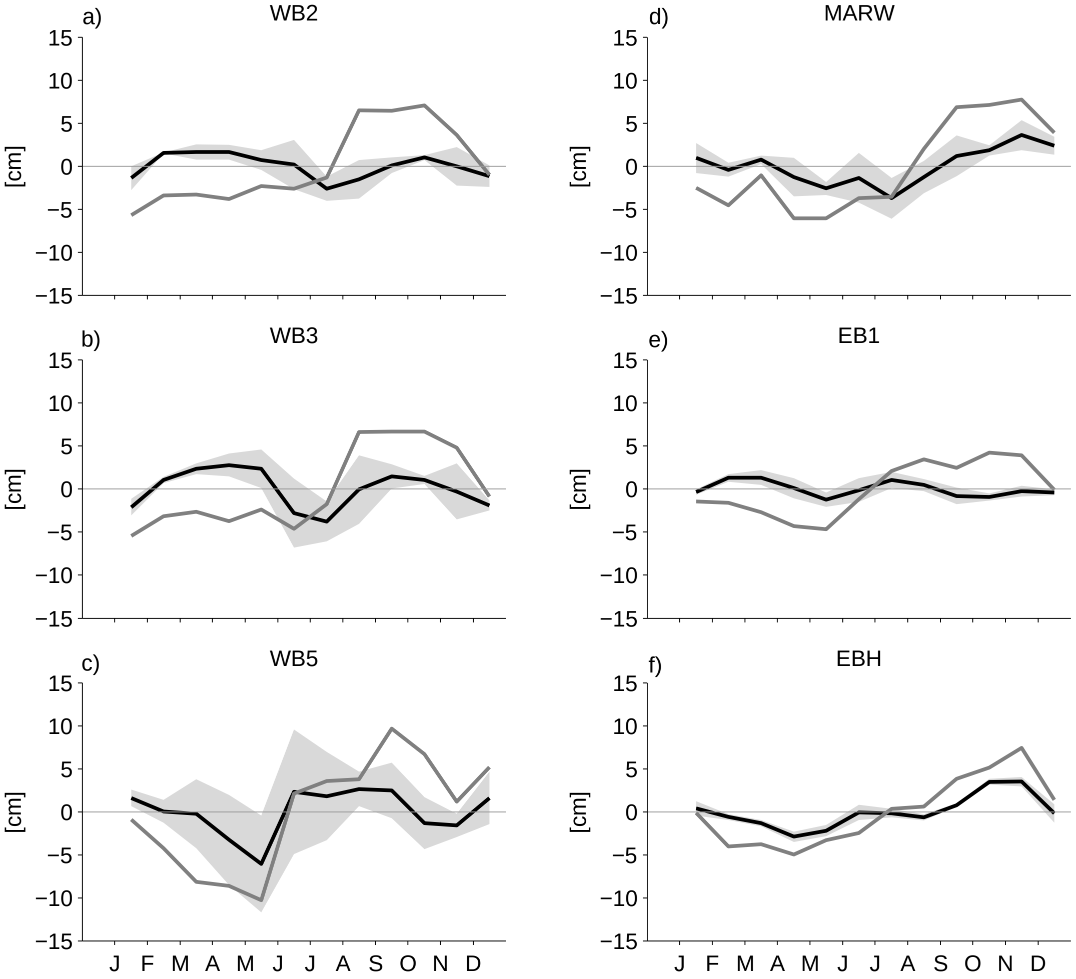

Figure 3.4: Monthly-mean anomalies (solid black lines) of the time series of DH at 220 m at the positions of (a) WB2, (b) WB3, (c) WB5, (d) MARW, (e) EB1, and (f) EBH computed for the period between April 2004 and April 2008 (April 2005 to April 2008 at EB1). The grey envelopes represent the standard error of each month as in Figure 3.3. The grey lines are the monthly-mean anomalies of η interpolated onto the mooring positions.

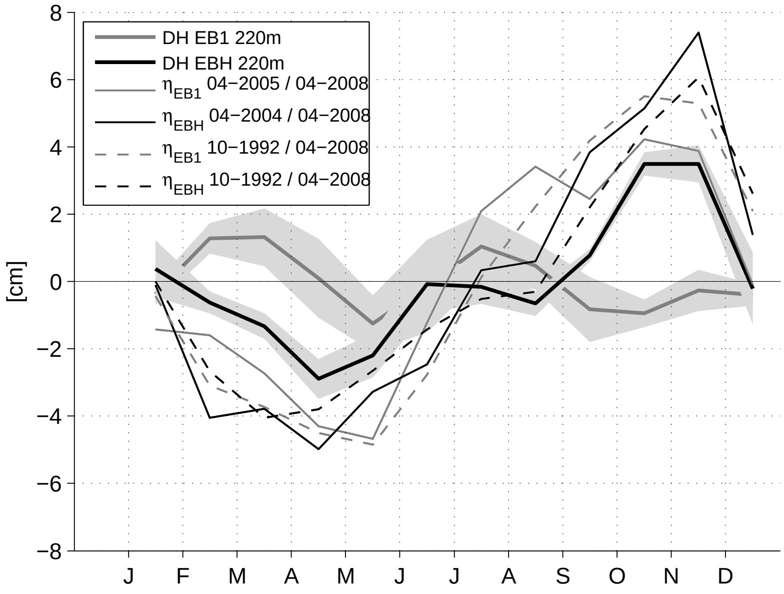

Figure 3.5: Monthly-mean anomalies of DH at 220 m at EB1 (thick grey line), DH at 220 m at EBH (thick black line), η at EB1 (between April 2005 and April 2008) (thin grey line), η at EBH (between April 2004 and April 2008) (thin black line). The dashed lines are the monthly-mean anomalies based on the 15-year long record of η at EB1 (dashed grey line) and η at EBH (black dashed line) starting in October 1992. The grey envelopes represent the standard error of each month as in Figure 3.3. The monthly standard errors of η at EB1 and EBH are not shown here for clarity.

The comparison of the peak-to-peak amplitude of the seasonal cycles of η at EBH (12.3 cm) and DH at 120 m at EBH (8.1 cm) indicates that about 65% of the amplitude in the seasonal cycle of DH at EBH comes from below 120 m (Figure 3.6). If there are deep seasonal deep-density anomalies below 100 m at EBH that are in phase with the shallow heating and cooling cycle in the upper ocean at EBH, it would be expected that the seasonal cycle of η at EBH is larger than at EB1. A simple approach to test this is to add the seasonal cycle of η at EB1 (which should be mostly associated with shallow heating and cooling in the upper ocean) to the seasonal cycle of DH at 120 m at EBH (which is associated to the deep seasonal signal at EBH) and compare it to the seasonal cycle in η at EBH. If the shallow heating and cooling cycle was similar at EB1 and EBH, the resulting seasonal amplitude should then be comparable to the seasonal amplitude of η at EBH. However, the resulting seasonal amplitude of the sum of η at EB1 and DH at 120 m at EBH is much larger than the seasonal amplitude of η at EBH (17.8 cm vs. 12.3 cm) (Figure 3.6). It is therefore plausible that the heating and cooling cycle at EBH is smaller than at EB1 or that at EBH the seasonal signal is redistributed in the vertical. The latter probably associated with the strong near coastal wind stress curl (Chapter 2, Section 2.7).

Figure 3.5 suggests that the deep vertical density structure is very different at EB1 and EBH. We explore now the vertical seasonal density structure at EB1 and EBH by comparing monthly mean anomalies of in-situ density at both sites at selected depth levels during the period when both moorings have full-depth measurements (April 2005 to April 2008). Note that the extrema of the density cycle will be of opposite sign of that of DH. There is no sign of significant seasonal density variability below the upper 200 m at EB1, as the seasonal anomalies of in-situ density show (Figure 3.7), in strong contrast there are pronounced coherent density anomalies at EBH reaching beyond 1000 m (see also Chidichimo et al. 2010). This confirms that the seasonal signal at EB1 occurs much shallower than at EBH (sallower than 220 m).

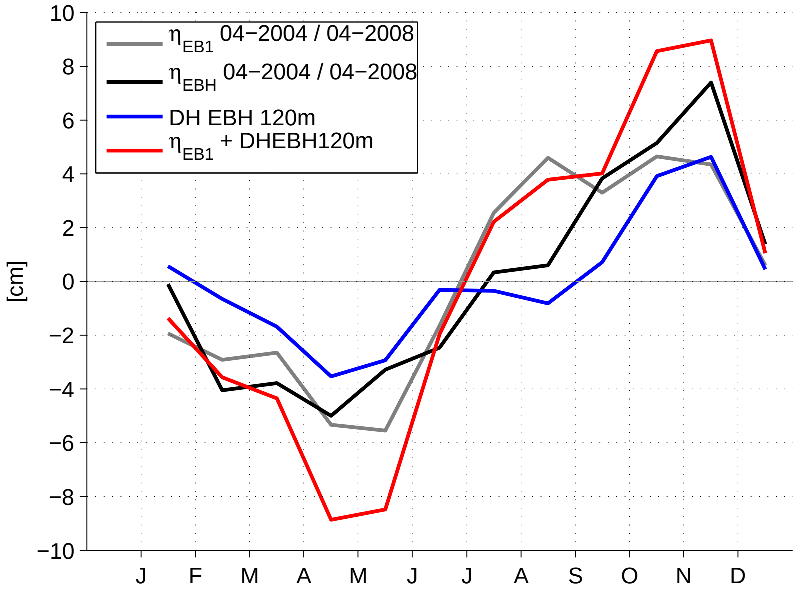

Figure 3.6: Monthly-mean anomalies of η at EB1 (between April 2004 and April 2008) (grey line), η at EBH (between April 2004 and April 2008) (black line), DH at 120 m at EBH (blue line), and the sum of η at EB1 (between April 2004 and April 2008) and DH at 120 m at EBH (red line).

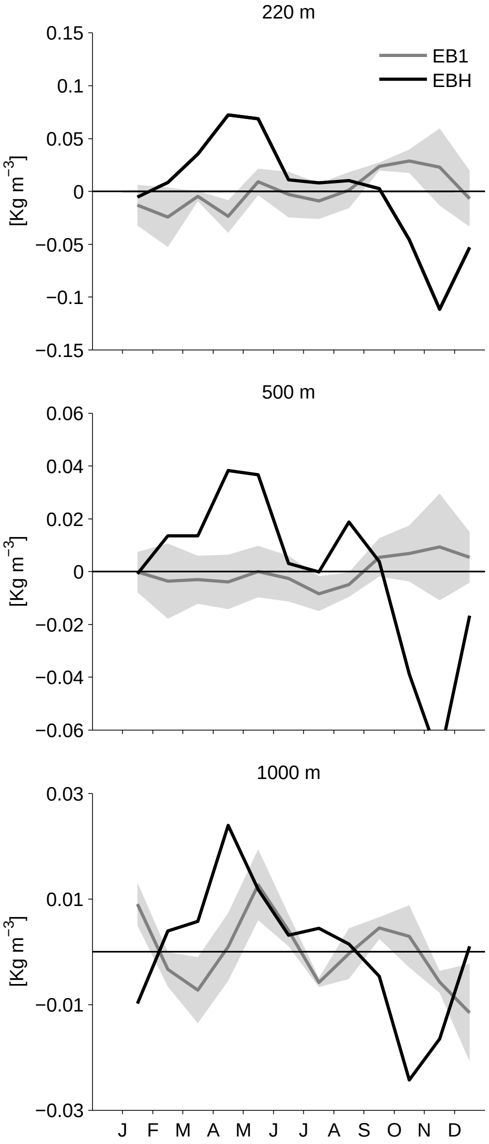

Figure 3.7: Monthly-mean in-situ density anomaly at EB1 (grey line) and EBH (black line) at selected depth levels computed for the period between April 2005 and April 2008 when both moorings have full-depth measurements. The grey envelope represent the standard error of each month at EB1. The monthly standard errors at EBH are not shown here for clarity.

One way of supressing the portion of the seasonal variations of η mainly associated with basin-scale near-surface thermal expansion is to remove at each time step the zonal mean for the whole Atlantic basin (from Bahamas to Morocco) at a given latitude. The correlation between DH at 220 m at EB1 and η with the zonal mean removed at the same location is of 0.73 (significant at 95% confidence), thus much larger than between DH at 220 m and η (without removing the zonal mean) at EB1 (0.32) (Figure 3.8). In contrast, the correlation between DH at 120 m at EBH and η with the zonal mean removed at the same location amounts to only 0.16 (insignificant at 5% error probability) (Figure 3.9). The latter indicates that almost all the correlation between DH and η at EBH is lost when attempting to isolate the variability of η at EBH by removing the basin coherent seasonal signal.

The results presented here show that there is a basin scale coherent seasonal cycle in η along 26.5° N, which has less month-to-month variability near the eastern boundary than near the western boundary. The only mooring site along the transect where the seasonal fluctuations of η and the deep vertical density structure on seasonal time scales are in phase is at EBH.

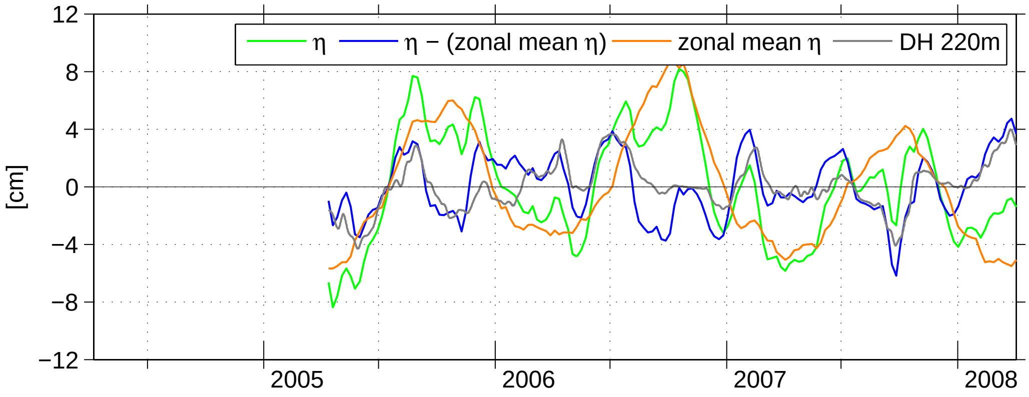

Figure 3.8: Anomalies (time average subtracted) of η at EB1 (green), η with the zonal mean (Bahamas to Morocco) at the latitude of EB1 removed (blue), zonal mean (Bahamas to Morocco) of η at the latitude of EB1 (orange), and dynamic height (DH) at 220 m at EB1 (grey).

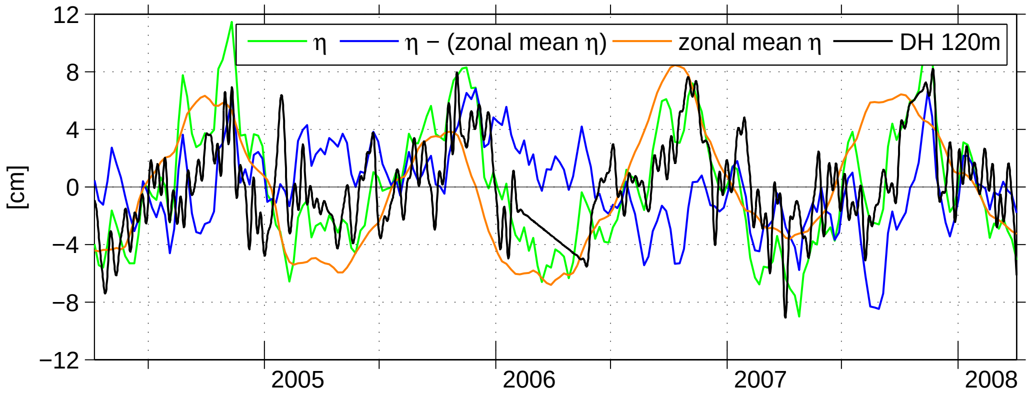

Figure 3.9: Anomalies (time average subtracted) of η at EBH (green), η with the zonal mean (Bahamas to Morocco) at the latitude of EBH removed (blue), zonal mean (Bahamas to Morocco) of η at the latitude of EBH (orange), and dynamic height (DH) at 120 m at EBH (black).

3.4 Seasonal upper ocean transports

a. Upper ocean transports between moorings

Now the seasonal variations in the upper mid-ocean transports are analyzed with the aim of establishing where along the 26.5° N transect the largest part of the seasonal upper mid-ocean transport anomaly occurs. The transports are computed as motivated in Section 3.2.2. These transports will be compared to the zonal η differences, with the purpose of testing if there is a link between the seasonal variations of the zonal η gradients and the seasonal variations in the upper mid-ocean ocean transports between moorings.

First we focus on the 10-day low-pass filtered zonally integrated upper transport fluctuations, computed from Eq. (3.2) for the segments defined by the mooring locations along 26.5° N: WB2 – WB3, WB3 – WB5, WB5 – MARW, MARW – EB1, and EB1 – EBH, namely $T^{\mathrm{UO}}_{\mathrm{WB2-WB3}}$, $T^{\mathrm{UO}}_{\mathrm{WB3-WB5}}$, $T^{\mathrm{UO}}_{\mathrm{WB5-MARW}}$, $T^{\mathrm{UO}}_{\mathrm{MARW-EB1}}$, and $T^{\mathrm{UO}}_{\mathrm{EB1-EBH}}$. The transport variability is much larger in the interior (from WB3 to MARW) than near the western (WB2 – WB3) and eastern (EB1 – EBH) boundaries (Figure 3.10). The largest transports are found between WB3 and WB5, which appear to be compensated by transport fluctuations between WB5 and MARW (suggestive of eddies and not of seasonal flow). The smallest transport variability is found as expected in the approximately 1250 km-wide segment near the eastern boundary, between EB1 and EBH.

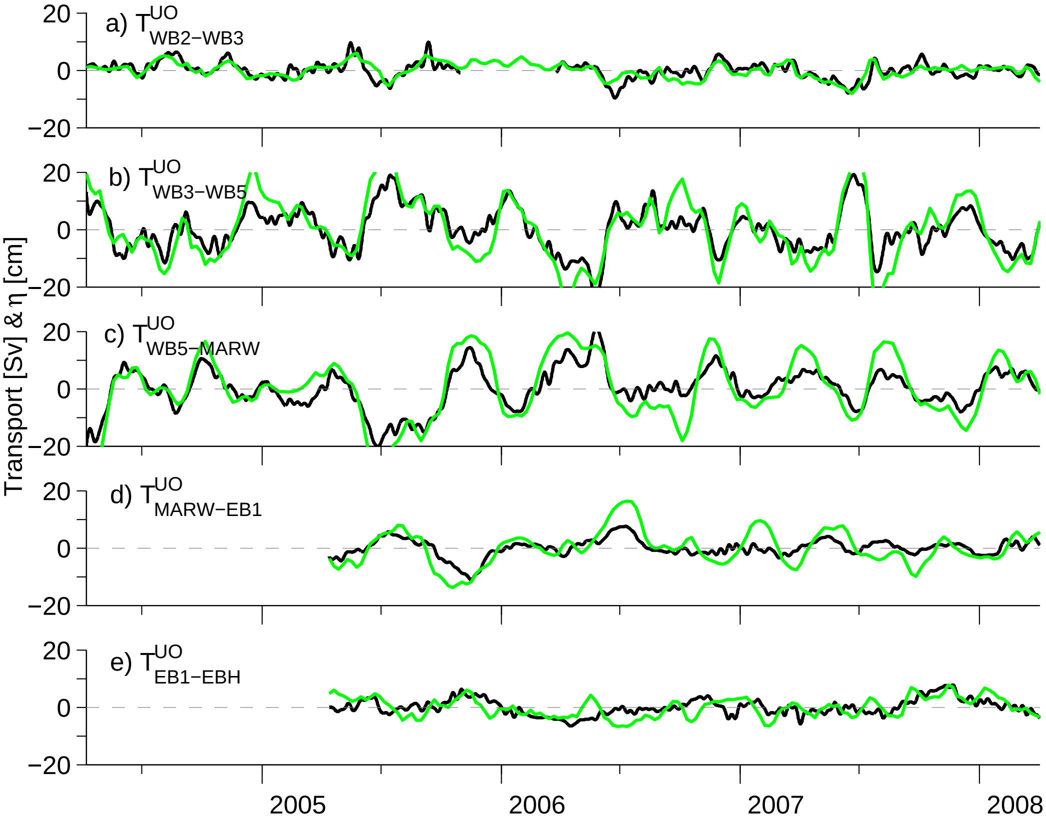

Figure 3.10: 10-day low pass-filtered upper ocean transport anomalies [Sv] above 1080 m (black lines) between (a) WB2 – WB3, ($T^{\mathrm{UO}}_{\mathrm{WB2-WB3}}$), (b) WB3 – WB5 ($T^{\mathrm{UO}}_{\mathrm{WB3-WB5}}$), (c) WB5 – MARW ($T^{\mathrm{UO}}_{\mathrm{WB5-MARW}}$), (d) MARW – EB1 ($T^{\mathrm{UO}}_{\mathrm{MARW-EB1}}$), and (e) EB1 – EBH ($T^{\mathrm{UO}}_{\mathrm{EB1-EBH}}$). The green lines represent anomalies of the zonal η differences [cm] $\eta_{WB3-WB2}$, $\eta_{WB5-WB3}$, $\eta_{MARW-WB5}$, $\eta_{EB1-MARW}$, and $\eta_{EBH-EB1}$, respectively. Positive transports correspond to northward flow.

Visual inspection of the transport time series reveals that the dynamic height at EBH (black line in Figure 3.2) contributes more to the variability near the eastern boundary than does EB1 (grey line in Figure 3.2). The seasonal cycles of these transports and the corresponding zonal differences in η, $\eta_{WB3-WB2}$, $\eta_{WB5-WB3}$, $\eta_{MARW-WB5}$, $\eta_{EB1-MARW}$, and $\eta_{EBH-EB1}$, respectively are shown in (Figure 3.11). The only segment along 26.5° N where there is a well defined seasonal cycle is within the eastern-boundary, as the monthly means of $T^{\mathrm{UO}}_{EB1-EBH}$ show, which has an amplitude of 7.6 Sv and minima in April and maxima in November and is significant above the mean standard error of ±0.8 Sv. In contrast, the seasonal cycle in $\eta_{EBH-EB1}$ does not exhibit a clear seasonality (Figure 3.11e). The latter is somehow expected as the seasonal cycles in η at EB1 and EBH are very similar (Figure 3.5).

How do the different segments along 26.5° N add up to the total basinwide integrated transport between WB2 and EBH ($T^{\mathrm{UO}}_{\mathrm{WB2-EBH}}$)?. To answer this question, $T^{\mathrm{UO}}_{\mathrm{WB2-EBH}}$ is compared to the zonally integrated upper transport fluctuations computed from Eq. (3.2) east of WB3, east of WB5, east of MARW, and east of EB1, namely $T^{\mathrm{UO}}_{\mathrm{WB3-EBH}}$, $T^{\mathrm{UO}}_{\mathrm{WB5-EBH}}$, $T^{\mathrm{UO}}_{\mathrm{MARW-EBH}}$, and $T^{\mathrm{UO}}_{\mathrm{EB1-EBH}}$. $T^{\mathrm{UO}}_{\mathrm{WB2-EBH}}$, $T^{\mathrm{UO}}_{\mathrm{WB3-EBH}}$, $T^{\mathrm{UO}}_{\mathrm{WB5-EBH}}$, $T^{\mathrm{UO}}_{\mathrm{MARW-EBH}}$, and $T^{\mathrm{UO}}_{\mathrm{EB1-EBH}}$ display a significant positive correlation (at the 95% confidence level) with the corresponding differences in η, $\eta_{EBH-WB2}$, $\eta_{EBH-WB3}$, $\eta_{EBH-WB5}$, $\eta_{EBH-MARW}$, and $\eta_{EBH-EB1}$, respectively (Figure 3.12; Table 3.2). The seasonal cycle of $T^{\mathrm{UO}}_{WB2-EBH}$ displays the minima in April and maxima in November, with a peak-to-peak amplitude of 8.9 Sv, with both peaks statistically different above the mean monthly standard error of ±1.0 Sv. The seasonal cycle of $\eta_{EBH-WB2}$ does not bring out a clear seasonality (Figure 3.13a). The seasonal cycles of $T^{\mathrm{UO}}_{WB3-EBH}$, $T^{\mathrm{UO}}_{WB5-EBH}$, and $T^{\mathrm{UO}}_{MARW-EBH}$ do not bring out a clear seasonality (Figure 3.13b-d).

We have shown in the previous chapter that eastern boundary densities contribute 5.2 Sv to the seasonal anomalies of the AMOC. Thus if the expected source of seasonal variability in $T^{\mathrm{UO}}_{WB2-EBH}$ are eastern boundary densities, the amplitude peak-to-peak of 8.9 Sv could be suggestive of a contribution of 3.7 Sv from seasonal densities at the western boundary. This can be tested isolating the contribution of western boundary densities to $T^{\mathrm{UO}}_{\mathrm{WB2-EBH}}$. For this, 4-year-average density profiles $\overline{\rho}_{EBH}(\mathrm{z})$ are used in Eq. (3.1) instead of time-variable ones, such that the only time-variable contribution comes from $\rho_{WB2}(\mathrm{z})$. Then the transports above 1080 m are computed following Eq. (3.2). The resulting contribution from western boundary densities to the seasonal transport anomalies between WB2 and EBH ($T^{\mathrm{UO}}_{\mathrm{WB2-\overline{EBH}}}$) is a random contribution resulting from the monthly averaging, while the contribution from eastern boundary densities to the upper mid-ocean transports, Ψ^{EBH}_{MAX} (Chapter 2, Section 2.5), has a pronounced well defined seasonal cycle (Figure 3.14). In addition, the phase changes are also larger at the eastern boundary. Thereby confirming that the seasonal variability in the basinwide upper mid ocean transport comes from the eastern boundary of the mid ocean section.

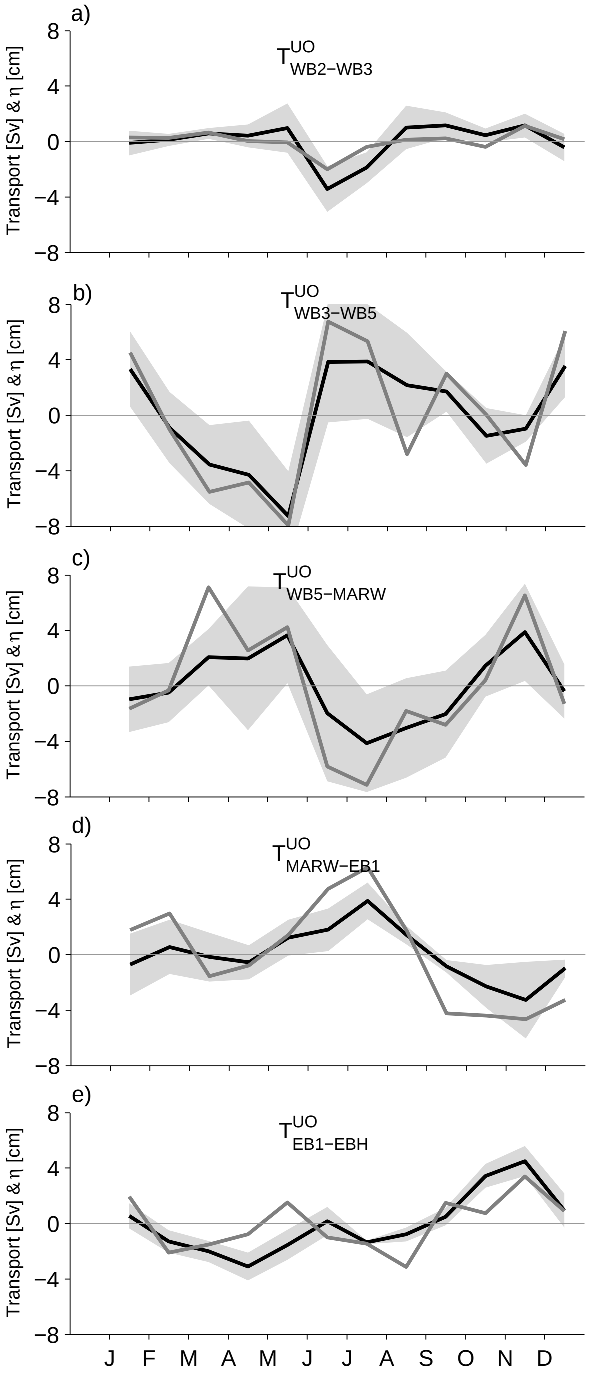

Figure 3.11: Monthly-mean anomalies of upper ocean transport anomalies [Sv] above 1080 m (black lines) between (a) WB2 – WB3, ($T^{\mathrm{UO}}_{\mathrm{WB2-WB3}}$), (b) WB3 – WB5 ($T^{\mathrm{UO}}_{\mathrm{WB3-WB5}}$), (c) WB5 – MARW ($T^{\mathrm{UO}}_{\mathrm{WB5-MARW}}$), (d) MARW – EB1 ($T^{\mathrm{UO}}_{\mathrm{MARW-EB1}}$), and (e) EB1 – EBH ($T^{\mathrm{UO}}_{\mathrm{EB1-EBH}}$). They grey envelopes represent the standard error of each month. The grey lines represent the monthly-mean anomalies of the zonal η differences [cm] $\eta_{WB3-WB2}$, $\eta_{WB5-WB3}$, $\eta_{MARW-WB5}$, $\eta_{EB1-MARW}$, and $\eta_{EBH-EB1}$, respectively. Positive transports correspond to northward flow.

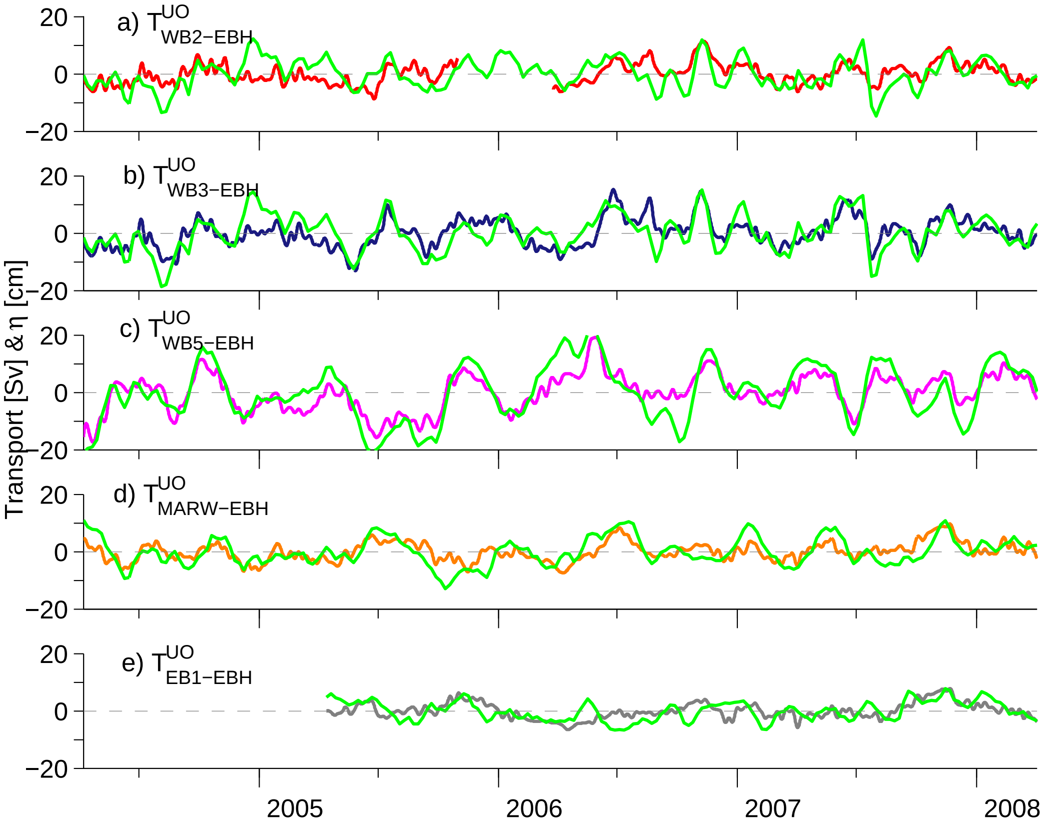

Figure 3.12: 10-day low pass-filtered upper ocean transport anomalies [Sv] above 1080 m (a) east of WB2, ($T^{\mathrm{UO}}_{\mathrm{WB2-EBH}}$, red), (b) east of WB3 ($T^{\mathrm{UO}}_{\mathrm{WB3-EBH}}$, blue), (c) east of WB5 ($T^{\mathrm{UO}}_{\mathrm{WB5-EBH}}$, magenta), (d) east of MARW ($T^{\mathrm{UO}}_{\mathrm{MARW-EBH}}$, orange), and (e) east of EB1 ($T^{\mathrm{UO}}_{\mathrm{EB1-EBH}}$, grey). The green lines represent fluctuations of the zonal η differences [cm] $\eta_{EBH-WB2}$, $\eta_{EBH-WB3}$, $\eta_{EBH-WB5}$, $\eta_{EBH-MARW}$, and $\eta_{EBH-EB1}$, respectively. Positive transports correspond to northward flow.

Site W	Site E	$T^{\mathrm{UO}}_{\mathrm{site\ W-site\ E}}$ std dev [Sv]	correlation ($T^{\mathrm{UO}}_{\mathrm{site\ W-site\ E}}$ and $\eta_{siteE-siteW}$)
WB2	EBH	4.0	0.43
WB3	EBH	4.8	0.64
WB5	EBH	6.9	0.83
MARW	EBH	4.0	0.66
EB1	EBH	2.6	0.54

Table 3.2: Column 3 show the standard deviation of the 10-day low-pass filtered upper ocean transports computed following Eq. (3.2) between the mooring sites given in columns 1 and 2. Column 4 displays the the correlations of transports with the zonal η difference between the moorings. All the time series span the period April 2004 to April 2008 except for calculations concerning EB1 (April 2005 to April 2008).

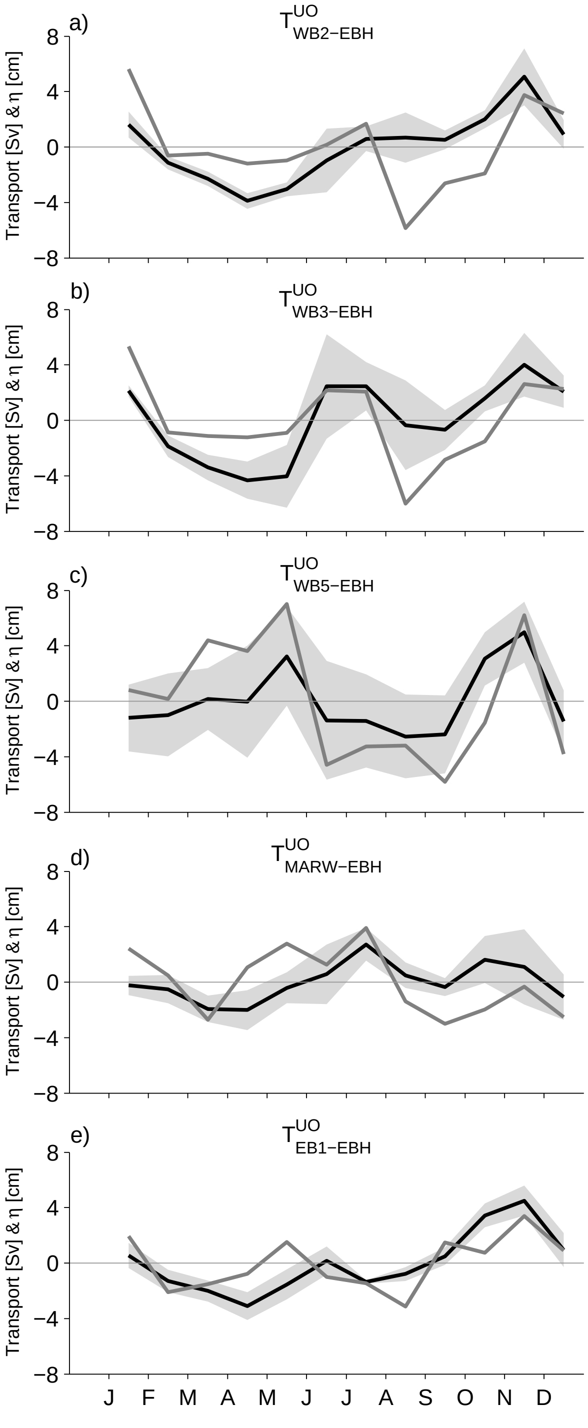

Figure 3.13: Monthly means anomalies of 10-day low pass filtered upper ocean transport [Sv] above 1080 m (black lines) (a) east of WB2, ($T^{\mathrm{UO}}_{\mathrm{WB2-EBH}}$), (b) east of WB3 ($T^{\mathrm{UO}}_{\mathrm{WB3-EBH}}$), (c) east of WB5 ($T^{\mathrm{UO}}_{\mathrm{WB5-EBH}}$), (d) east of MARW ($T^{\mathrm{UO}}_{\mathrm{MARW-EBH}}$), and (e) east of EB1 ($T^{\mathrm{UO}}_{\mathrm{EB1-EBH}}$). They grey envelopes represent the standard error of each month. The grey lines represent the monthly mean fluctuations of the zonal η differences [cm] $\eta_{EBH-WB2}$, $\eta_{EBH-WB3}$, $\eta_{EBH-WB5}$, $\eta_{EBH-MARW}$, and $\eta_{EBH-EB1}$, respectively.

Thus, the seasonal transport signal is confined to the eastern boundary and has an imprint on the upper ocean transport variability along 26.5° N only when computing the upper transports from the western to the eastern endpoints of the basin (Figure 3.13a). A similar analysis but computing upper ocean transports accumulated from the western boundary towards the east (west of WB3, west of WB5, west of MARW, west of EB1, and west of EBH) shows that the only segment of the transatlantic section that displays a clear seasonal cycle in upper mid-ocean transports is between WB2 and EBH (not shown).

The monthly means of $\eta_{EBH-WB2}$ and $\eta_{EBH-EB1}$, instead, do not bring out a clear seasonality and they have little correspondence to the seasonal upper ocean transport seasonal cycles as observed with $T^{\mathrm{UO}}_{WB2-EBH}$ and $T^{\mathrm{UO}}_{EB1-EBH}$, respectively (Figure 3.13a-e). These results indicate that fluctuations of η along 26.5° N are not good indicators of the seasonal anomalies in upper ocean transports at 26.5° N.

b. Eastern-boundary transport contribution to the AMOC

Now the connection between the transport contribution to the AMOC arising from eastern boundary density variability, Ψ^{EBH}_{MAX}, and η at EBH is analyzed. We estimated the integral time scales in the time series of Ψ^{EBH}_{MAX} to be 22 days. That means that for the 42-month time series there are 62 degrees of freedom. Thus, correlations grater than 0.32 are significantly different from zero at a 95% confidence level. Between the two variables there is a significant correlation at the 95% confidence level of 0.63.

A linear regression of the form $\Psi^{EBH}_{MAX} = m * \eta_{EBH}$ gives m = 0.31 Sv cm^{-1} (Figure 3.15). Subtracting the fit from Ψ^{EBH}_{MAX} yields transport residuals Ψ^{EBH}_{MAX} – m * η_{EBH} of 1.5 Sv rms. The linear fit using η_{EBH} explains 53% of the variance of Ψ^{EBH}_{MAX}. The error of the transport prediction using η (1.5 Sv rms) has a quite large amplitude given that the rms variability of Ψ^{EBH}_{MAX} is 2 Sv rms, indicating that the uncertainties are quite large when trying to predict Ψ^{EBH}_{MAX} with η. On seasonal timescales (180-day low pass filtered anomalies), the correlation between Ψ^{EBH}_{MAX} and η at EBH increases substantially to 0.91 (significant at the 95% confidence limit)(Figure 3.16a), while on intra-seasonal timescales (less than 100 days) they are significatively correlated (correlation coefficient of 0.45) at the 95% level only for a narrow period band between 70 and 100 days. The spectra of Ψ^{EBH}_{MAX} does not exhibit significant peaks at the 70 – 100 days period band (Chapter 2, Section 2.5), hence it does not represent an important period band in terms of transport variability arising from eastern boundary density changes. A large part of the correlation between the two variables seems to come from the period from October 2007 and April 2008 (Figure 3.16b). The correlation between the two variables 70 – 100 days band pass filtered without considering the period from October 2007 and April 2008 amounts to only 0.32.

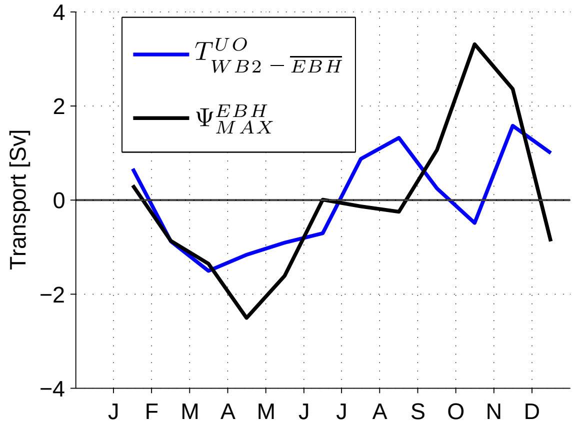

Figure 3.14: Monthly-mean anomalies of 10-day low pass filtered upper ocean transport above 1080 m east of WB2 assuming steady eastern-boundary conditions ($T^{\mathrm{UO}}_{\mathrm{WB2-\overline{EBH}}}$, blue), and 10-day low-pass filtered anomalies of the eastern boundary contribution to the AMOC at 26.5° N (Ψ^{EBH}_{MAX}, black).

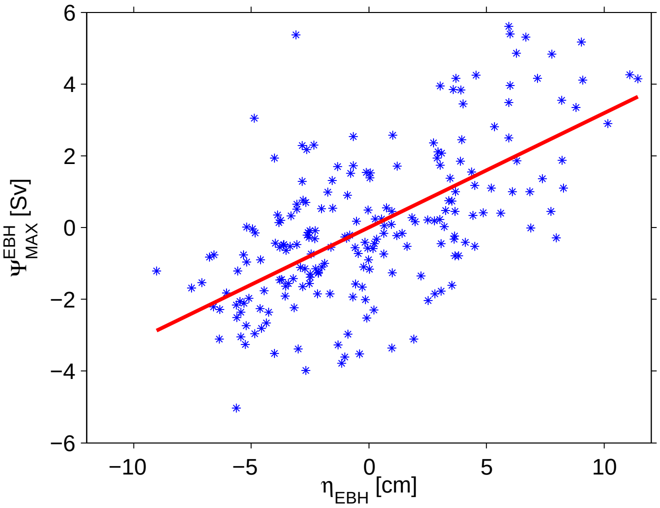

Figure 3.15: Scatter plot between 10-day low-pass filtered anomalies of the eastern boundary contribution to the AMOC at 26.5° N (Ψ^{EBH}_{MAX}) and the anomalies of η at EBH for the period between April 2004 and April 2008. The red line represents the fitted least-squares linear regression. The resulting coefficient and slope are 0.63 and 0.31 respectively.

The seasonal cycles of Ψ^{EBH}_{MAX} and η at EBH are in good agreement (Figure 3.17) both exhibit minima in spring (May) and maxima in autumn even though the latter is shifted by one month (October for Ψ^{EBH}_{MAX} and November for η). The long-term seasonal cycle of η indicates that the autumn maximum in November is representative of much longer periods.

These results indicate that even though there is good agreement between Ψ^{EBH}_{MAX} and η on seasonal and longer timescales, the uncertainties are quite large when trying to predict Ψ^{EBH}_{MAX} with η by means of a linear regression.

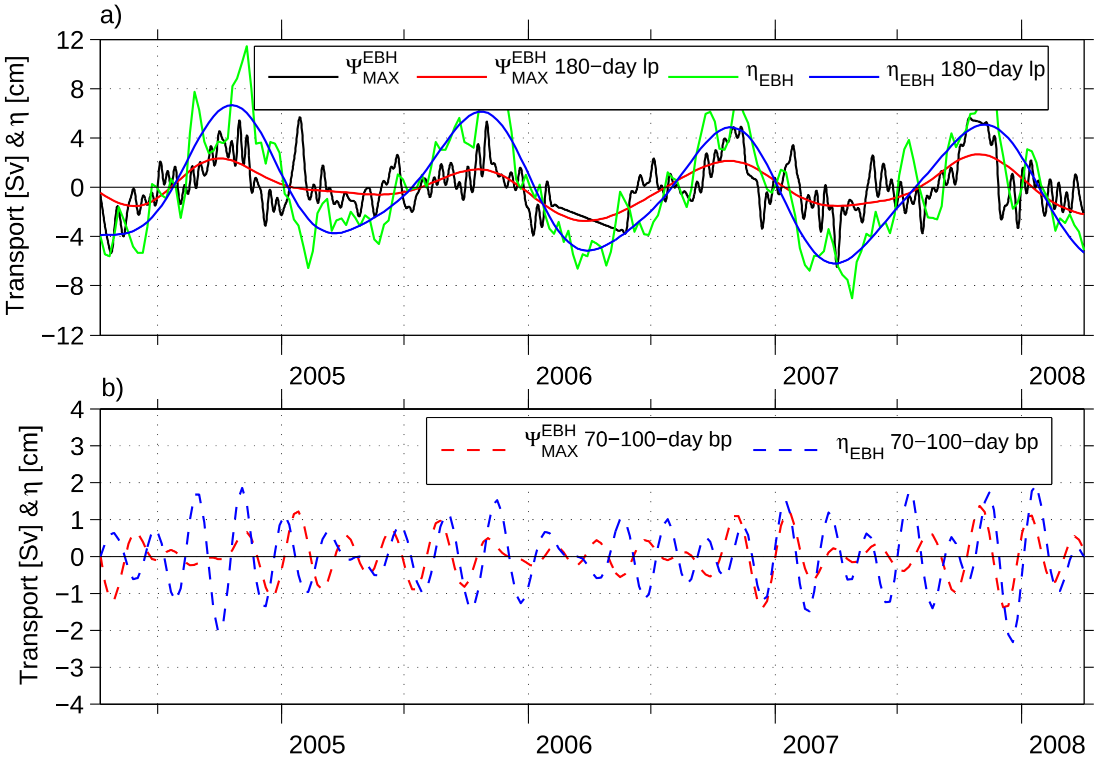

Figure 3.16: (a) 10-day low-pass filtered anomalies of the eastern boundary contribution to the AMOC at 26.5° N [Sv] (Ψ^{EBH}_{MAX}, black), 180-day low-pass filtered anomalies of Ψ^{EBH}_{MAX} [Sv] (red), anomalies of η at EBH [cm] (green), and 180-day low-pass filtered anomalies of η at EBH [cm] (blue), and (b) 70 – 100-day band-pass filtered anomalies of Ψ^{EBH}_{MAX} [Sv] (dashed red), 70 – 100-day band-pass filtered anomalies of η at EBH [cm] (dashed blue).

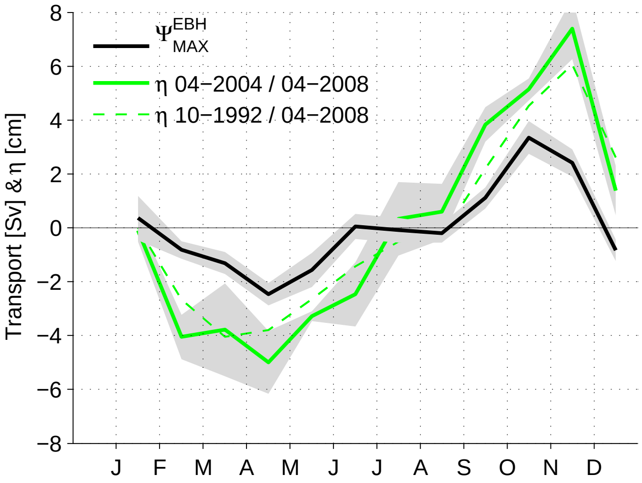

Figure 3.17: Monthly-means of 10-day low-pass filtered anomalies of the eastern boundary contribution to the AMOC at 26.5° N [Sv] (Ψ^{EBH}_{MAX}, black), monthly-mean anomalies of η at EBH [cm] computed for the period between April 2004 and April 2008 (solid green line), and monthly-mean anomalies of η at EBH [cm] computed based on the 15-year long record (dashed green line). The grey envelopes represent the standard error of each month.

3.5 Discussion

Cheney et al. (1994) showed that the uncertainty in monthly values of sea surface height (η) is approximately within 2.0 cm rms. An error analysis of geopotential anomalies performed by Johns et al. (2005) showed that total rms error of geopotential anomalies computed from in situ temperature measurements does not exceed $0.2\,\mathrm{m^2s^{-2}}$ rms. They used a lower vertical density sampling levels than in this study, few pressure measurements, and no conductivity measurements. Thus, we estimate that the errors in geopotential anomalies in this study are less than $0.2\,\mathrm{m^2s^{-2}}$. Kanzow et al. (2010) estimated the error in 10-day low pass filtered measurements of top-to-bottom integrated internal transports to be less than 2.0 Sv. The geopotential anomalies, the transport anomalies, and η anomalies discussed in this study thus exceed the error bars.

We have shown that the seasonal cycles in η from altimetry are in phase along the 26.5° N transect with a maximum in the autumn and a minimum in the first half of the year. However, at the western basin the seasonal cycles of η exhibit much larger standard errors compared to the seasonal cycles at the eastern boundary. This points to different dynamics governing the variability of η near the western boundary and the eastern boundary of the mid ocean section. In particular, offshore of the western boundary large eddy variability is found. The seasonal cycles of η with less month-to-month variability are found at the locations of the two easternmost moorings, EB1 and EBH. Vinogradov et al. (2008) found that in the subtropical oceans the depth to which it is sufficient to integrate the steric height signals in order to explain 80% of the total (top to bottom) seasonal steric height variability is about 100 m. In agreement, we find that the dynamic heights derived from the RAPID/MOCHA in-situ density measurements at WB2, WB3, WB5, MARW, and EB1 do not show significant seasonal anomalies at depths below than 200 m. At EBH, however, moored in-situ density measurements show a coherent deep-reaching seasonal cycle in densities between 100 and 1400 m (Chidichimo et al. 2010). The following picture emerges near the eastern boundary. The seasonal cycle in η at EB1 is confined to a very thin layer in the upper ocean as there is no evidence of significant seasonal density anomalies below 200 m, while at EBH the seasonal isopycnal displacements are observed up to 1400 m, and most likely the deep seasonal cycle is associated with the strong near-coastal seasonal cycle in wind stress curl that lifts and depresses the density surfaces leading to maximum density during spring and minimum density during autumn (Chidichimo et al. 2010). The fact that we can establish a link between η and the seasonal deep vertical structure at EBH might be fortuitous, in the sense that it arises because the deep seasonal density anomalies are in phase with the seasonal changes in density near the surface. One way of suppressing the large steric cycle in the upper ocean is to remove the zonal mean of the whole Atlantic basin from η. When attempting to isolate the variability of η at EBH by removing the basin coherent seasonal signal, almost all the correlation between DH and η at EBH is lost. These results indicate that the observations of η on seasonal timescales are difficult to reconcile with the deep seasonal density variability observed at EBH.

Our analysis of the seasonal circulation across 26.5° N shows that the transport anomalies which dominate the seasonal cycle of the basinwide upper ocean transports with autumn maximum and spring minimum do not correspond to basin scale coherent flows but are concentrated at the eastern boundary between EB1 and EBH. As the deep seasonal anomalies at EBH (and the lack thereof at EB1) suggest, the seasonal flow takes place near the African coast rather than being broadly distributed over the more than 1000 km wide section between EB1 and EBH. Baringer and Molinari (1999) concluded that more than 90% of the annual cycle in baroclinic heat flux (BHF) across 26° N in the Atlantic (caused by the interior transport shear profile) is captured within 3000 km of the western boundary of the mid-ocean section. These results are difficult to reconcile with the mooring observations. In addition, the phase of the seasonal cycle in BHF found by Baringer and Molinari (1999) (summer maximum) is quite different to what we find (spring minimum and fall maximum). To carry out a straightforward comparison with the study of Baringer and Molinari (1999), the BHF should be computed from the RAPID/MOCHA mooring measurements. The focus of this study lies in AMOC-related transport variability, hence the detailed analysis of heat transport and its components is outside of the scope of this thesis. Results from Johns et al. (2010) (manuscript in prep.) suggest the fluctuations in the strength of the AMOC and the northward heat transport across 26.5° N are highly correlated (better than 0.9). One might speculate that the large difference between the study of Baringer and Molinari (1999) and this study could be due to the different temporal and spatial resolution of the data sets used for the analysis (hydrographic sections combined with climatologies versus continuous moored-based density measurements). In particular, the largest differences may be due to the lack of sufficient density measurements close to the eastern boundary at 26° N in Baringer and Molinari (1999) study to resolve the seasonal cycle there.

The zonal differences in η between WB2 and EBH and between EB1 and EBH can not recover the seasonal signal of the corresponding upper ocean transports. The fact that there is not a seasonal signal in the zonal differences in η between EB1 and EBH arises because seasonal amplitude of η at EB1 and EBH is very similar. This could indicate that the seasonal heat fluxes have larger seasonal amplitudes offshore (EB1) than inshore (EBH). A detailed analysis of the heat budget in the eastern boundary of the Atlantic would shed more light into this issue. There is good agreement between Ψ_{MAX}^{EBH} and η on seasonal and longer timescales. However, the uncertainties are quite large when trying to predict Ψ_{MAX}^{EBH} with η by means of a linear regression. The results presented here imply that the seasonal variations in η can not be used to estimate seasonal upper ocean transports at 26.5° N.

3.6 Conclusions

Based on an array of moorings distributed along 26.5° N in the western basin (WB2, WB3, WB5, and MARW) and the eastern basin (EB1 and EBH) of the Atlantic, and a 15-year long record of altimetric observations of sea surface height (η) interpolated onto the mooring positions, we conclude:

- There is a basin scale coherent seasonal cycle in η along 26.5° N, which has less month-to-month variability near the eastern boundary than near the western boundary. The only mooring site along the transect where the fluctuations of η and the deep vertical density structure on seasonal time scales are in phase is at EBH.
- At EB1 no significant seasonal density anomalies below 100 m are found while at EBH there are coherent seasonal density anomalies between 100 – 1400 m.
- Along 26.5° N the dynamically relevant signal below 100 m in density on seasonal

timescales, which leads to the stronger southward upper ocean flow in spring that in turn causes the minimum in the AMOC at that time, and viceversa in autumn, is confined to the eastern boundary between EB1 and EBH. This implies that the seasonal flow is not associated with the large scale forcing pattern, but it is associated with localized forcing, such as wind stress forcing or boundary wave propagation.

- When attempting to remove the basin scale coherent seasonal signal from η to isolate the variability at EBH there is no significant correlation between η and the dynamic height computed from moored density measurements at EBH.
- The gradient of the seasonal surface elevations inferred from altimetry can not be related to seasonal upper mid ocean transport variability at 26.5° N.
- The results presented here indicate that it is essential to observe the deep vertical density structure at the eastern boundary of the mid-ocean section as part of an AMOC monitoring strategy.

Chapter 4

Conclusions and outlook

4.1 Conclusions

We conclude this thesis, providing answers to the questions posed in the introduction (Chapter 1).

(1) Is the eastern-boundary density variability an important contributor to sub-seasonal and seasonal anomalies of the strength and vertical structure of the AMOC at 26.5° N?

Yes. The 10-day low-pass filtered 42-month long record of the eastern boundary contribution to the AMOC at 26.5° N, $\Psi^{\mathrm{EBH}}_{\mathrm{MAX}}$, has a temporal standard deviation of ±2 Sv. Kanzow et al. (2010) show that the overall AMOC variability is ±4.9 Sv and that the western boundary contribution of the mid-ocean section to the AMOC varies by ±2.3 Sv. The latter indicates that the western and eastern boundaries of the mid-ocean section contribute to the AMOC variability by roughly the same amount. This result contradicts earlier findings by Longworth (2007), who found from historical CTD measurements that the eastern boundary contribution was only half of that from the western boundary. However, the *total* western-boundary transport contribution to the AMOC also includes variability of the Gulf Stream and is hence significantly larger than that from the eastern boundary. We find a pronounced deep-reaching seasonal cycle in eastern-boundary density, with maximum positive density anomalies in spring and negative ones in autumn, which are coherent between 100 m and 1400 m. These anomalies drive anomalous southward upper mid-ocean flow in spring, implying maximum reduction of the AMOC, and anomalous northward upper mid-ocean flow in autumn, implying maximum strengthening of the AMOC. The eastern boundary causes a peak-to-peak seasonal cycle of the AMOC of 5.2 Sv, which clearly dominates the peak-to-peak seasonal cycle of the *total* AMOC of 6.7 Sv. This dominant influence is surprising and arises because western boundary transports do not display such a clear seasonal cycle when isolated in a similar fashion.

(2) Are the density anomalies coherent at EB1 and EBH such that EB1 might serve as backup or replacement of EBH, as was formulated in the original proposal (Marotzke et al. 2002)?

No. The results presented here show that there is little agreement between the transports estimates from EB1 and EBH. There are considerable differences between EB1 and EBH in terms of temporal variability, amplitude, vertical structure and frequency distribution of the resulting mid-ocean geostrophic transport fluctuations. The transports derived from EB1 show much less energy at periods shorter than 50 days, compared to the transports derived from EBH. The leading EOF transport modes show that the vertical shear of the transport arising from EB1 and EBH is especially different in the upper 1000 m. This points to different dynamics governing the density fluctuations at EB1 and EBH. Local coastal wind forcing appears to play an important role in setting the variability at EBH. At EB1, the deep-reaching density anomalies may be linked to mesoscale eddies associated with the open ocean circulation. Contrary to the original planning (Marotzke et al. 2002), measurements at EB1 and EBH cannot serve as a backup for each other: densities need to be measured right at the continental slope to compute the full-basin density gradient as part of an AMOC monitoring strategy.

(3) Which are the possible driving mechanisms of eastern-boundary density variability on seasonal timescales?

Several authors reported seasonal anomalies of the eastern boundary current system off Northwest Africa based on mooring-based measurements and hydrographic observations. A strong northward current during autumn close to the African shelf in the 1300 m deep channel between Lanzarote and Africa at 29° N was observed (Knoll et al. 2002; Hernández-Guerra et al. 2003). Knoll et al. (2002) found maximum southward flow in the upper 200 m in the middle of the channel between Lanzarote and Africa during spring. The seasonal northward transport in the Canary Current system is consistent with the anomalous northward transports (and minimum in in-situ density) we find in October. The phase of maximum southward flow during spring reported by Knoll et al. (2002) is consistent with the southward transports (and maximum in in-situ density) we find in April. This suggests a link with the variability we find in $\Psi^{\mathrm{EBH}}_{\mathrm{MAX}}$ but further analysis needs to be done on the variability of the eastern boundary current. The Moroccan coastal upwelling undergoes seasonal changes induced by the coast-parallel trade winds. The band between 25° N and 43° N along the African coast exhibits strongest coastal upwelling during summer and autumn (e.g., Wooster et al. 1976; Mittelstaedt 1983). We observe maximum densities in April/May, two months earlier than the maximum upwelling occurs. Also coastal upwelling is thought to bring waters from 200 or 300 m depth to the surface. In contrast, our analysis suggests coherent seasonal density changes down to 1400 m. For these reasons coastal upwelling is unlikely to be the direct driver of the seasonal density and transport cycles. Instead, the vertical structure suggests a first baroclinic mode as a result of the displacement of the density surfaces induced by the wind stress curl. An analysis of the QuikSCAT-based SCOW (Scatterometer Climatology of Ocean Winds) seasonal wind stress curl climatology (Risien and Chelton 2008) reveals a pronounced seasonal cycle in eastern boundary wind stress curl, which leads the density anomaly by roughly 90 degrees or 3 months. The out-of-phase relationship is plausible, as uplifting of the density surfaces should prevail during the winter phases of enhanced cyclonic wind curl anomalies. Therefore maximum positive density anomalies can be expected in spring, when the transition from cyclonic to anti-cyclonic wind stress curl anomalies takes place. The summer period of anti-cyclonic wind stress curl then should lead to the observed maximum negative density anomalies in autumn as a result of the maximum depression of the density surfaces.

(4) Do the seasonal transport anomalies correspond to broad (basin scale) or localized (e.g. near ocean boundary) flows?

The analysis of the seasonal circulation across 26.5° N shows that the transport anomalies which dominate the seasonal cycle of the basinwide upper ocean transports with autumn maximum and spring minimum do not correspond to basin scale coherent flows but are concentrated at the eastern boundary between EB1 and EBH. As the deep seasonal anomalies at EBH (and the lack thereof at EB1) suggest, the seasonal flow takes place near the African coast rather than being broadly distributed over the more than 1000 km wide section between EB1 and EBH. This implies that the seasonal flow is not associated with the large scale forcing pattern, but it is associated with localized forcing, such as wind stress forcing or boundary wave propagation.

(5) Is altimetry a useful tool to infer seasonal upper mid-ocean transports at 26.5° N?

The results presented here show that there is a basin scale coherent seasonal cycle in η along 26.5° N, which has less month-to-month variability near the eastern boundary than near the western boundary. The only mooring site along the transect where the fluctuations of η and the deep vertical density structure on seasonal time scales are in phase is at EBH. When attempting to remove the basin scale coherent seasonal signal from η to isolate the variability at EBH there is no significant correlation between η and the dynamic height computed from moored density measurements at EBH. The zonal differences in η can not recover the seasonal transport signal present in the upper ocean transports computed from the moorings between WB2 and EBH and between EB1 and EBH. Our results imply that the seasonal surface elevations inferred from altimetry can not be related to seasonal upper mid ocean transport variability at 26.5° N.

4.2 Outlook

It would be beneficial to observe whether the pronounced seasonal variability at the eastern boundary is associated with localized variability or to a large meridional scale (of O(1000 km)). This question becomes relevant in the climate context, as a large meridional scale of the seasonal anomalies found at the eastern boundary could imply a large meridional extent of the seasonal upper mid ocean transports and the associated heat flux. Ideally, to quantify the extent of the meridional coherence of the measurements at the eastern boundary at 26.5° N one would need to analyze continuous deep top-to-bottom density measurements along the eastern boundary of the Atlantic. In reality, this is not plausible given the lack of such observations. We have shown that the observations of sea surface height on seasonal time scales are difficult to reconcile with the pronounced deep vertical seasonal density structure at the eastern boundary. An alternative way of studying the meridional scale of the eastern boundary densities would be using a numerical model that could provide deep density measurements along the eastern boundary of the Atlantic. However, this could only be successful if the model was able to recover the deep density structure observed with the RAPID/MOCHA moorings. Bingham et al. (2007) studied the meridional coherence of the AMOC in a range of ocean models. They found that there are substantial changes in the character of the AMOC south and north of 40° N. South of 40° N they found meridionally coherent AMOC variability on interannual timescales, while north of 40° N there is a strong decadal component in AMOC variability. Thus, judging from their results it would be efficient to place a mooring near the eastern boundary south of 40° N, but far away enough from EBH so that a large meridional scale (of O(1000 km)) could be studied.

4.3 Résumé

We present the first 4-year-long time series of the contribution of the eastern-boundary density variability to AMOC fluctuations at 26.5° N, based on sustained continuous moored density measurements from the RAPID/MOCHA array between April 2004 and April 2008. The contribution of eastern-boundary density variations to the AMOC is larger than expected. Eastern-boundary density variations contribute ±2 Sv rms AMOC variability, similar to the contribution from the western boundary (east of the Bahamas) to the mid-ocean geostrophic component of the AMOC. The seasonal cycle in density at the eastern boundary is coherent between 100 m and 1400 m, with maximum positive and negative density anomalies in spring and autumn, respectively. Resulting is a minimum AMOC in spring and a maximum AMOC in autumn, with a peak-to-peak amplitude of the seasonal cycle of 5.2 Sv caused by the eastern boundary, which dominates the 6.7 Sv seasonal cycle of the *total* AMOC. The results presented here indicate that it is essential to observe the deep vertical density structure at the eastern boundary of the Atlantic as part of an AMOC monitoring strategy at 26.5° N.

Bibliography

Baringer, M. O. and Larsen, J. C.: Sixteen years of Florida Current Transport at 27° N, Geophysical Research Letters, 28, 3179–3182, 2001.

Baringer, M. O. and Molinari, R.: Atlantic Ocean baroclinic heat flux at 24 to 26° N, Geophysical Research Letters, 26, 353–356, 1999.

Baringer, M. O., Johns, W. E., Meinen, C. S., Shoosmith, D., and Bryden, H. L.: On the structure of Florida Current Variability, Poster presentation at the Rapid Climate Change 2008 annual meeting, online available at: `http://www.noc.soton.ac.uk/rapid/sci/viewabs1.php?keyword1=gwa806`, 2008.

Bingham, R. J. and Hughes, C. W.: Signature of the Atlantic meridional overturning circulation in sea level along the east coast of North America, Geophysical Research Letters, 36, L02 603, 2009.

Bingham, R. J., Hughes, C. W., Roussenov, V., and Williams, R. G.: Meridional coherence of the North Atlantic meridional overturning circulation, Geophysical Research Letters, 34, L23 606, 2007.

Bryden, H. L., Longworth, H. R., and Cunningham, S. A.: Slowing of the Atlantic meridional overturning circulation at 25° N, Nature, 438, 655–657, 2005.

Bryden, H. L., Mujahid, A., Cunningham, S. A., and Kanzow, T.: Adjustment of the basin-scale circulation at 26° N to variations in Gulf Stream, deep western boundary current and Ekman transports as observed by the Rapid array, Ocean Science, 5, 421–433, URL `http://www.ocean-sci.net/5/421/2009/`, 2009.

Cheney, R. E., Miller, L., Agreen, R., Doyle, N., and Lillibridge, J.: TOPEX/POSEIDON: The 2-cm solution, Journal of Geophysical Research, 99, 24 555–24 564, 1994.

Chidichimo, M. P., Kanzow, T., Cunningham, S. A., Johns, W. E., and Marotzke, J.: The contribution of eastern-boundary density variations to the Atlantic meridional overturning circulation at 26.5° N, Ocean Science, 6, 475–490, doi:10.5194/os-6-475-2010, URL `http://www.ocean-sci.net/6/475/2010/`, 2010.

Cunningham, S. A., Kanzow, T., Rayner, D., Baringer, M. O., Johns, W. E., Marotzke, J., Longworth, H. R., Grant, E. M., Hirschi, J. J.-M., Beal, L. M., Meinen, C. S., and Bryden, H. L.: Temporal variability of the Atlantic meridional overturning circulation at 26.5° N, Science, 317, 935–938, 2007.

Dibarboure, G., Lauret, O., Mertz, F., and Rosmorduc, V.: SSALTO/DUACS user handbook: (M)SLA and (M)ADT near-real time and delayed time products. CLS-DOS-NT-0.6.304,Rev. 9, Aviso User Service, Ramonville St-Agne, France, SALP-MU-P-EA-21065-CLS, Issue 1, p. 41, 2008.

Ganachaud, A. and Wunsch, C.: Large-scale ocean heat and freshwater transports during the World Ocean Circulation Experiment, Journal of Climate, 16, 696–705, 2003.

Hall, M. M. and Bryden, H. L.: Direct estimates and mechanisms of ocean heat transport, Deep Sea Research I, 3A, 339–359, 1982.

Hernández-Guerra, A., Aristegui, J., Canton, M., and Nykjaer, L.: Phytoplankton pigment patterns in the Canary Islands area as determined using Coastal Zone Colour Scanner data, International Journal of Remote Sensing, 14, 1431–1437, 1993.

Hernández-Guerra, A., Fraile-Nuez, E., Borges, R., López-Laatzen, F., Véllez-Belchi, P., Parrilla, G., T., and Müller: Transport variability in the Lanzarote passage (eastern boundary current of the North Atlantic Subtropical Gyre), Deep Sea Research I, 50, 189–200, 2003.

Hernández-Guerra, A., Fraile-Nuez, E., López-Laatzen, F., Parrilla, G., and Véllez-Belchi, P.: Canary Current and North Equatorial Current from an inverse box model, Journal of Geophysical Research, 110, C12 019, 2005.

Hirschi, J., Baehr, J., Marotzke, J., Stark, J., Cunningham, S., and Beismann, J. O.: A monitoring design for the Atlantic meridional overturning circulation, Geophysical Research Letters, 30, 1413, 2003.

Hirschi, J. J.-M. and Marotzke, J.: Reconstructing the meridional overturning circulation from boundary densities and the zonal wind stress, Journal of Physical Oceanography, 37, 743–763, 2007.

Hirschi, J. J.-M., Killworth, P. D., Blundell, J. R., and Cromwell, D.: Sea Surface height signals as indicators for oceanic meridional mass transports, Journal of Physical Oceanography, 39, 581–601, 2009.

Ivchenko, V. I., Danilov, S., Sidorenko, D., Scröter, J., Wenzel, M., and Aleynik, D. L.: Steric height variability in the Northern Atlantic on seasonal and interannual time scales, Journal of Geophysical Research, 113, C11 007, 2008.

Johns, W. E., Kanzow, T., and Zantopp, R.: Estimating ocean transports with dynamic height moorings: An application in the Atlantic deep western boundary current, Deep Sea Research I, 52, 1542–1567, 2005.

Johns, W. E., Beal, L. M., Baringer, M. O., Molina, J., Cunningham, S. A., Kanzow, T., and Rayner, D.: Variability of shallow and deep western boundary currents off the Bahamas during 2004-2005: First results from the 26° N RAPID-MOC array, Journal of Physical Oceanography, 38, 605–623, 2008.

Johns, W. E., Beal, L. M., Baringer, M. O., Cunningham, S. A., Kanzow, T., Bryden, H. L., Hirschi, J. J. M., Marotzke, J., Meinen, C. S., Shaw, B., and Curry, R.: Continuous, array-based estimates of Atlantic Ocean Heat transport at 26° N, in preparation, 2010.

Johnson, H. L. and Marshall, D. P.: Localization of abrupt change in the North Atlantic thermohaline circulation, Geophysical Research Letters, 29, 1083, 2002.

Johnson, H. L. and Marshall, D. P.: Global teleconnections of meridional overturning circulation anomalies, Journal of Physical Oceanography, 34, 1702–1722, 2004.

Kanzow, T., Send, U., Zenk, W., Chave, A. D., and Rhein, M.: Monitoring the integrated deep meridional flow in the tropical North Atlantic: Long-term performance of a geostrophic array, Deep Sea Research I, 53, 528–546, 2006.

Kanzow, T., Cunningham, S. A., Rayner, D., Hirschi, J. J.-M., Johns, W. E., Baringer, M. O., Bryden, H. L., Beal, L. M., Meinen, C. S., and Marotzke, J.: Observed flow compensation associated with the MOC at 26.5° N in the Atlantic, Science, 317, 938–941, 2007.

Kanzow, T., Hirschi, J. J. M., Meinen, C. S., Rayner, D., Cunningham, S. A., Marotzke, J., Johns, W. E., Bryden, H. L., Beal, L. M., and Baringer, M. O.: A prototype system for observing the Atlantic Meridional Overturning Circulation - scientific basis, measurement and risk mitigation strategies, and first results, Journal of Operational Oceanography, 1, 19–28, 2008a.

Kanzow, T., Send, U., and McCartney, M.: On the variability of the deep meridional transports in the tropical North Atlantic, Deep-Sea Research I, 55, 1601–1623, 2008b.

Kanzow, T., Johnson, H., Marshall, D., Cunningham, S. A., Hirschi, J. J.-M., Mujahid, A., Bryden, H. L., and Johns, W. E.: Basinwide integrated volume transports in an eddy-filled ocean, Journal of Physical Oceanography, 39, 3091–3110, 2009.

Kanzow, T., Cunningham, S. A., Johns, W. E., Hirschi, J. J.-M., Marotzke, J., Baringer, M. O., Meinen, C. S., Chidichimo, M. P., Atkinson, C., Beal, L. M., Bryden, H. L., and Collins, J.: Seasonal variability of the Atlantic meridional overturning circulation at 26.5° N, Journal of Climate, in review, 2010.

Kawase, M.: Establishment of mass-driven abyssal circulation , Journal of Physical Oceanography, 17, 2294–2317, 1987.

Knoll, M., Hernández-Guerra, A., Lenz, B., López-Laatzen, F., Machín, F., Müller, T. J., and Siedler, G.: The Eastern Boundary Current System between the Canary islands and the African coast, Deep Sea Research II, 49, 3427–3440, 2002.

Köhl, A.: Anomalies of meridional overturning: Mechanisms in the North Atlantic, Journal of Physical Oceanography, 35, 1455–1472, 2005.

Larsen, J. C.: Transport and heat flux of the Florida Current at 27° N derived from cross-stream voltages and profiling data: theory and observations, Philos. T. Roy. Soc. London, A 338, 1992.

Lee, T. and Marotzke, J.: Seasonal cycles of meridional overturning and heat transport of the Indian Ocean, Journal of Physical Oceanography, 28, 923–943, 1998.

Longworth, H. R.: Constraining variability of the Atlantic meridional overturning circulation at 26.5° N from historical observations, Ph.D. thesis, School of Ocean and Earth Science, University of Southampton, Southampton, UK, 198 pp, 2007.

Marotzke, J., Cunningham, S. A., and Bryden, H. L.: Monitoring the Atlantic meridional overturning circulation at 26.5° N, Proposal accepted by the Natural Environment Research Council (UK), available online at http://www.noc.soton.ac.uk/rapidmoc/, 2002.

Mittelstaedt, E.: The upwelling area off northwest Africa- a description of phenomena related to coastal upwelling, Progress in Oceanography, 12, 307–331, 1983.

Percival, D. B. and Walden, A. T.: Spectral Analysis for Physical Applications: Multitaper and Conventional Univariate Techniques, Cambridge University Press, Cambridge, UK, 1993.

Piedeleu, M., Sangrà, P., Sanchez-Vidal, A., Fabres, J., Gordo, C., and Calafat, A.: An observational study of oceanic eddy generation mechanisms by tall deep-water islands (Gran Canaria), Geophysical Research Letters, 36, L14 605, 2009.

Rahmstorf, S.: Thermohaline circulation: The current climate, Nature, 421, 699, 2003.

Rayner, D.: RV Ronald H. Brown Cruise RB0602 and RRS Discovery Cruise D304, Rapid Mooring Cruise March and May 2006, Cruise report No. 16, Southampton, UK, 2007.

Risien, C. M. and Chelton, D. B.: A global climatology of surface wind and wind stress fields from eight years of QuikSCAT scatterometer data, Journal of Physical Oceanography, 38, 2379–2413, 2008.

Roemmich, D. and Wunsch, C.: Two transatlantic sections: Meridional circulation and heat flux in the subtropical North Atlantic Ocean, Deep Sea Research, 32, 619–664, 1985.

Sangrà, P. ., Pelegri, J. L., Hernández-Guerra, A., Arregui, I., Martin, J. M., Marrero-Diaz, A., Martinez, A., Ratsimandresy, A. W., and Rodriguez-Santana, A.: Life history of an anticyclonic Eddy, Journal of Geophysical Research, 110, C03 021, 2005.

Sangrà, P., Pascual, A., Rodriguez-Santana, A., Machin, F., Mason, E., McWilliams, J. C., Pelegri, J. L., Dong, C. M., Rubio, A., Aristegui, J., Marrero-Diaz, A., Hernández-Guerra, A., Martinez-Marrero, A., and Auladell, M.: The Canary Eddy Corridor: A major pathway for long-lived eddies in the subtropical North Atlantic, Deep Sea Research I, 56, 2100–2114, 2009.

Vinogradov, S. V., Ponte, R. M., Heimbach, P., and Wunsch, C.: The mean seasonal cycle in sea level estimated from a data-constrained general circulation model, Journal of Geophysical Research, C03032, 2008.

Wooster, W. S., Bakun, A., and McLain, D. R.: The seasonal upwelling cycle along the eastern boundary of the North Atlantic, Journal of Marine Research, 34, 131–141, 1976.

Worthington, L. V.: On the North Atlantic Circulation, Vol.6, (The John Hopkins Oceanography Studies), The John Hopkins University Press, 1976.

Zantopp, R., Lee, T., and Johns, W.: Technical Report 98-006: moored current meter observations east of Abaco, The Bahamas ('ACCP-3' Array), Tech. rep., University of Miami, RSMAS, 1998.

Acknowledgements

I wish to express my deepest gratitude to my advisor Jochem Marotzke. Thanks for the constant support throughout my studies, for the advise whenever I needed it, for encouraging me to publish, and for giving me the opportunity to carry my studies under excellent conditions.

I am very grateful to my co-advisor Torsten Kanzow. Thanks so much for the infinite patience, for motivating me with science, for always having had time for me, and for all your help.

Thanks to Detlef Quadfasel for taking the time for chairing my panels, for the support and rational advise during my studies.

Thanks to Stuart Cunningham for all that I learned from him and for his guidance during the time at sea.

Thanks to Johanna Baehr for all her help during my first months in Hamburg, and for always showing interest in my work. Thanks to Dirk Notz, for helping me during the first steps of my Ph.D.. Thanks to Zoltan Szuts for many helpful discussions, for proof-reading part of this thesis, and for always having had time to help me.

I am very grateful to Carolina Vera and Alberto Piola for introducing me into oceanography and climate sciences and for all their support during my M.Sc. studies at the Universidad de Buenos Aires.

Thanks to the RAPID-MOC monitoring project for providing the mooring data for this thesis.

I am very grateful to the International Max Planck Research School on Earth System Modelling for financing my studies. Many thanks to Antje Weitz for all the support. Thanks to Conni Kampmann for the excellent predisposition to always do something to help, and for listening to me and cheering me up so many times. Thanks to Kornelia Müller for her cheerful good mood and for all the help.

Thanks to all my colleagues of the ocean group, for the nice working atmosphere. Thanks especially to my officemate Daniel for your solidarity and your peaceful good mood, it was great sharing the office with you. I am very grateful to Malte, Aiko, and Kolya for making me feel comfortable, for absorbing work stress, and for listening.

Thanks so much to my friends Elías, Miren, Luis, Xiuhua, Alvaro, Ingrid, Daniela, Gabi, and Marin for all the fun, for making my start in Hamburg so much easier, and for their emotional support. Thanks to Marcos, for all the fun, for being close in the difficult moments, and for your acid sense of humor that would always cheer me up.

Thanks to my friends Luciana, Valeria, Andrea, Belén, Virna, Fernanda, and Uriel for being close despite the large distance and for in one way or another accompanying me during the ups and downs in the last years. Thanks for being there.

I want to express my inmense gratitude to Nidia. For so many things. Thanks for your sincere friendship, for being there and comforting me whenever I needed you, for all the fun. It was great going through this together, I could not imagine this experience without you.

This Ph.D. would have never been possible without the huge love and constant support and encouragement of my family. Thanks to my sister Agustina, for your amazing generosity and understanding, for the long talks on the phone, for always having something to say that would make me feel better, for being always close to me. Thanks to my mum Graciela for giving me strength and for always helping me not to loose focus. Thanks to my dad Hugo for teaching me to never give up and transmitting to me your love of life. Thanks to Pedro for being part of my family and taking care of me.

Die gesamten Veröffentlichungen in der Publikationsreihe des MPI-M
„Berichte zur Erdsystemforschung“,
„Reports on Earth System Science“,
ISSN 1614-1199

sind über die Internetseiten des Max-Planck-Instituts für Meteorologie erhältlich:

http://www.mpimet.mpg.de/wissenschaft/publikationen.html

ISSN 1614-1199